To the Graduate Council,

I am submitting herewith a dissertation written by Philip Gareth Evans entitled “Surface Plasmon Enhanced Heating of Gold Nanoparticles: A Plasmonic Optical Switch”. I have examined the final electronic copy of this dissertation for form and content and recommend that it be accepted in partial fulfillment of the requirements for the degree of Doctor of Philosophy, with a major in Physics.

Thomas. L. Ferrell, Major Professor

We have read this dissertation
and recommend its acceptance:

Marianne Breinig

Thomas Callcott

Ida Lee

John Quinn

Accepted for the Council:

Carolyn Hodges

Dean of the Graduate School

(Original signatures are on file with official student records.)

Surface Plasmon Enhanced Heating of Gold Nanoparticles: A Plasmonic Optical Switch

A Dissertation
Presented for the
Doctor of Philosophy
Degree
The University of Tennessee, Knoxville

Philip G. Evans
May 2007

To Ruth, without whom this
wouldn't have been so much fun.

Acknowledgments

I wish to express my thanks to my supervisor, Dr. Thomas L. Ferrell, for guidance and advice during the course of the last five years. I owe a great deal of gratitude to my mentor and friend, Dr. Ali Passian, for the words and deeds of encouragement in my professional development as a scientist. The members of my Doctoral Committee, Drs. Marianne Breinig, Thomas Callcott, Ida Lee and John Quinn deserve my thanks for their many useful comments and suggestions during the course of this work. I am particularly grateful towards Dr. James Parks and the Department of Physics & Astronomy for financial support through Teaching Assistantships. I would also like to thank my colleagues Rubye Farahi, David Hedden, Ed Arakawa, Christine Cheney, Jody Millward, Alvin Peak and Pam Carter.

Abstract

Recent work by Lereu et al. (Appl. Phys. Lett. Vol. 86, 154101, 2005) demonstrates a method of all-optical transfer of modulation signals using surface plasmon excitation on thin gold films. Localized heating of the film, resulting from surface plasmon decay, alter the optical properties of the device. A similar optical modulation method is now presented using gold nanoparticles. Computational models are used to generate realistic values of the thermo-optical response of gold and the thermal dynamics of a hot nanoparticle-substrate device. Differential pump-probe reflectivity measurements were perferomed and demonstrate modulation frequencies of upto 10kHz, an improvement of two orders of magnitude over the thin-film device. Sample fabrication techniques using physical vapor deposition and interference lithography, and heat transport on the nanoscale are also discussed.

Contents

List of Tables

List of Figures

Chapter 1

Introduction

Recent work by Lereu *et al.* [1] has demonstrated a novel optical switching effect based on the excitation of surface plasmons on a thin gold film by an infrared fiber laser. The decaying surface plasmons heat the film locally and result in the optical properties of the film changing. These changes are detected and measured by a second beam in the visible. This surface plasmon enhanced heating effect demonstrates a method of all-optical switching, where a signal can be transfered from one beam to another. The effect is limited, however, by the time scales required for the film to return to thermal equilibrium before being excited again. Increasing the surface-to-volume ratio will result in quicker cooling, suggesting that a similar effect with higher modulation rates may be possible using small gold particles. The purpose of this dissertation is to determine a method of fabricating, and measuring the properties of, an optical device consisting of gold nanoparticles supported on a suitable substrate. To understand the origins of surface plasmons, a brief introduction is necessary.

1.1 Historical/Background

Plasmons are quanta of the longitudinal waves in electron density as perturbed from neutral equilibrium in an electron gas. A plasmon is a class of elementary excitation, described in detail by Pines & Bohm [2], using the second quantization formalism of quantum mechanics. Many properties of the collective effects of electronic excitations can also be derived classically by Maxwell's equations.

Surface plasmons (SPs) are quanta associated with surface bound waves in the electronic density in a similar fashion to bulk plasmons and are excited by the coupling of the electromagnetic field to available eigenmodes in the electron gas. The breaking of symmetry by the surface results in electronic oscillations with properties different from those of the bulk plasmon. For example, the surface of a semi-infinite plane reduces the surface plasmon resonant frequency ω_{sp} from ω_p to $\omega_p/\sqrt{2}$ for the case of an idealized electron gas bounded by vacuum. In practice, the bulk plasmon resonance lies at a frequency such that the dielectric function vanishes.

Observations pertaining to SPs actually date back to the use of metal oxides in the manufacture of stained glass as early as the 10th Century. Of course, this was not realized by the glaziers. More recently, during the 20th Century, Woods anomaly [3] on ruled metallic gratings and unexplainable peaks in electron scattering experiments with thin metallic films [4], have since been attributed to SP excitation. In Wood's anomaly there is a dark spot

instead of the normal diffraction of a certain wavelength by a metalized grating. This is due to absorption of the photons by surface plasmons. Colloidal solutions of gold, silver and zinc are now routinely touted as health supplements with fantastic benefits such as improvement of arthritis, Alzheimer's disease and the newest weight-loss formulation. The distinctive hues of these alleged health supplements is a result of SP excitation and absorption of light by the small metallic particles.

The first theoretical description of SPs excited by electrons was given by Ritchie [5]. Work by R. A. Ferrell & Quinn [6] further established the momentum-exciton model of collective electron effects by the excitation of the plasma oscillations by fast electrons in thin films. R. A. Ferrell [7] first made the prediction that SPs, under the proper circumstances, would reradiate as ultraviolet light, providing the link between SPs and photons. By the late 1950's and early 1960's SP excitation by electrons on metal films was routinely carried out thanks to a series of electron energy-loss experiments by Powell and Swann [8], Kunz and Raether [9].

The excitation of SPs by light was largely unexplored as it was thought to be impossible due to the momentum mismatch of photons and SPs. This limited the experimental progress on the optical excitation of SPs until ground-breaking work in 1968 by Otto [10], Kretschmann and Raether [11]. They demonstrated that SPs could be excited by light on flat surfaces by using an optical coupling method in which light is incident on the metal film, at an angle greater than the critical angle, through a glass prism instead of directly from vacuum. The prism supplies the extra momentum to the photon, providing the momentum-matching condition to excite SPs. This is commonly referred to as the Kretschmann Configuration and is illustrated in Figure (1.1). SP excitation occurs at the minimum in the reflection coefficient for p-polarized light just as with Brewster's angle, but for the case of a metal foil of complex refractive index. The excitation of SPs is covered in more detail in Chapter 2. In this dissertation, all surface plasmon excitation is assumed to be by light unless otherwise noted.

1.2 Surface Plasmons on Different Geometries

Conditions for SP excitation are highly dependent on the geometry of the surface. With the 2D 'slab' geometry for example, a coupling device is required in order to match the momentum of incident light to the momentum of the SP or no SP can be excited. The Otto and Kretschmann configurations, roughened surfaces and periodic gratings all provide the extra momentum required.

SPs can be excited on particles directly, as long as the particles are small compared to the wavelength, without any coupling technique. This results in quite pronounced optical effects. Introducing various metals such as copper, gold, silver and iron into molten glass is a method of producing stained glass, a technique known and perfected by glaziers over centuries. Mie [12] obtained exact solutions to Maxwell's equations for light scattering from spheres, thus explaining some of the absorption spectra structure to bound surface modes. Earlier, Maxwell-Garnett [13] first attempted to model the optical properties of metallic glasses using a single refractive index, having some success using the effective medium approach. It wasn't until 1958 when Doyle [14] realized that sharp peaks in the absorption spectra of Ag and Au colloid suspensions, unexplained by the traditional Drude-Lorentz model, were due to SP excitations.

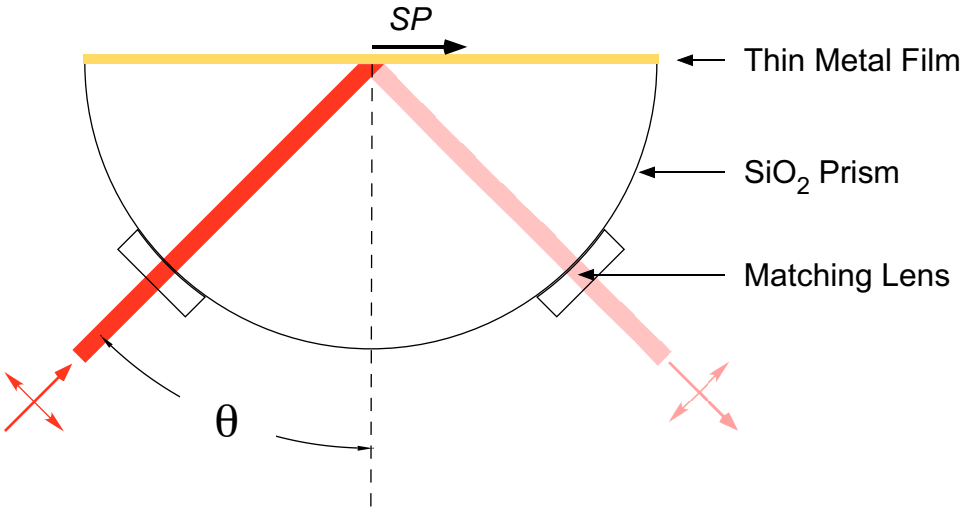

Figure 1.1: The Kretschmann Configuration. A p-polarized laser beam, passing through a cylindrical matching lens and cylindrical SiO_2 prism, is incident on the metal film at an angle θ, exciting a surface plasmon (SP) on the metal surface.

The interaction of light with small particles has been studied extensively. The optical response is dependent on the shape of these particles as well as their proximity to one another and their immediate environment. The particle size is only important as it becomes comparable to the wavelength. Incident light will excite surface modes on the particle, characterized by a sharp peak in the absorption spectra, when the wavelength and polarization of the incident light matches specific conditions corresponding to dipole, quadrupole and higher order resonances along the particle's geometric axes.

SPs can been excited on a variety of different particle geometries such as spheroids [15], ellipsoids [16], toroids [17], squares, dots and triangles. The absorption spectra is highly dependent on the size and shape of such particles [18] [19] [20]. For example, the absorption peak corresponding to a SP excitation on a spherical particle will undergo redshifting as the particle is elongated to a prolate spheroidal shape. Exact theoretical solutions of Maxwell's equations relating to SP excitation on particles have been obtained for simple geometries with spherical symmetry. More complex geometries with lower degrees of symmetry are much more difficult to solve analytically so numerical methods are often used to evaluate such situations. The case of SP excitation on spheroidal nanoparticles is presented in detail in Chapter 2 of this dissertation.

1.3 Consequences of Surface Plasmon Excitation

The excitation of SPs is dependent on surface conditions and the immediate vicinity surrounding the surface. Variables such as the metal film thickness, composition, preparation method, surface roughness and substrate material all affect conditions for SP excitation. Small changes in the absorbance or reflectivity spectrum of a metal film can be quickly and readily detected using modern photodetectors, lock-in amplification, signal processors and computers. This makes SP excitation a powerful experimental technique in surface science, chemistry and biology.

One consequence of SP excitation on flat geometries is the surface enhancement and exponential decay of the electric field away from the surface. Typically, the field will decay to $1/e$ over a distance on the order of a wavelength away from the surface. The field due to SP excitation on a particle is that of a dipole. Objects approaching a SP-supporting surface experience an increasing electric field intensity. This has practical applications in near-field scanning microscopy [21] [22] [23], Surface-Enhanced Raman Spectroscopy (SERS) [24] [25], chemical and biological sensors [26] [27] [28] and non-linear phenomena such as second harmonic generation (SHG) [29].

SPs have a finite propagation length along the surface and are damped as a result of electron, lattice and surface scattering. SPs exhibit two decay modes: non-radiative, where the SP loses energy by collisions, resulting in local heating of the metal; and radiative, where the SP is converted back to a photon. For SP studies and devices using light in the UV-Vis-NIR regions of the EM spectrum, metals such as Au, Ag, Cu, Al are most often used as they exhibit low damping in this wavelength range. Typical SP propagation lengths are on the order of tens of microns.

1.4 Plasmonics

Recent interest in SPs has stemmed from remarkable experimental results with novel optical devices. For example, SPs have been shown to be the mechanism behind efficient light transmission through arrays of sub-wavelength holes, violating Abbe's theorem [30] [31]. In others, light has been converted to SPs and propagated in thin metal strips with physical dimensions of a fraction of the incident wavelength [32] [33]. Periodic arrays of nanostructures on a thin-film have shown promise as SP wave guides [34]. A new field is emerging, known as plasmonics [35], where light is efficiently converted to SPs and vice versa to overcome the diffraction limit, transport properties and conversion efficiencies of traditional semiconductor-based photonic devices.

As the physical dimensions of circuit elements in semiconductor devices shrink in response to technology and market pressures, the connections between circuit elements will also shrink. With modern computer processors often consuming $\sim$ 300W, a great deal of heat is generated within the chip die leading to potentially destructive thermal stress cycling. By replacing circuit elements with appropriate nanoscale elements, it is possible to further reduce the physical size and power consumption of processors and increase the processing power.

Plasmonics also offers improvements in communication systems. In modern fiber optic networks a great deal of energy and computational overhead is spent continually converting electrical signals into light to transport via a fiber, reconversion back to electricity in order to amplify, regenerate and route signals. The spacing of repeaters and regenerators along fiber lines further increases infrastructure costs to the network provider. With advances in plasmonics, it may be possible to reduce cost and achieve far superior network operation by replacing traditional fibers with plasmonic waveguides and traditional switching circuitry with plasmonic switches and nanoparticle circuit elements.

Engheta [36] has shown that linear chains of nanoparticles can theoretically be used as nano-transmission lines exhibiting all properties of traditional transmission lines. The electrodynamic response of the chains show capacitive, inductive and loss tangent effects and can be thought of as nanocircuit elements. The addition of a plasmonic switch would complement the linear chains and provide all nanocircuit elements to build functioning fully plasmonic circuits.

1.5 Scope of this Work

Recent work by Lereu *et al.* [1] has shown a novel effect based on the decay of surface plasmons on a thin Au film. In their work, a pump beam operating in the IR excites surface plasmons on a thin Au film in the Kretschmann configuration. A probe beam, operating in the visible, is focused on a region of the film where the IR SPs are excited. As the IR SPs decay, the Au is locally heated, leading to a change in the optical properties of the region. The probe beam detects these changes.

This technique demonstrates a method of all-optical switching, whereby a signal from a high-power, low energy beam is transferred, via SP excitation and subsequent thermal decay, to a second higher energy beam. The effect is limited, however, by the time scales required for the film to return to thermal equilibrium before being excited again.

It is thought that a similar thermal effect caused by decaying SPs can also be explored by devices using Au nanoparticles. With a much greater surface-to-volume ratio than thin-films, nanoparticles would heat up and cool down much quicker than a comparatively larger and thicker film. Therefore, any changes in the particle cross-sections due to thermal effects would be enhanced. By altering the size and shape of nanoparticles, it is possible to tune the absorption spectra to any particular wavelength, providing for a method wavelength multiplexing.

The study of thermal effects in thin films due to laser heating is well established [37]. Various pump-probe experiments have been performed using pulsed lasers operating in the femtosecond temporal regime [38] [39]. These techniques are valuable for the study of electron-phonon interactions in metals. Energy is transfered from the pump pulse to the electrons in the sample, leading to extremely rapid increase in the electron temperature, resulting in a temperature difference between the electrons and the atomic lattice. At this elevated temperature, the mean free path of electrons is very short resulting in many collisions. Each collision transfers energy from the electron to the lattice and eventually, over a time scale of picoseconds ($\times 10^{-12}$ seconds), the electron and lattice temperatures reach equilibrium.

A lot of attention is coming to focus on the thermal response of nanoparticles and nanocomposites under pulsed laser excitation [40] [41]. So far, recent experimental efforts have focused on the fundamental solid-state aspects of the thermal response of nanoparticles. This dissertation further adds to this work and presents new results showing the thermo-optical response of Au nanoparticles in the continuous-wave (CW) pump regime, demonstrating nanoparticles acting as plasmonic switches. These results are directly applicable to plasmonics, opening the door to a quantum amplifier.

This dissertation is outlined thus: Chapter 2 presents an introduction of surface plasmon theory on thin-films and nanoparticles. Attention is focused in particular to the case of spheroidal particles much smaller than the wavelength of light. Surface plasmon excitation, as the reader will learn, is extremely sensitive to the dielectric function ϵ of the supporting material, in this case Au, and immediate surroundings. Chapter 2 also includes an introduction to the Drude-Lorentz theory of the dielectric function.

Chapter 3 presents new work on the thermo-optical response of spheroidal nanoparticles. A numerical model is created in order to generate realistic values of the dielectric function of Au at arbitrary temperatures in the range 295K to 1295K. Chapter 4 considers the thermal dynamics of the nanoparticle-substrate-air environment and heat transport from the nanoparticle to it's surroundings. A brief introduction to heat transfer is given, followed with numerical modeling of the problem via finite-element anaylsis (FEA) to provide insights into time- and spatial dependence of temperature in the modeled system.

Chapter 5 presents the work on the sample fabrication methods used in this dissertation, including sample microscopy and analysis, comparisons with various models describing the optical response, experimental set-up, procedures and methodology. Chapter 6 introduces the pump-probe experimental method and presents the results of pump-probe experimental work on Au nanoparticle samples, together with analysis and comparison with theoretical and numerical results. Finally, Chapter 7 concludes and summarizes the results of this dissertation.

Chapter 2

Theory

2.1 Surface Plasmons on Infinite Geometries

Consider a semi-infinite geometry in 2D Cartesian space. The half-space $z < 0$ (region 1) is occupied by a metal having a complex frequency-dependent dielectric function $\epsilon_m(\omega) = \epsilon'_m(\omega) + i\epsilon''_m(\omega)$. The half-space $z > 0$ (region 2) is a dielectric ambient medium having a dielectric function $\epsilon_d(\omega)$. A p-polarized electromagnetic wave propagates in the x-direction. The electric fields in regions 1 and 2 are expressed as

$$\mathbf{D}_1 = \epsilon_m E_1(\hat{\mathbf{x}} + \hat{\mathbf{z}}) \exp i(k_{x1}x - k_{z1}z - \omega t) \tag{2.1.1}$$

$$\mathbf{D}_2 = \epsilon_d E_2(\hat{\mathbf{x}} + \hat{\mathbf{z}}) \exp i(k_{x2}x + k_{z2}z - \omega t.) \tag{2.1.2}$$

The normal components of $\mathbf{D}$ are continuous at the boundary $z = 0$. There are no external charges; the electric fields occur only from the polarization charges on the boundary. Applying the continuity of the tangential components of $\mathbf{E}$, i.e.,

$$E_{z=0+} = E_{z=0-} \tag{2.1.3}$$

provides the necessary condition for surface plasmon excitation

$$\epsilon_m = -\epsilon_d. \tag{2.1.4}$$

An ideal metal, neglecting damping, can be assumed for the metal in this simplistic case so ϵ_m can be expressed as

$$\epsilon_m = 1 - \left(\frac{\omega_p}{\omega}\right)^2 \tag{2.1.5}$$

In reality, however, no metal satisfies equation (2.1.5) as it is necessary to include the effects of damping and bound electrons as well as other deviations of the optical properties of real metals from those of the idealized electron gas model. But in the idealized case, equations (2.1.4) and (2.1.5) yield an expression that specifies the surface plasmon frequency on the planar surface of a semi-infinite medium. This is given by the equation

$$\omega_{sp} = \frac{\omega_p}{\sqrt{\epsilon_d + 1}} \tag{2.1.6}$$

where

$$\omega_p = \sqrt{\frac{4\pi n e^2}{m_e^*}} \tag{2.1.7}$$

is the plasma frequency. n is the number of electrons per unit volume and m_e^* the effective electron mass. When the metal is bounded by vacuum, the right-hand side of equation (2.1.6) becomes $\omega_p/\sqrt{2}$.

2.1.1 Optical Excitation of Surface Plasmons

Surface plasmons can only be excited when the momentum and energy of incoming particle matches. This is accomplished easily experimentally with electrons but is more difficult with photons. The dispersion relation for a photon in a vacuum is given by

$$\omega = ck \tag{2.1.8}$$

and is often referred to as the 'light-line'. Figure (2.1) shows the dispersion relations for the vacuum bounded surface plasmon (equation 2.1.6) and the light-line. Since the two curves never cross at non-zero values of k, photons directly incident on a metal surface cannot excite surface plasmons. However, photons can excite surface plasmons when used with a suitable coupling device.

In the Kretschmann configuration, Figure (1.1), light is incident through an optically dense material, such as a hemispherical prism, at an angle θ. The metal on which the surface plasmons will be excited is mounted on the flat face of the prism. The photon wavevector parallel to the prism-metal interface in this case is given by

$$k_x = \frac{\omega}{c}\sqrt{\epsilon_0}\sin\theta \tag{2.1.9}$$

so the prism effectively supplies the required momentum to the photon in order to match the surface plasmon excitation conditions. Other methods of optical coupling to surface plasmons utilize gratings and surface roughness features to supply the needed momentum. The interested reader is referred to Ref. [42] for more details.

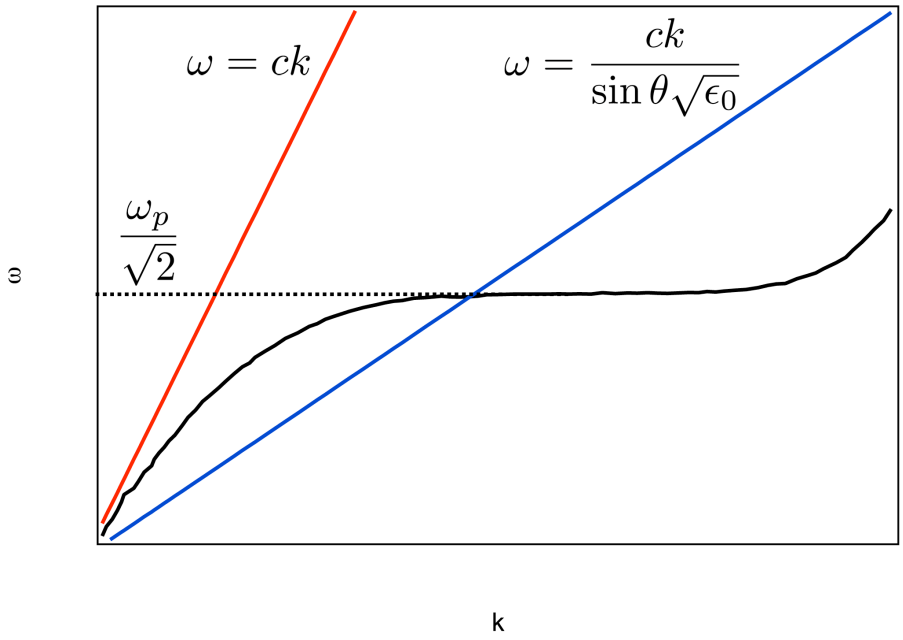

Figure 2.1: Dispersion relations for a SP in a slab geometry bounded by vacuum, light in vacuum, in the Kretschmann configuration at angle θ.

2.1.2 Surface Plasmons on Thin Films

Surface plasmons on vacuum deposited thin films on prisms can also be excited with the Kretschmann configuration. The efficiency of light-SP coupling can be determined by measuring the internally reflected light intensity as a function of incident angle. At some angle θ_{sp} for a particular value of λ, there will be a sharp dip in the reflectance spectra, indicating SP resonance.

Maximum energy is transfered from the light to the surface plasmon when three conditions are met: the polarization of the incoming light must be p-polarized; the angle of incidence $\theta = \theta_{sp}$; and the thickness d of the metal film is optimized with respect for a particular incident λ.

The first two conditions can be satisfied with sound experimental method. The condition on optimum film thickness must be evaluated using Fresnel's coefficients for the reflected beam in a 3-layer structure. Maximum energy is transfered from the light to the SP when the reflected light intensity from the metal film is zero. The reflectivity from a 3-layer structure is

$$R^p = \left| r_{012}^{(p)} \right|^2 = \left| \frac{r_{01}^{(p)} + r_{12}^{(p)} exp(2ik_{z1}d)}{1 + r_{01}^{(p)} r_{12}^{(p)} exp(2ik_{z1}d)} \right|^2 \tag{2.1.10}$$

where

$$r_{ik}^{(p)} = \frac{(\frac{k_{zi}}{\epsilon_i} - \frac{k_{zk}}{\epsilon_k})}{(\frac{k_{zi}}{\epsilon_i} + \frac{k_{zk}}{\epsilon_k})} \tag{2.1.11}$$

with the (p) superscripts denoting the p-polarized wave.

Figure (2.2) shows the consequences of different Au film thickness on the reflectivity spectra for SP excitation in the Kretschmann configuration. Increasing the Au thickness from $d = 35$nm to 50nm results in the reflectivity spectra being redshifted, narrowed and minima approaching zero.

Figure (2.3) shows the reflectivity from a $d = 50$nm Au film as a function of incident angle θ for four common laser wavelengths λ. In the blue part of the spectrum, the angle-resolved reflectivity shows little detail, with an extremely broad dip occurring around $\sim 60°$. As the incident light is shifted from the green and into the near-infrared (NIR) regions, the reflectivity valley narrows, becoming much more pronounced at lower values of θ. Near-total extinction of the reflected beam occurs for $\lambda = 632.8$nm at 43.3° but with a wide resonance. A much sharper feature occurs for $\lambda = 830.8$nm at 41.1°, however, the minima in reflectivity reaching 0.1. This may further be enhanced by optimizing the film thickness specifically for this wavelength.

Figure (2.4) shows the angular reflectivity spectrum for four thicknesses of Au film in the Kretschmann configuration with an SiO_2 substrate. The excitation wavelength in this case is fixed at $\lambda = 632.8$nm. As the Au film thickness increases, the dip in the reflectivity spectrum corresponding to SP excitation shifts from a broader, less pronounced dip (R=0.21 at θ=43.8° for d=35nm) to a much narrower dip with minima almost reaching zero ($R \approx 1 \times 10^{-3}$ at θ=43.3° for d=50nm).

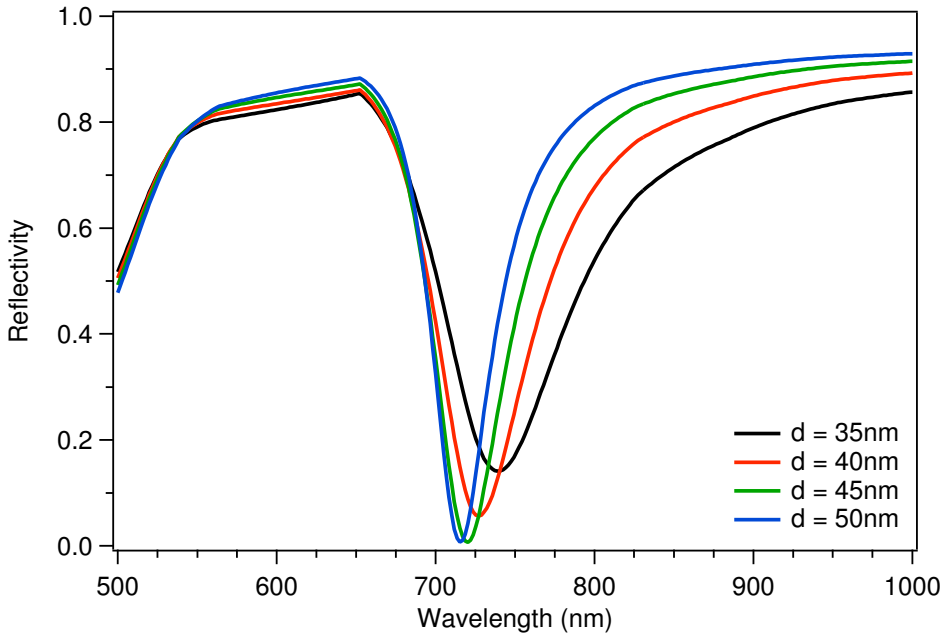

Figure 2.2: R vs. λ for four thicknesses d of Au on SiO_2 in the Kretschmann configuration in a vacuum environment. The angle of incidence is fixed at θ=45°.

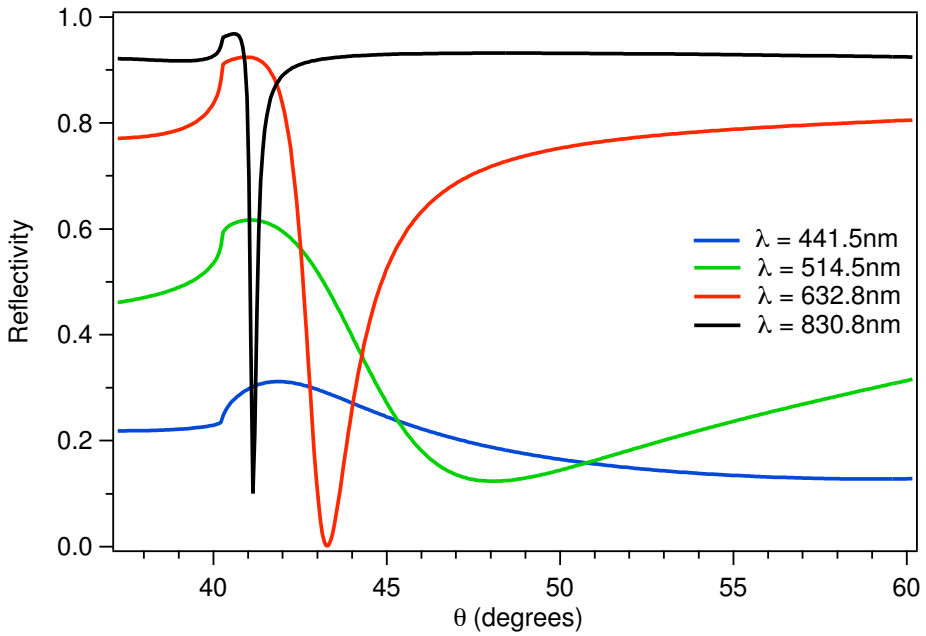

Figure 2.3: R vs. θ for four common laser wavelengths. $d = 50$nm Au on an SiO_2 substrate in the Kretschmann configuration in a vacuum environment.

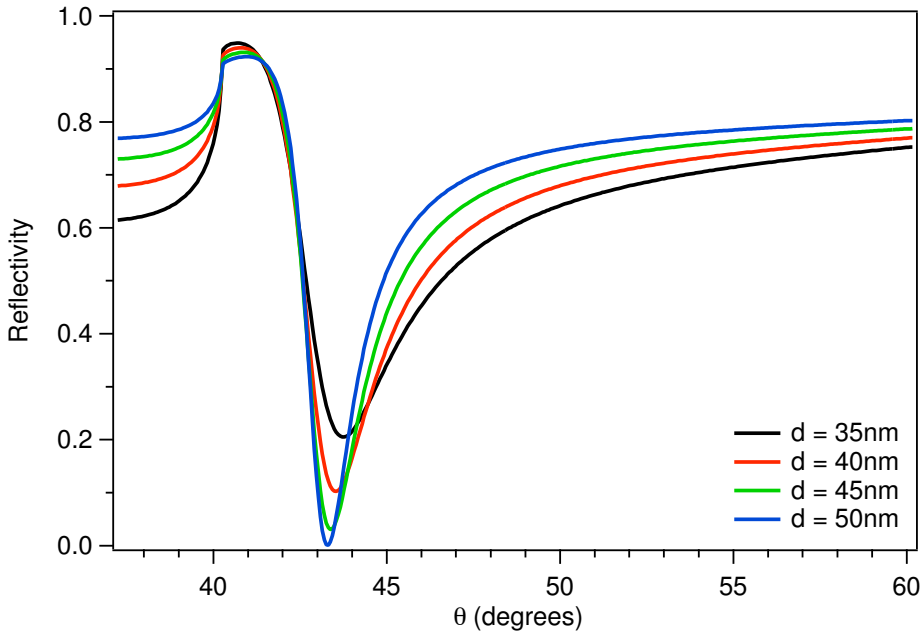

Figure 2.4: R vs. θ for four thicknesses of Au d on an SiO_2 substrate in the Kretschmann configuration in a vacuum environment. $\lambda = 632.8$nm.

2.2 Surface Plasmon Excitation on Nanoparticles

Surface plasmon excitation on nanoparticles (particles of dimension $\sim 10^{-9}$m) is rather different from the case of thin films. Two notable differences arise: the dispersion relation exhibits strong dependance on the nanoparticle size and shape, and SPs on nanoparticles may be excited directly without using a coupling method. This difference arises fundamentally from the fact that the infinite boundaries assumed in the thin-film case are removed as the particles are individually isolated and finite in size. SP excitation on nanoparticles has immense technological advantages with applications in chemical and biological detection, scanning probe microscopy and Raman spectroscopy. In this section, the conditions for SP excitation on nanoparticles is introduced.

A suitable basis geometry is required in order to develop a theoretical framework for SP excitation on nanoparticles. Little [43] and Kennerly [44] used oblate spheroidal coordinates to describe nanoparticles fabricated by annealing metal-island films. Bloemer [15] & Buncick [16] used prolate spheroidal and ellipsoidal coordinates respectively to describe nanoparticles grown via a glancing-angle deposition (GLAD) method. Both spheroidal coordinate systems have the advantage of being completely separable in the Laplace equations, providing analytic solutions for the electric potential Φ. For more detailed information on electrodynamics in the spheroidal coordinate system, the reader is referred to Refs. [19] and [20].

Spheroidal coordinates are denoted (η, θ, ϕ). η is the radial-like coordinate, a constant value of which specifies the surface of a spheroid. The polar coordinate θ specifies a hyperboloid where $\theta = \cos\psi$, ψ being the angle between the z-axis and the asymptote of the hyperbola. The azimuthal coordinate ϕ is the same as in spherical coordinates. Figure (2.5) illustrates the two families of spheroids.

The theoretical framework is outlined thus: the Laplace equations for the electric potential Φ are solved in the spheroidal coordinate space. A fixed coordinate, representing the spheroid's surface, provides the boundary between particle interior and the vacuum ambient. By introducing a spatially uniform time varying electric field, therefore restricting the framework to the dipole excitations (l =1, $m \pm l$), the surface and volume charge densities can be obtained for the particle. The particle polarizability and effective dipole moment are then obtained. The scattering and absorption cross-sections are subsequently found using the optical theorem.

2.2.1 Oblate Spheroids

The minor axis is parallel with the Cartesian z-axis and the spheroid is formed with a rotation of the hyperbola around the minor axis. Each coordinate has the following ranges:

$$\begin{aligned} 0 \leq &\eta \leq \infty \\ 0 \leq &\theta \leq \pi \\ 0 \leq &\phi \leq 2\pi \end{aligned}$$

Transformation equations between oblate spheroidal and Cartesian coordinates are

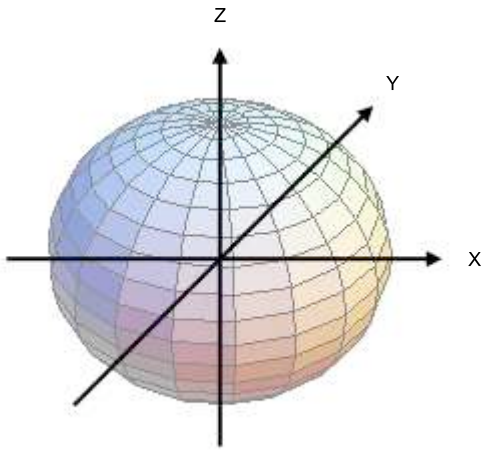

(a) An oblate spheroid

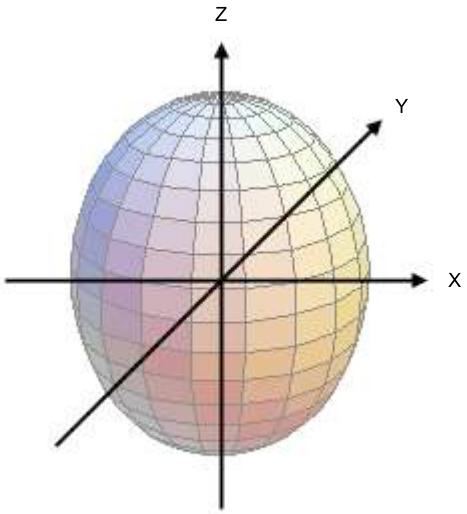

(b) A prolate spheroid

Figure 2.5: Spheroids

$$
\begin{aligned}
x =& a\sqrt{(1+\eta^2)}\sin\theta\cos\phi \\
y =& a\sqrt{(1+\eta^2)}\sin\theta\cos\phi \\
z =& a\eta\cos\theta
\end{aligned}
$$

where a is the focal length of the spheroid. The minor-to-major axis ratio R of an oblate spheroidal particle with shape parameter η is

$$R = \frac{\eta}{\sqrt{(1+\eta^2)}}. \tag{2.2.1}$$

As $\eta \to \infty, R \to 1$, the oblate spheroid becomes a sphere and as $\eta \to 0, R \to \infty$, the oblate spheroid becomes a flat disk of infinite radius.

2.2.2 Prolate Spheroidal Coordinates

The major axis is parallel with the Cartesian z-axis and the spheroid is formed with a rotation of the hyperbola around the minor axis. Each coordinate has the following ranges:

$$
\begin{aligned}
1 \leq& \eta \leq \infty \\
0 \leq& \theta \leq \pi \\
0 \leq& \phi \leq 2\pi
\end{aligned}
$$

Transformation equations between prolate spheroidal and Cartesian coordinates are

$$
\begin{aligned}
x =& a\sqrt{(\eta^2-1)}\sin\theta\cos\phi \\
y =& a\sqrt{(\eta^2-1)}\sin\theta\cos\phi \\
z =& a\eta\cos\theta
\end{aligned}
$$

where again, a is the focal length of the spheroid. The major-to-minor axis ratio R of a prolate spheroidal particle with shape parameter η is

$$R = \frac{\sqrt{(\eta^2-1)}}{\eta} \tag{2.2.2}$$

As $\eta \to \infty, R \to 1$, the prolate spheroid becomes a sphere and as $\eta \to 1, R \to \infty$, the prolate spheroid becomes a line of infinite length.

2.2.3 Solutions to Laplace's Equation

The solutions to the Laplace equation, $\nabla^2\Phi = 0$ in the spheroidal coordinate system, is sought. The method of separation of variables can be applied with the potentials cast as

$$\Phi(\eta,\theta,\phi) = G(\eta)F(\theta)H(\phi) \tag{2.2.3}$$

The solutions of the Laplace equation in oblate spheroidal coordinates for inside and outside the particle are

$$\Phi_{in} = \sum_{lmp} A_{lmp} Q_{lm}(i\eta) P_{lm}(i\eta) Y_{lm}^{p}(\theta, \phi) \tag{2.2.4}$$

$$\Phi_{out} = \sum_{lmp} B_{lmp} Q_{lm}(i\eta) P_{lm}(i\eta) Y_{lm}^{p}(\theta, \phi) \tag{2.2.5}$$

A_{lm} and B_{lm} are weighting coefficients, $P_{lm}(i\eta)$ and $Q_{lm}(i\eta)$ are the associated Legendre functions of the first and second kinds respectively. Y_{lm}^{p} are the spherical harmonics. To find similar expressions in the prolate case, one replaces $i\eta$ with η.

The electrodynamic response of a spheroidal nanoparticle can be approximated with the non-retarded (NR) dipole approximation. Retardation effects are negligible since the physical size of the nanoparticles are much smaller than λ. This leads to a vast simplification of the theoretical framework, but limits resonance to the l=1, $m\pm$ 1 dipole modes. The l=0 mode is also neglected as there is no net charge on the particle. The electric fields inside and outside the particle are found by $\mathbf{E} = -\nabla\Phi$, to which a time-dependent and spatially uniform field term is added, corresponding to the incident field.

2.2.4 Polarizabilities & Resonance Conditions

The incident electric field induces a surface charge density on the spheroid given by

$$\sigma = \frac{1}{4\pi} \sum_{mp} \hat{\eta} \cdot (\nabla\Phi_{in} - \nabla\Phi_{out})\Big|_{\eta=\eta_0} \tag{2.2.6}$$

where $\hat{\eta}$ is the unit vector pointing outwards and η_0 represents the particle surface. The surface and volume charge densities are related by

$$\rho = \frac{\sigma\delta(\eta - \eta_0)}{h_\eta} \tag{2.2.7}$$

δ being the Dirac delta function and h_η the scale factor for the η coordinate. From the volume charge density ρ, the electric dipole moment $\mathbf{p}$ can be found by

$$\mathbf{p} = \int_V \mathbf{x}'\rho(\mathbf{x}')d^3dV \tag{2.2.8}$$

The dipole moments are related to the polarizability α_i in the linear regime by

$$\mathbf{p}_i = \alpha_i \mathbf{E}_i \tag{2.2.9}$$

The polarizabilities for a oblate spheroid in Cartesian components $\mathbf{p}_i$ are

$$\alpha_x^o = \frac{2a^3[\epsilon-1]\sqrt{(1+\eta^2)}}{3Q_{11}(i\eta)[\epsilon-\epsilon_{11}(i\eta)]}$$
$$\alpha_y^o = \frac{2a^3[\epsilon-1]\sqrt{(1+\eta^2}}{3Q_{11}(i\eta)[\epsilon-\epsilon_{11}(i\eta)]} \tag{2.2.10}$$
$$\alpha_z^o = \frac{-a^3\eta[\epsilon-1]}{3Q_{10}(i\eta)[\epsilon-\epsilon_{10}(i\eta)]}$$

(2.2.11)

A resonance condition exists as $\epsilon_{lm} \to \epsilon$, where ϵ is the dielectric function of Au, a function of wavelength. This corresponds to a surface plasmon excitation such that

$$\epsilon \to \epsilon_{1m} = \left.\frac{P_{1m}(i\eta)dQ_{1m}(i\eta)}{Q_{1m}(i\eta)dP_{1m}(i\eta)}\right|_{\eta=\eta_0} \tag{2.2.12}$$

P_{lm} and Q_{lm} are the associated Legendre functions of argument $i\eta$ and are

$$P_{10}(i\eta) = i\eta \tag{2.2.13}$$
$$P_{11}(i\eta) = \sqrt{-\eta^2-1} \tag{2.2.14}$$
$$Q_{10}(i\eta) = \frac{i\eta}{2}\ln\left(\frac{i\eta+1}{i\eta-1}\right) - 1 \tag{2.2.15}$$
$$Q_{11}(i\eta) = \sqrt{-\eta^2-1}\left[\frac{\ln}{2}\left(\frac{i\eta+1}{i\eta-1}\right) + \frac{i\eta}{1+\eta^2}\right] \tag{2.2.16}$$

dP_{lm} and dQ_{lm} indicate the derivative of P_{lm} and Q_{lm} with respect to η. Again, similar expressions in the prolate case are found by replacing $i\eta$ with η.

The dielectric function resonance condition for SP excitation on spheroidal nanoparticles is only dependent on the shape parameter η. It is possible to select the SP excitation wavelength by changing the particle geometry. Figures (2.6) and (2.7) show graphs of the resonance condition with respect to the shape parameter η for prolate and oblate spheroids respectively.

2.2.5 Dipole Scattering and Absorption Cross Section

The total cross-section is the sum of scattered and absorbed cross sections and is derived using the optical theorem [45].

$$\sigma_t\Big|_s = \frac{4\pi\omega}{c}\Im[\alpha_x] \tag{2.2.17}$$
$$\sigma_t\Big|_p = \frac{4\pi\omega}{c}\Im[\alpha_y\cos^2\theta + \alpha_z\sin^2\theta] \tag{2.2.18}$$

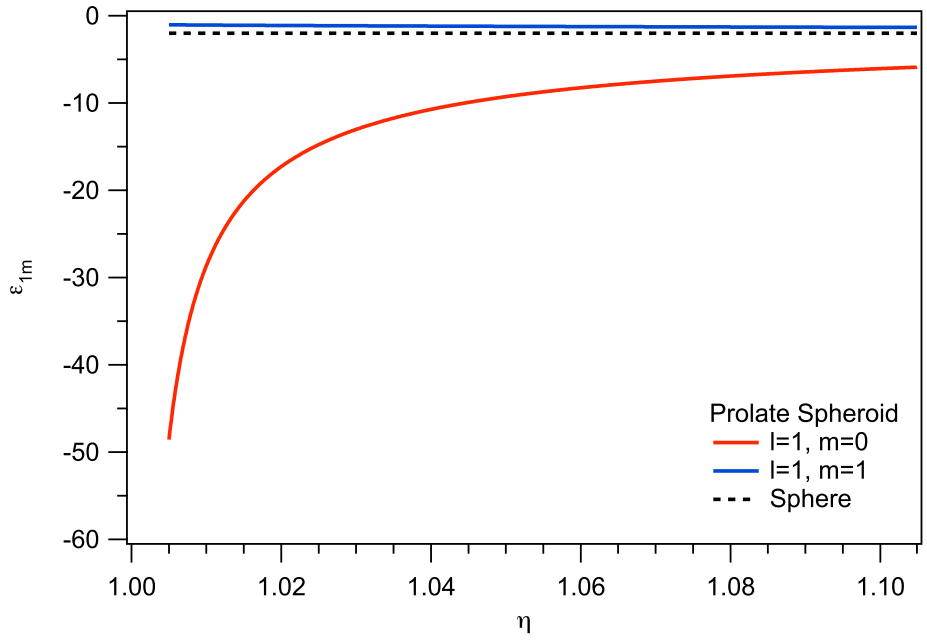

Figure 2.6: The resonance condition for prolate spheroids as a function of the shape parameter η. l=1, m=0 is the long-wavelength mode about the major axis, l=1, m=1 is the short-wavelength mode about the minor axis.

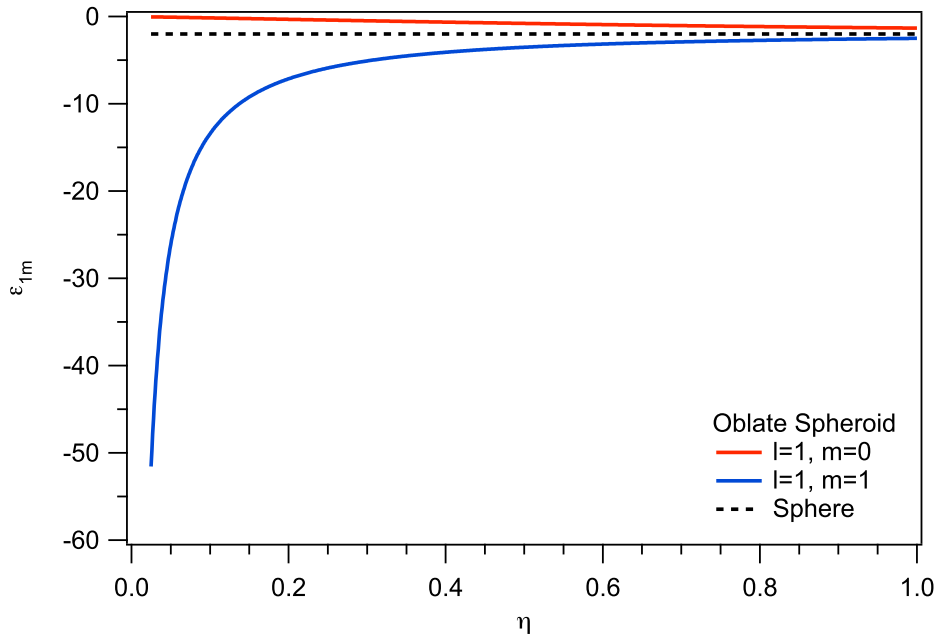

Figure 2.7: The resonance condition for oblate spheroids as a function of the shape parameter η. l=1, m=0 is the short-wavelength mode about the minor axis, l=1, m=1 is the long-wavelength mode about the major axis.

$$\sigma_{scat}\Big|_s = \frac{8\pi\omega^4}{3c^4}|\alpha_x|^2 \tag{2.2.19}$$

$$\sigma_{scat}\Big|_p = \frac{8\pi\omega^4}{3c^4}(|\alpha_y|^2\cos^2\theta + |\alpha_z|^2\sin^2\theta) \tag{2.2.20}$$

where θ is the angle between the incident beam and the major axis of the particle. and the subscripts s and p denote the polarization of incident light. $\sigma_{scat} \ll \sigma_{abs}$ so $\sigma_t \simeq \sigma_{abs}$. Given that the intensity of the incident beam is I_0, then

$$I_0 = I_t + I_{sc} + I_{abs}$$

where I_t, I_{sc} and I_{abs} are the transmitted, scattered and absorbed intensities, respectively. The transmittance T is given as

$$T = \frac{I_t}{I_0} = 1 - \left[\frac{I_s}{I_0} + \frac{I_a}{I_0}\right] = 1 - N\sigma_t \tag{2.2.21}$$

where N is the number of particles per unit area. Equation (2.2.21) assumes that $I_{sc} \ll I_{abs}$. The absorbance A is therefore

$$A = -\log(T) = -\log\left(\frac{1}{1 - N\sigma_t}\right) \tag{2.2.22}$$

2.3 The Dielectric Function ϵ

Resonance conditions for SPs depend on structure and geometry of surface and also on the optical properties of the material. When $\epsilon_{lm} = \epsilon$, as illustrated in Section 2.2 previously, sharp peaks in absorption spectrum are visible due to the resonance in the polarizabilities, expressions of which are given in equation (2.2.11).

Knowledge of the dielectric function is important in this dissertation. There are numerous approaches to determine the dielectric function theoretically. Such approaches include the Drude-Lorentz model, the random-phase approximation (RPA), Hartree-Fock (HF), density functional theory (DFT). For most systems consisting of a large number of atoms in a linear regime, the Drude-Lorentz model gives an adequate description of real metals in the UV-Vis-NIR region. A brief introduction to the Drude-Lorentz dielectric function is given below with particular focus on noble metals.

2.3.1 The Drude-Lorentz Model

The Drude-Lorentz model is derived from classical arguments and provides most quantitative aspects of the electrodynamic response of charge carriers to an applied electric field. An infinitely large mass (the atomic nucleus) is bound to a small mass (the electron) by a spring. The equation of motion for the electron is given by

$$\frac{d^2\mathbf{r}}{dt^2} + \gamma\frac{d\mathbf{r}}{dt} + \omega_0^2\mathbf{r} = \frac{-e\mathbf{E}_{loc}}{m_e} \tag{2.3.1}$$

where m_e is the electron mass, e is the electronic charge and γ is a damping term. $\mathbf{E}_{loc}$ is the local electric field driving the electron and for simplicity assume $< \mathbf{E}_{loc} >= \mathbf{E}$, $\mathbf{E}$ being the macroscopic electric field. In what follows, $\mathbf{E}$ is understood to vary in time as $e^{i\omega t}$. The solution to equation (2.3.1) is

$$\mathbf{r} = \frac{-e\mathbf{E}}{m} \frac{1}{(\omega_0^2 - \omega^2) - i\gamma\omega} \tag{2.3.2}$$

and the induced dipole moment ($\mathbf{p} = -e\mathbf{r}$) is

$$\mathbf{p} = \frac{e^2\mathbf{E}}{m} \frac{1}{(\omega_0^2 - \omega^2) - i\gamma\omega} \tag{2.3.3}$$

The displacement $\mathbf{r}$ is sufficiently small to be able to assume a linear relationship between $\mathbf{p}$ and $\mathbf{E}$, namely

$$\mathbf{p} = \alpha(\omega)\mathbf{E} \tag{2.3.4}$$

which leads to

$$\alpha(\omega) = \frac{e^2}{m} \frac{1}{(\omega_0^2 - \omega^2) - i\gamma\omega} \tag{2.3.5}$$

where $\alpha(\omega)$ is the frequency dependent atomic polarizability. The macroscopic polarization is defined as

$$\mathbf{P} = N\alpha(\omega)\mathbf{E} \tag{2.3.6}$$

and by applying Maxwell's equations

$$\mathbf{D} = \epsilon(\omega)\mathbf{E} = \mathbf{E} + 4\pi\mathbf{P} \tag{2.3.7}$$

the frequency-dependent dielectric function $\epsilon(\omega)$ is

$$\epsilon(\omega) = 1 + \frac{\omega_p^2}{(\omega_0^2 - \omega^2) - i\gamma\omega} \tag{2.3.8}$$

Again, the quantity $\omega_p = \sqrt{\frac{4\pi n e^2}{m_e}}$ is the plasma frequency.

2.3.2 Free and Bound Electron Contributions

For atoms with more than one electron per atom, a summation over all electrons j must be taken. The dielectric function has contributions from both free and bound electrons. In a classical sense, the bound electrons are oscillators with a resonant frequency of ω_j. When considering a system with a number of oscillators, the the dielectric function is a sum of all oscillators, i.e.,

$$\epsilon(\omega) = 1 + \sum_{j=0}^{N} \frac{f_j\omega_p^2}{(\omega_j^2 - \omega^2) - i\gamma_j\omega} \tag{2.3.9}$$

where f_j is the oscillator strength and γ_j is the damping term for the jth oscillator. Quantum mechanically, the resonant frequencies ω_j correspond to transitions between atomic energy levels and γ_j to the inverse-lifetimes of excited states. Accurate values of the dielectric function of real materials therefore require specific knowledge of the band structure to enable the atomic transitions to be found.

Free electrons are described by the Drude model where the positive-ion background (analogous to the spring restoring force term $m\omega_0^2\mathbf{r}$) is removed, i.e., $\omega_j = 0$. Equation (2.3.9), rewritten in the free electron regime becomes

$$\epsilon_f(\omega) = 1 - \frac{\omega_p^2}{\omega(\omega + i\gamma_f)} \tag{2.3.10}$$

where γ_f is the damping frequency for free electrons.

The dielectric function can be expressed as a simple sum of bound- and free-electron contributions such that

$$\epsilon(\omega) = \epsilon_b(\omega) + \epsilon_f(\omega) \tag{2.3.11}$$

with the bound contribution given by

$$\epsilon_b(\omega) = \sum_{j=0}^{N} \frac{f_j\omega_p^2}{(\omega_j^2 - \omega^2) - i\gamma_j\omega} + \frac{\omega_p^2}{\omega(\omega + i\gamma_f)} \tag{2.3.12}$$

2.3.3 Refractive Index

$\epsilon(\omega)$ is inherently complex and this is expressed as

$$\epsilon(\omega) = \epsilon'(\omega) + i\epsilon''(\omega) \tag{2.3.13}$$

where ϵ' is the real part and ϵ'' is the imaginary part, responsible for absorption. ϵ is also frequently given in terms of the refractive index n and the extinction coefficient k as $\epsilon = (n + ik)$ which gives the real and imaginary parts as

$$\epsilon' = n^2 - k^2 \tag{2.3.14}$$

$$\epsilon'' = 2nk \tag{2.3.15}$$

Metals and other materials having a metallic phase have a negative value of ϵ'.

As the dielectric function is inherently due to the electrons in the material, the dielectric function is dependent on many variables, for example, band structure, temperature, frequency of incident radiation, etc. As a general quantitative approach for describing the dielectric functions of metals, the Drude approximation adequately describes most features of the metal's response to an external field.

It should be noted that two different expressions for the dielectric function may be used. $\epsilon(\omega)$, i.e. a function of frequency can be expressed as $\epsilon(\lambda)$, i.e., a function of wavelength, by transforming the argument using $\omega = \frac{2\pi c}{\lambda}$, where c is the speed of light in vacuum.

Chapter 3

Temperature Dependent Optical Response of Nanoparticles

In this chapter the effects of temperature on the optical response of oblate spheroidal gold nanoparticles are studied. These effects can be broken down into two main parts; the volumetric expansion of the nanoparticle, and the temperature dependence of the dielectric function. Combined, these effects alter the optical properties of the nanoparticle as a function of temperature. A numerical model that supplies realistic values of the dielectric function $\epsilon(T)$ over a temperature range from 295K to 1295K is presented.

3.1 Volumetric Expansion

Chapter 2 introduced the theoretical framework describing the optical response of spheroids. This will now be applied to investigate how temperature, through expansion, alters the spheroid's optical response. Consider a single oblate spheroidal nanoparticle at an initial temperature T_0. The spheroid expands upon heating and both the initial minor (z_0) and major (r_0) axes are expected to undergo expansion, but each to what degree is not known. Results from Perner *et al.* [46] suggest that an ultra-fast pulse heated spheroidal nanoparticles suspended within a glass matrix will expand primarily along the major axis. In this section, the isotropic and anisotropic expansions of oblate spheroids are considered.

3.1.1 Isotropic Expansion

Upon heating, the dimensions of the major and minor axis expand by an amount proportional to the temperature change ΔT. In the linear regime, the expanded length is expressed as

$$l = l_0(1 + \alpha_T \Delta T) \tag{3.1.1}$$

where l_0 is the initial length and α_T is the linear thermal expansion coefficient. If both the major and minor axes expand isotropically, the expression for the axis ratio R is

$$R = \frac{z}{r} = \frac{z_0(1+\alpha_T \Delta T)}{r_0(1+\alpha_T \Delta T)} \tag{3.1.2}$$

$$= \frac{z_0}{r_0} \tag{3.1.3}$$

i.e., R remains constant and as a result, the shape parameter η_0 remains constant also. The isotropic expansion results in a larger focal length a given by

$$a(\Delta T) = \frac{r_0(1+\alpha_T \Delta T)}{\sqrt{\eta_0^2 + 1}}. \tag{3.1.4}$$

3.1.2 Anisotropic Expansion

In this section, the anisotropic expansion of an oblate spheroid is considered. Expansion is only along the major axis, with the minor axis staying constant. Such a situation may be realized by confining the nanoparticle to a surface or inside a dielectric matrix. This is the most extreme case and is highlighted in order to investigate the most pronounced changes in the optical properties with increasing temperature. The volume of an oblate spheroid at an arbitrary initial temperature T_0 is expressed as

$$V_0 = \frac{4\pi}{3} r_0^2 z_0. \tag{3.1.5}$$

Increasing the temperature by an amount ΔT results in a volume change of

$$\Delta V = \beta_T V_0 \Delta T \tag{3.1.6}$$

where β_T is the thermal coefficient of volume expansion. Expressing the new volume as $V = V_0 + \Delta V$ and assuming expansion only along the major axis, the expression for the major axis length as a function of temperature change is

$$r(\Delta T) = r_0 \sqrt{1 + \beta_T \Delta T} \tag{3.1.7}$$

The axis ratio R is therefore a function of temperature change as

$$R(\Delta T) = \frac{z}{r} = \frac{R_0}{\sqrt{1 + \beta_T \Delta T}} \tag{3.1.8}$$

where $R_0 = z_0/r_0$, the oblate axis ratio prior to heating.
Expansion confined along the major axis alters the shape parameter η such that

$$\eta(\Delta T) = \frac{R_0}{\sqrt{1 + \beta_T \Delta T - R_0^2}} \tag{3.1.9}$$

and the focal length a of the nanoparticle is written

$$a(\Delta T) = \frac{r_0 \sqrt{1 + \beta_T \Delta T}}{\sqrt{\eta(\Delta T)^2 + 1}} \tag{3.1.10}$$

3.1.3 Consequences of Shape Shifts

Changes in η and a due to thermal expansion have subtle consequences on the polarizabilities α_i, and as a result, the scattering and absorption cross-sections, σ_{sca} and σ_{abs}. Changing η will result in the resonance conditions ϵ_{lm} of the particle changing and therefore the wavelength of light that resonance occurs. In this section, ϵ is taken as E. Palik's data [47] and is constant with temperature. The resonance condition ϵ_{1m} for oblate spheroids, equation (2.2.12) and reprinted below, is sensitive to changes in η

$$\epsilon \rightarrow \epsilon_{1m} = \left.\frac{P_{1m}(i\eta)dQ_{1m}(i\eta)}{Q_{1m}(i\eta)dP_{1m}(i\eta)}\right|_{\eta=\eta_0}.$$

For isotropic expansion, η is constant and there is no shift in ϵ_{1m}. Only for anisotropic expansion will ϵ_{1m} change as a result of η. Figure 3.1 shows η vs. T for an oblate spheroid with an initial minor-major axis ratio R_0=0.5. η decreases with increasing temperature over the range 295K to 1295K. Au melts at 1337K so temperature ranges are restricted to the solid phase.

Figure 3.2 shows the real part of ϵ_{1m} as a function of temperature change for anisotropic expansion. The $m = 0$ case increases, becoming less negative, with increasing temperature. The $m = 1$ case decreases, becoming more negative, with increasing temperature. The changes in both functions are around 2% of T_0 values over the temperature range 295K-1295K and is entirely due to the magnitude of β_T. The imaginary parts of ϵ_{1m} are constant with respect to temperature over the range 295K-1295K and therefore are not shown.

The expressions for nanoparticle polarizabilities α_i $(i = x, y, z)$, equations (2.2.11) and reprinted below, include both now temperature-dependent terms ϵ_{lm} and a.

$$\begin{aligned}
\alpha_x =& \frac{2a^3[\epsilon - 1]\sqrt{(1+\eta^2)}}{3Q_{11}(i\eta)[\epsilon - \epsilon_{11}(i\eta)]} \\
\alpha_y =& \frac{2a^3[\epsilon - 1]\sqrt{(1+\eta^2}}{3Q_{11}(i\eta)[\epsilon - \epsilon_{11}(i\eta)]} \\
\alpha_z =& \frac{-a^3\eta[\epsilon - 1]}{3Q_{10}(i\eta)[\epsilon - \epsilon_{10}(i\eta)]}
\end{aligned} \tag{3.1.11}$$

Figure 3.3 shows how increasing temperature will alter α_x for the anisotropic case; both the real and imaginary parts increase with temperature. This is due to the expanding nanoparticle focal length a, resulting in the magnitude of the polarizability changing as a^3. There is a very small blue-shift of $\sim$ 1nm in the polarizability maxima over the temperature range 295K to 1295K. It should be noted that ϵ is not temperature dependent so far in this analysis and only the thermal expansion of the spheroid is considered. Similar curves for α_x for the isotropic case have been generated, but are not presented. The difference between α_x for the isotropic and anisotropic cases are so small as to make the figures appear very similar. Instead, Figure 3.4 shows the difference in α_x for the isotropic and anisotropic cases as a function of temperature.

Figure 3.5 shows the total cross-section for p-polarization, σ_{tot}^p, as function of wavelength at four temperatures for the anisotropic case.

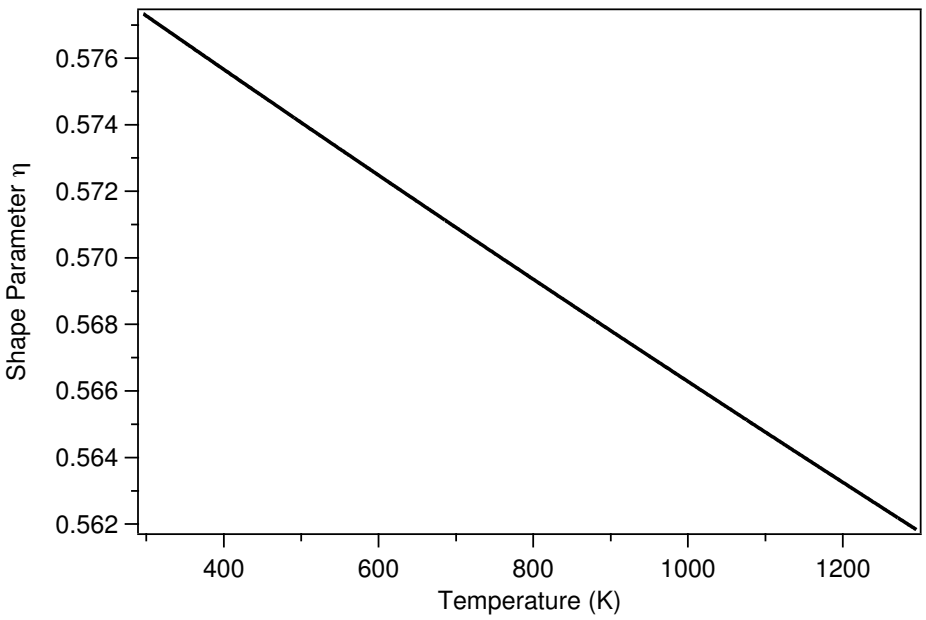

Figure 3.1: η vs. T for an oblate spheroid with the initial dimensions $r_0 = 20$nm, $z_0 = 10$nm, $R_0 = 0.5$ in the anisotropic expansion case. For isotropic expansion, η remains constant.

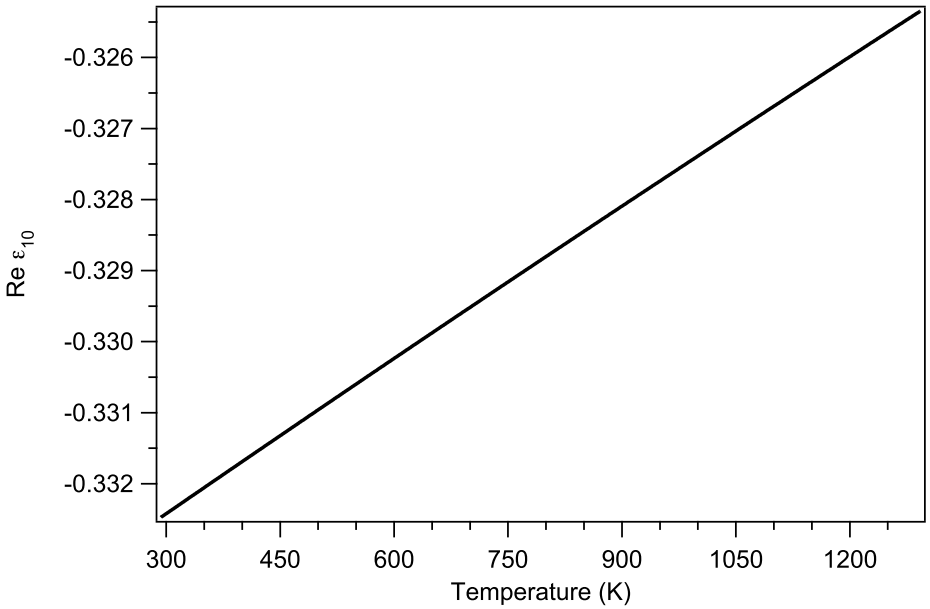

(a) The real part of the resonance condition ϵ_{10} as a function of temperature.

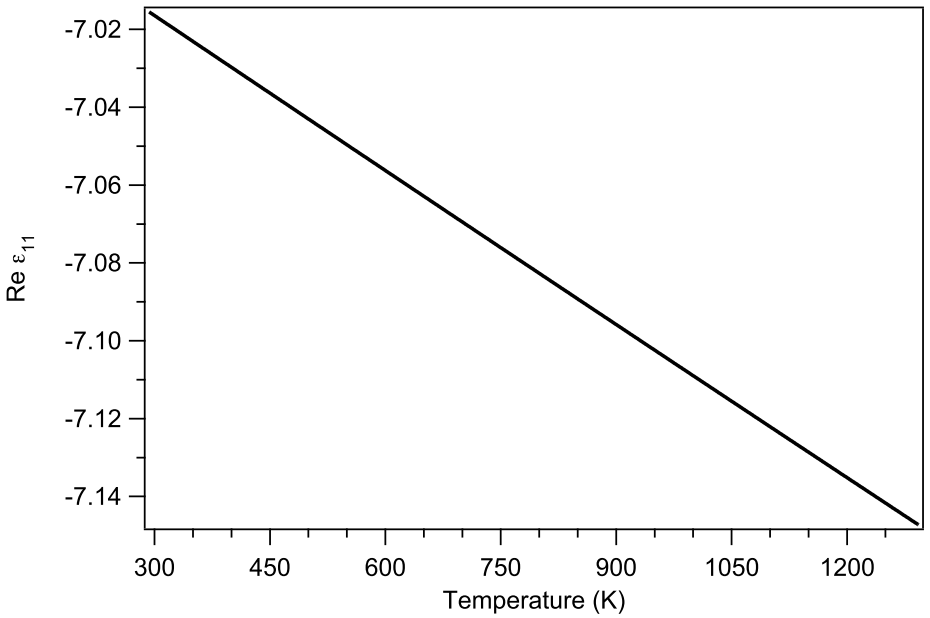

(b) The real part of the resonance condition ϵ_{11} as a function of emperatures.

Figure 3.2: The resonance condition ϵ_{1m} as a function of temperature for the anisotropic expansion case.

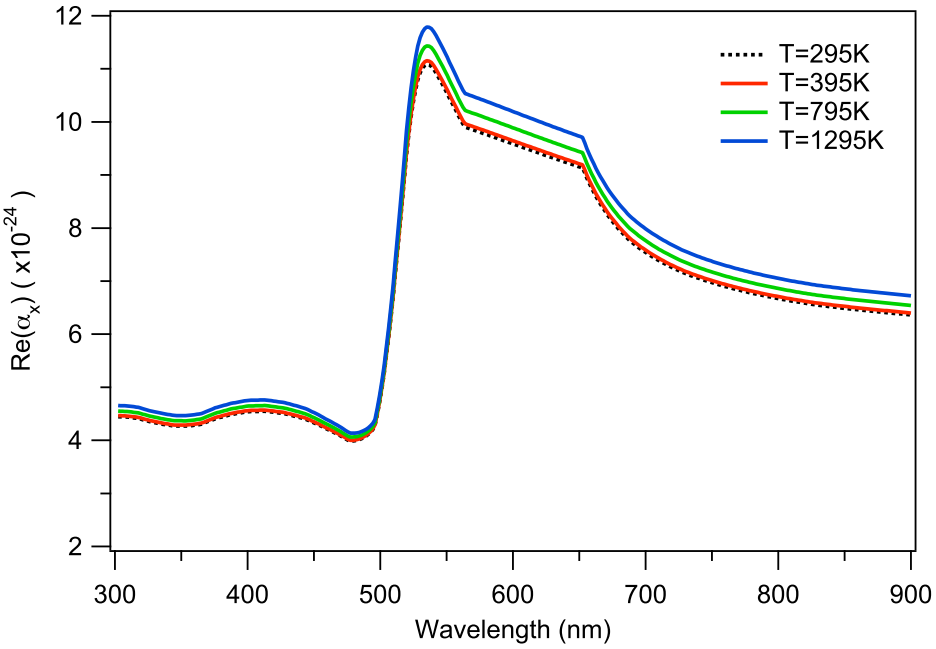

(a) The real part of α_x as a function of temperature.

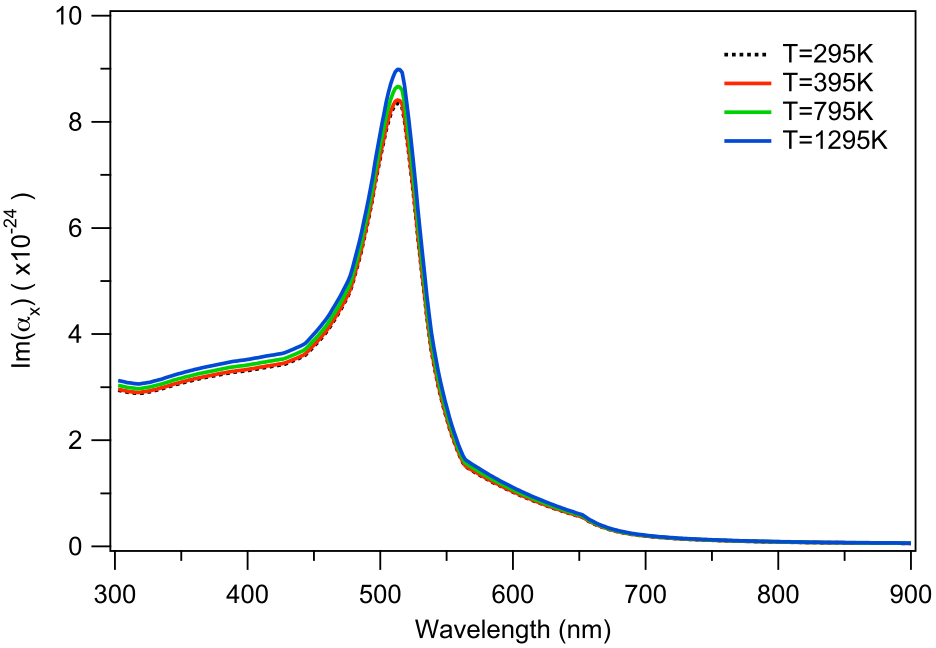

(b) The imaginary part of α_x as a function of wavelength at four temperatures.

Figure 3.3: The real and imaginary parts of the polarizability along the major axis, α_x, as a function of wavelength for an oblate spheroid dimensions $z_0 = 10$nm, $r_0 = 20$nm, $R_0 = 0.5$ at four different temperatures assuming and anisotropic expansion. The dielectric function of Au, taken from E. Palik, is constant with respect to temperature.

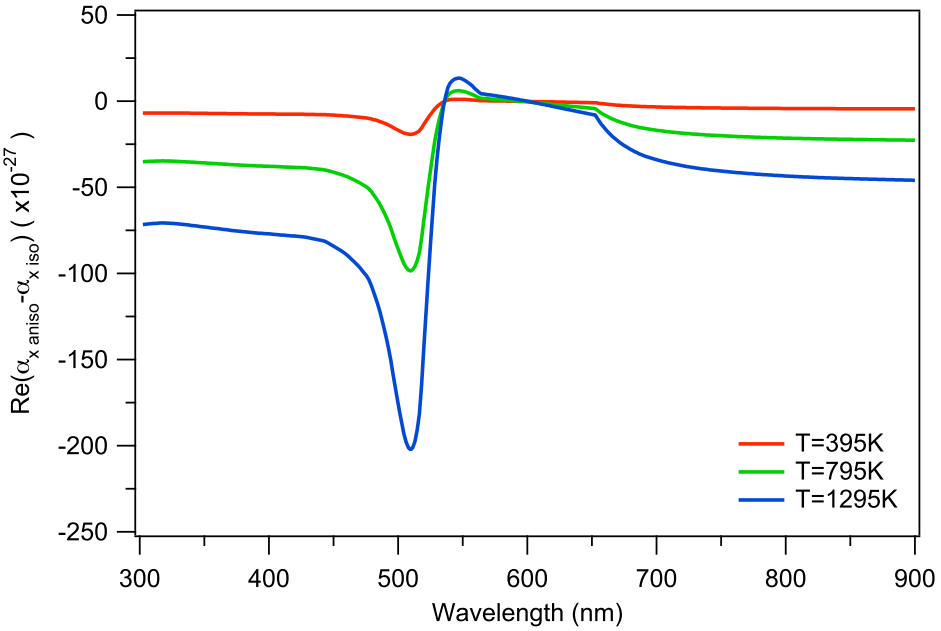

(a) The real part of $\alpha_{xaniso} - \alpha_{xiso}$ as a function of wavelength at four temperatures.

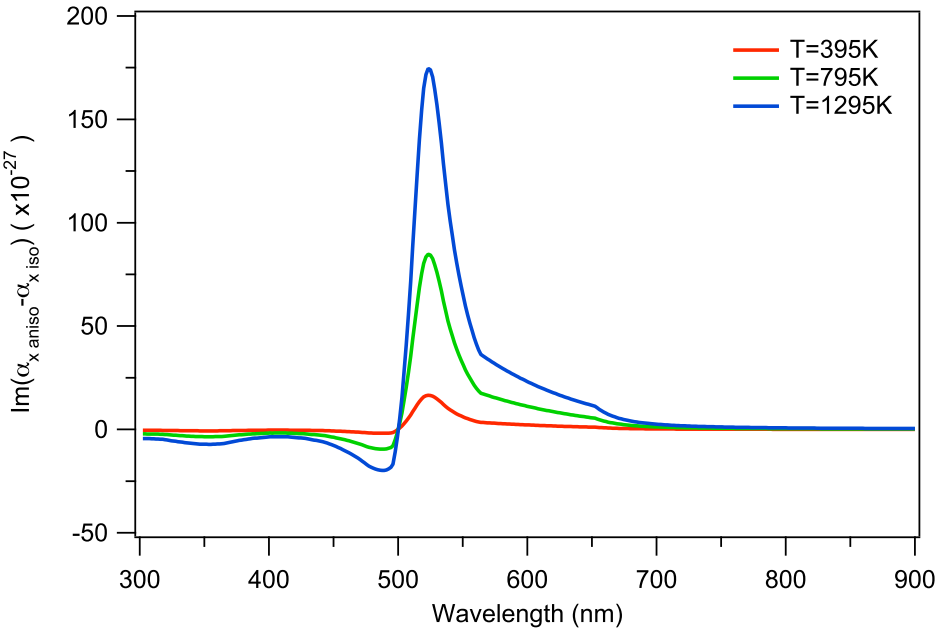

(b) The imaginary part of $\alpha_{xaniso} - \alpha_{xiso}$ as a function of wavelength at four temperatures.

Figure 3.4: The differences in the polarizability α_x between isotropic and anisotropic expansion cases.

Figure 3.6 shows $\sigma^p_{abs}/\sigma^p_{scat}$ vs. wavelength at four temperatures using E. Palik's data. Peak position is const. with temperature. Although both abs and scat increase with temperature, the ratio decreases due to greater proportional increase in scat than abs cross sections.

Ultimately the thermal expansion of an oblate spheroid results in very subtle changes in the optical response. With increasing temperature, there is a small increase in the polarizabilities, hence the cross-sections, due to the increased focal length a. However, it should be noted that attention is only focused on the physical effects of increased temperature. Temperature dependence of the dielectric function itself needs to be taken into account to investigate how the polarizabilities, therefore the cross-sections, change with increasing temperature. If, in practice, a shift in the absorption spectra does occur, it will most likely be due to the temperature dependence of the dielectric function itself.

3.2 Temperature Dependence of ϵ

The resonance conditions for exciting surface plasmons on spheroids are very sensitive to changes in the dielectric function ϵ. The consequences of increased temperature on the dielectric function must be considered in order to fully appreciate the problem at hand.

There is a great deal of experimental evidence showing pronounced changes in the dielectric function of noble metals as a result of current, electric field, stress and temperature modulation [48] [49] [50]. Prior to the 1990s, temperature dependence of the dielectric function was the realm primarily of solid state theorists studying changes in band structure and absorption edges [51] [52] [53] [54]. It is only recently [41] [40] [46] [55] [56] [57] [58] that this work has become of more importance with practical applications such pulsed heating of metallic nanoparticles.

Although many workers [59] [60] [61] have attempted to quantify the temperature dependence of ϵ, attention has only focused on the variation of one or two terms, usually the free electron damping factor γ_f and the Fermi-Dirac distribution function $f(E)$.

There is no obvious inclusion of temperature dependence in the Drude-Lorentz dielectric function (DLDF) introduced in Chapter 2. In order to consider temperature dependancy, the DLDF must be modified to be more realistic in describing the actual dielectric function of noble metals, in particular, Au. The goal is to develop a numerical approach that generates realistic values of the dielectric function $\epsilon(T)$ for Au. These numerically-obtained dielectric functions shall be denoted $\epsilon^{num}(T)$ for clarity.

In what follows, modifications to the DLDF are made using well-known techniques and experimental data from band structure calculations, pulsed laser heating experiments and optical constant measurements. Terms within the DLDF are analyzed for temperature dependence and recast in a specific temperature dependent form. There are three broad areas where a change in temperature will affect the DLDF: volumetric expansion; increase of scattering processes; and alterations to the band structure. All initial (T=295K) parameters and temperature dependent coefficients are obtained from a variety of sources from the literature.

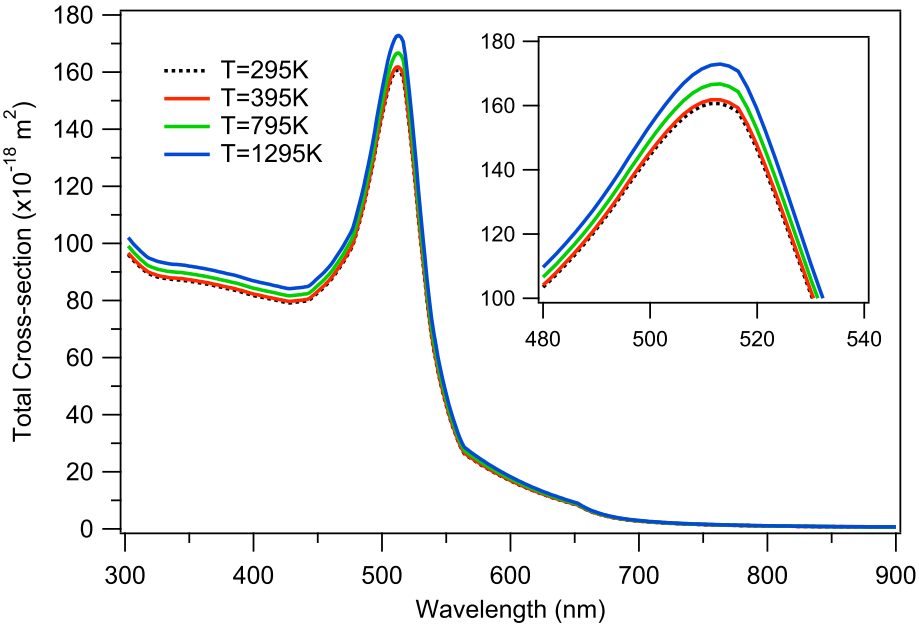

Figure 3.5: The total p-polarized cross-section, σ_{tot}^{p}, as a function of wavelength for an oblate spheroid dimensions $z_0 = 10$nm, $r_0 = 20$nm, $R_0 = 0.5$ at four different temperatures in the anisotropic case. E. Palik's data is taken for the dielectric function and is constant with respect to temperature. The inset shows the region 480nm-540nm in detail.

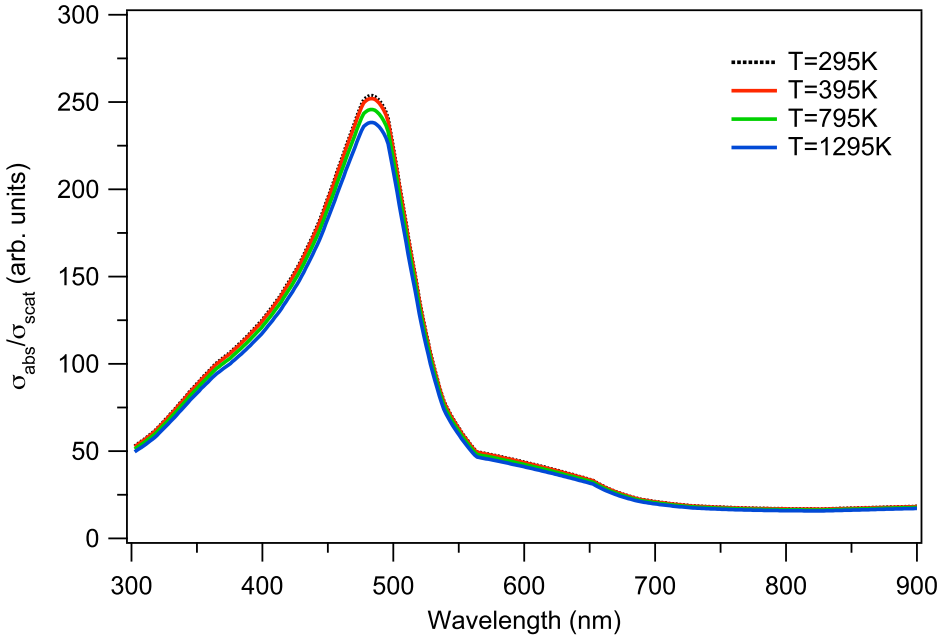

Figure 3.6: $\sigma^p_{abs}/\sigma^p_{scat}$ for an oblate spheroid dimensions $z_0 = 10$nm, $r_0 = 20$nm, $R_0 = 0.5$ at four different temperatures in the anisotropic case. E. Palik's data is taken for the dielectric function and is constant with respect to temperature.

3.2.1 Modifications to the Bound Contribution

The Drude-Lorentz dielectric function (DLDF) for a metal is reprinted below.

$$\epsilon(\omega) = 1 + \sum_{j=0}^{N} \frac{f_j \omega_p^2}{(\omega_j^2 - \omega^2) - i\gamma_j \omega} \tag{3.2.1}$$

The DLDF is modified to be more realistic in application to noble metals by replacing the bound contribution with a method first introduced by Rosei [50]. Instead of assuming the electrons have a continuous range of energies of which some are bound, the important interband transitions are described as transitions from a flat d-band to a parabolic conduction band. Not only does this offer some attempt to quantize the model, it introduces the concept of an energy gap separating the d-band and the conduction band which does not exist in the classical Drude-Lorentz model. Making this substitution effectively averages over all interband transitions, replacing ω_j with a single damping factor γ_b.

Electronic transitions from the d-band to the conduction band (i.e., having energy greater than the gap energy $\hbar\omega_g$) are interband transitions and contribute to ϵ_b. Transitions from below to above the Fermi energy, but restricted to the same electronic band, are intraband transitions. These electrons are often referred to as 'free' electrons in the Drude model, having a continuum of low energy excitations. The bound-electron contribution to the dielectric function can be cast as

$$\epsilon_b(\omega) = K \int_{\omega_g}^{\infty} [1 - f(E)] \frac{\sqrt{x - \omega_g}}{x} \frac{1}{(x + \omega + i\gamma_b\omega)(x - \omega - i\gamma_b\omega)} dx \tag{3.2.2}$$

where K is a constant, ω_g is the energy gap frequency, $f(E)$ the Fermi-Dirac distribution function. There is no analytic solution to equation (3.2.2) and therefore it shall require numerical methods to evaluate. The major advantage of this approach is that it simplifies the computation significantly. One major disadvantage is that some transitions, particularly in the low wavelength regime where interband transitions are dominant, are poorly described by this method.

3.2.2 The Plasma Frequency ω_p

There is no specific temperature dependence in the expression for the plasma frequency ω_p. However, temperature dependence is via two phenomena: the electron density n and effective electron mass m_e^*. Again assuming a volumetric expansion proportional to temperature change

$$\Delta V = \beta_T V_0 \Delta T.$$

The expansion of the unit cell effectively reduces the electron density by a factor of $(1 + \beta_T \Delta T)$. The change in m_e^* is more complex to analyze. Strictly speaking, the effective electron mass in a crystal lattice is defined as

$$m_e^* = \hbar^2 \left(\frac{d^2 E}{dk^2} \right)^{-1} \tag{3.2.3}$$

and is related to the curvature of the energy bands in k-space. There is no definitive expression for how the band structure of Au warps as a function of temperature so direct calculation of the effective electron mass is not yet possible. Instead, assuming the effective electron mass is inversely proportional to T such that

$$m_e^*(\Delta T) = \frac{m_{e0}^*}{(1 + \Theta_m \Delta T)} \tag{3.2.4}$$

where Θ_m is the thermal coefficient of effective electron mass. Estimates shall be made for Θ_m by evaluating ω_p at different temperatures, then calculating the influence of the lattice expansion on ω_p to find the resultant change in the effective mass term. The expression for the plasma frequency is recast as a function of temperature change

$$\omega_p(\Delta T) = \omega_{p0} \sqrt{\frac{1 + \Theta_m \Delta T}{1 + \beta_T \Delta T}} \tag{3.2.5}$$

where ω_{p0} is the initial plasma frequency, taken at T=295K in this work.

3.2.3 The Gap Energy $\hbar\omega_g$

$E_g = \hbar\omega_g$ is the energy gap from the upper d-band ($L_{5^+ + 6^+}$) to the Fermi level (E_F), corresponding to the interband absorption edge in Au. Figure (3.7) shows the relativistic augmented-plane-wave (RAPW) calculated band structure for Au from Ref. [52]. Temperature change is known to alter the band structure by warping and broadening the energy levels. This is a consequence of volume expansion by increasing the lattice spacing. As the temperature is increased, changes in the band structure must be considered. The gap energy shift is assumed to be linear over the range of temperatures below the melting point. It is this value used in the determination of $\hbar\omega_g(\Delta T)$.

$$\hbar\omega_g(\Delta T) = \hbar\omega_{g0} + \xi \Delta T \tag{3.2.6}$$

where ξ is the thermal coefficient of the bandgap shift.

3.2.4 The Electron Damping Terms γ_i

The electron damping terms γ_i are due to electron collisions with other electrons, lattice phonons, defects, impurities and the surface. Considering a linear relationship with respect to temperature over the range of interest and with no distinction as yet between the free and bound electron damping terms, leads to

$$\gamma(R, T) = \gamma_0 + \kappa_i T + \frac{C v_f}{r} \tag{3.2.7}$$

where γ_0 are the bulk values at T_0 , κ_i (i=b (bound) or f (free)) are the thermal coefficients of damping, C is an appropriate scaling factor (0.1 to 2.0 depending on the sample size and configuration as reported in the literature), v_f the Fermi velocity in Au and r the radius of the nanoparticle in question. However, it has been shown experimentally [62] that the size dependent term is negligable for particles on the order of $r \lesssim 1$nm therefore the size dependent term is neglected in this work.

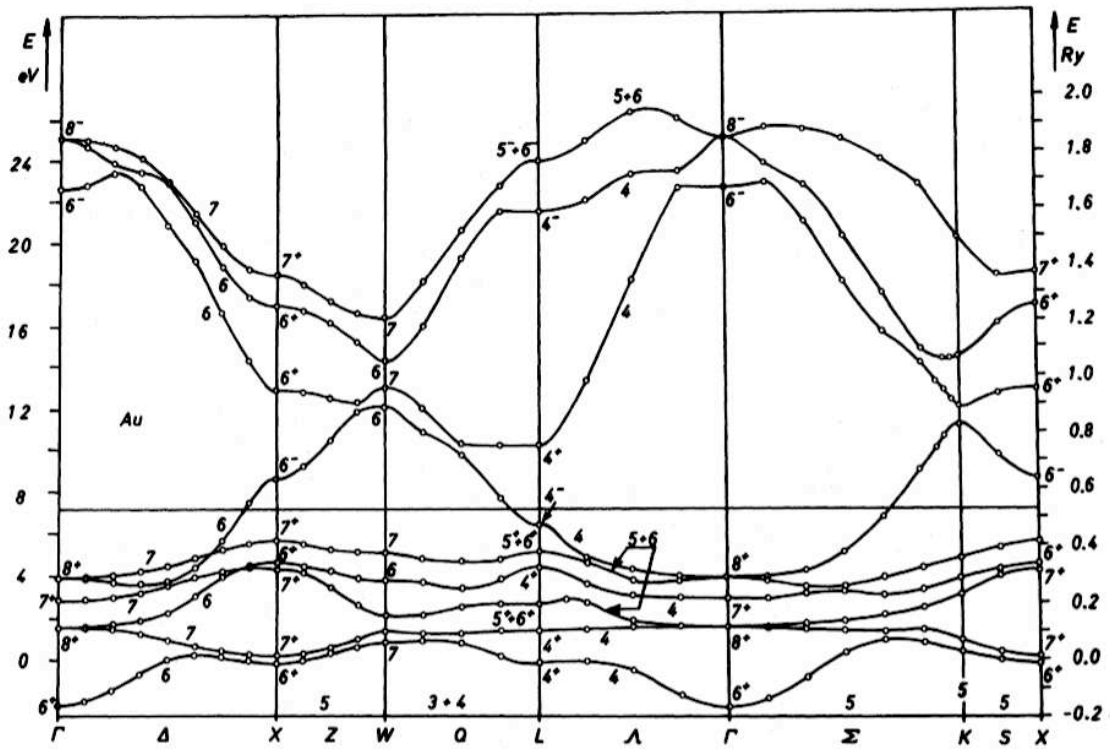

Figure 3.7: The relativistic augmented-plane-wave (RAPW) calculated band structure for Au from Christensen & Seraphin.

3.2.5 The Chemical Potential $\mu(T)$ and Fermi-Dirac Distribution $f(E)$

The Fermi-Dirac distribution function $f(E)$ is

$$f(E) = \frac{1}{e^{\frac{(\hbar\omega - E_F)}{kT}} + 1} \tag{3.2.8}$$

with the Fermi energy E_F defined as [63]

$$E_F = \frac{\hbar^2}{2m}(3\pi^2 n_0)^{2/3}. \tag{3.2.9}$$

where n_0 is the number density of electrons at $T = 0$K. E_F is only defined as such at $T = 0$K. For $T > 0$K, E_F is replaced with the chemical potential $\mu(T)$, with $d\mu(T)/dT$ generally being negative. The temperature dependence of equation (3.2.9) is a result of volumetric expansion on n_0 which, as shown above, effectively reduces n_0 by a factor of $(1 + \beta_T \Delta T)$. A simplistic expression for the temperature dependent chemical potential is

$$\mu(T) = \frac{E_F}{(1 + \beta T)^{2/3}} \tag{3.2.10}$$

Note that equation (3.2.10) refers specifically to T, not ΔT, as E_F is evaluated from $T = 0$K.

3.3 Determination of Variables

The most widely cited source of optical constants for many materials is the volume edited by E. Palik [47]. For Au in the visible and IR spectral ranges, Palik uses data obtained by Thèye [64] ($\lambda = 260$nm to 2.5μm) and by Dold & Mecke [65] ($\lambda = 2.0\mu$m to 9.9μm). These authors used thin-films of various thickness evaporated onto glass substrates from which optical constants were obtained by measuring the absorption coefficient $2nk/\lambda$. The imaginary part ϵ'' is extracted and then Kramers-Kronig analyzed to obtain real part ϵ'.

The measured optical data are very dependent on the sample, leading to a large range of values for a particular material. An excellent account is given by Thèye [64] and Aspnes [66]. Factors such as the fabrication method, substrate material, preparation method and annealing processes all lead to large variations in the measured optical data, influencing the analysis of data and leading to differences in ω_p and γ_f from sample to sample. This is illustrated in Figure 3.8 which shows the imaginary part of the dielectric function of Au as measured by three sources.

In this section, ϵ will be compared between several sources in order to determine reasonable initial values of ω_{p0} and γ_0, together with their temperature dependent coefficients Θ_m, κ and the thermal coefficient of bandgap shift, ξ. As different sources are used in the obtaining the values of constants and variables in this work, the reader should expect some deviation and disagreement between sources. For the most part, values are obtained by applying fitting routines to ϵ data unless the authors have specifically calculated relevant values.

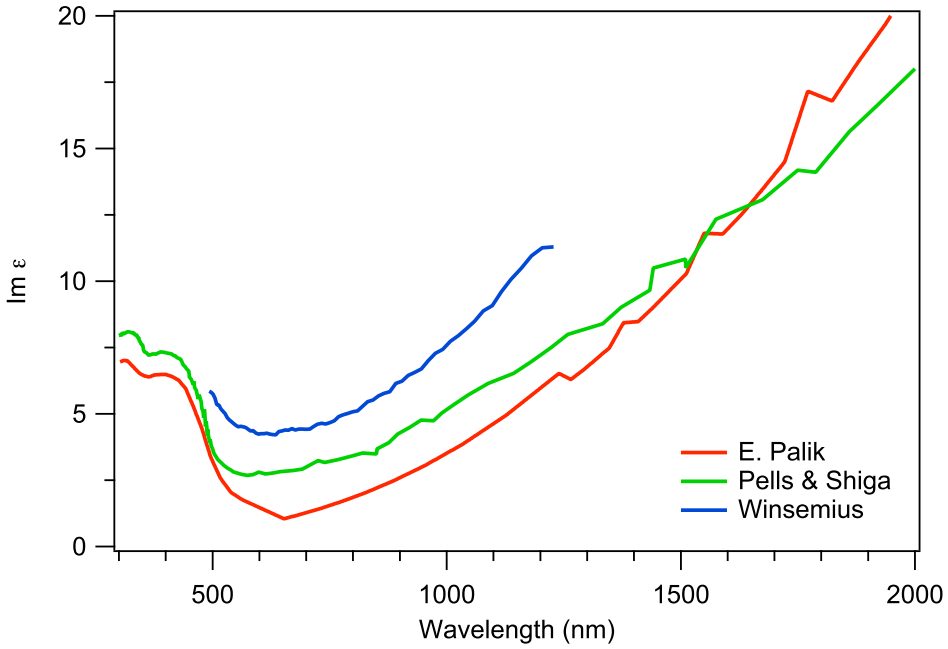

Figure 3.8: The imaginary part of the dielectric function of Au as measured by Winsemius and Pells & Shiga, and included in the volume by Palik.

3.3.1 Plasma Frequency ω_p & Free-Electron Damping Term γ_f

Values for ω_p and γ_f can obtained by fitting the Drude function to available Au dielectric function data. The Drude functions for real and imaginary parts are

$$\epsilon' = 1 - \frac{\omega_p^2}{(\omega^2 + \gamma_f^2)} \tag{3.3.1}$$

and

$$\epsilon'' = \frac{\omega_p^2 \gamma_f}{\omega(\omega^2 + \gamma_f^2).} \tag{3.3.2}$$

Accurate fits are obtained by applying the fitting routines to data with energies below the interband absorption threshold (1.84 eV, λ = 674nm for Au) as there is very little contribution from the bound regime. Ideally, ϵ data should extend as far into the IR as possible to obtain the most accurate results from the free electron contribution.

Figure (3.9) shows the fit graphs for both the real and imaginary parts obtained from E. Palik (ϵ^{Pal}). Figure (3.10) shows the fit graphs for the imaginary part obtained from Winsemius *et al.* [54] (ϵ^{Win}), who measured the optical properties of Au using the polarimetric method of Beattie [67] at several temperatures on polished samples of bulk Au. In particular, Winsemius ascribes an 'effective temperature' T^* to analyze the data. Pells & Shiga (PS) [59] measured optical properties of polished and annealed Au bulk samples in vacuum using the same method at temperatures of 295K, 470K and 670K. Their analysis on the imaginary part in the free-electron (IR) region provides values for ω_p and γ_f. Table 3.1 presents the values of ω_p and γ_f obtained from Pells & Shiga and from fitting with Palik and Winsemius.

To highlight the difficulties of obtaining accurate data from sample to sample for the optical properties of Au, compare the differences between fit values obtained from Palik's data and Pells & Shiga's data. Dold & Mecke make no specific remarks regarding the sample temperature during measurement. Thèye remarks that her measurements were taken from room temperature to 100°C, but gives no specifics, resulting in some degree of uncertainty.

Winsemius' data was taken in the 1.0-3.5 eV (λ = 354nm-1.24μm) range and does not extend far enough into the IR to enable the Drude function to be fit with much accuracy, resulting in values for γ_f which are an order of magnitude or greater different from Palik and Pells & Shiga. Only Pells & Shiga give data for ϵ'' over a wide enough spectral range and at specific temperatures.

However, one can infer general ranges and trends from the data in table 3.1. ω_p lies in the 1×10^{16} rad/s range and increases with temperature; γ_f is less accurate, being in the 1-10 $\times$ 10^{14} rad/s range and also increases with temperature. The large variation in γ_f is almost entirely attributable to sample type and preparation methods as scattering from impurities, defects, surface roughness, material grain size boundaries are the dominant macroscopic effects.

Pells & Shiga's data allows estimates on the values for Θ_m and κ_f, the thermal coefficients of effective electron mass and free-electron damping frequency respectively, finding $\Theta_m = 1.613 \times 10^{-4}$/K and $\kappa_f = 1.047 \times 10^{12}$rad/s K.

Experiments by Inouye [61] determined $\kappa_f = 6.51 \times 10^{10}$ rad/s K, a difference of over an order of magnitude from the result compared to Pells & Shiga's data. The difference in the

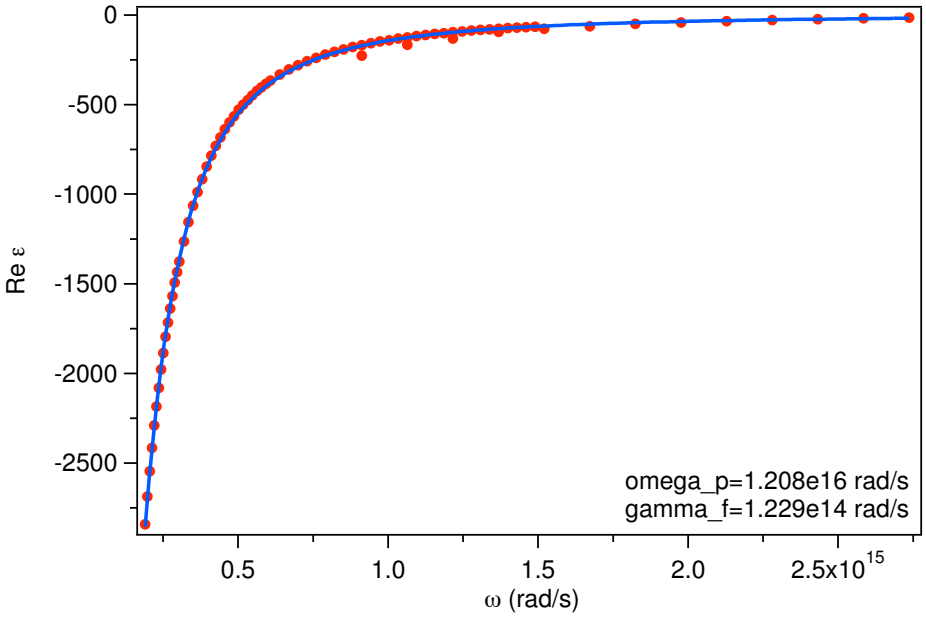

(a) The real part of ϵ^{Pal} (points) with fit (line)

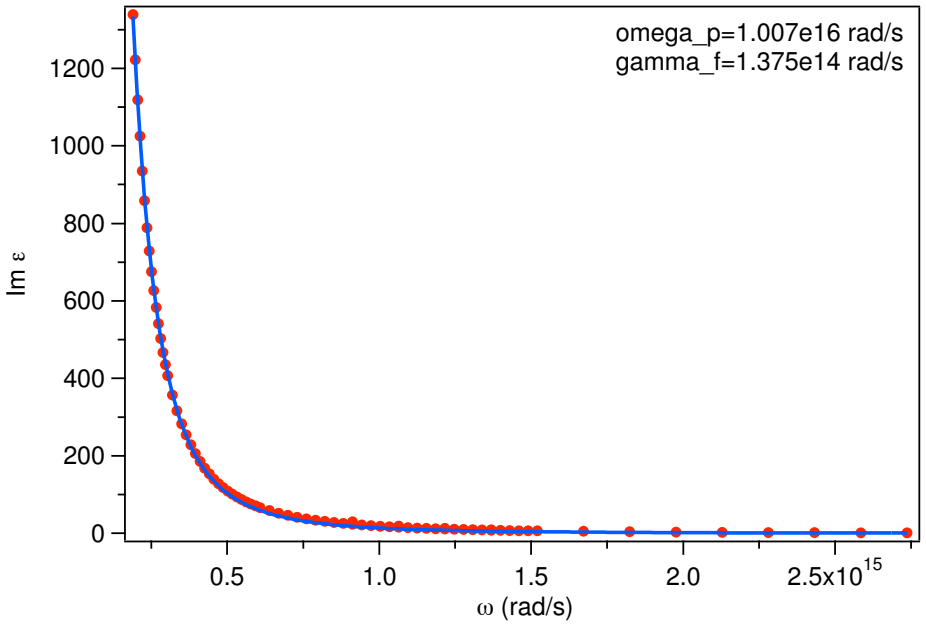

(b) The imaginary part of ϵ^{Pal} (points) with fit (line)

Figure 3.9: Fitting ϵ^{Pal} to the Drude model in the visible-IR range.

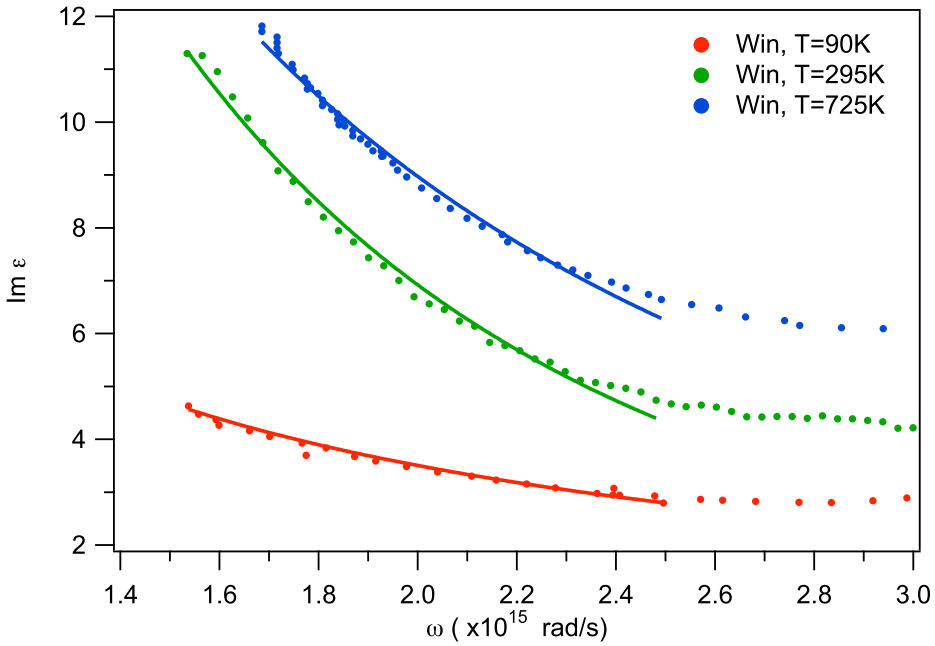

Figure 3.10: The imaginary part of ϵ^{Win} (points) with fits to the Drude model (lines) for data obtained at temperatures of 90K, 295K and 725K.

Table 3.1: Values of ω_p and γ_f obtained from fitting to ϵ^{Pal} and ϵ^{Win}, and from analysis by Pells & Shiga. The numbers in square brackets [ ] for Winsemius' measurements indicate the effective temperature, T^*.

Source	Temperature (K)	ω_p ($\times 10^{16}$ rad/s)	γ_f ($\times 10^{14}$ rad/s)
Palik, Re	295-373	1.208 ± 0.001	1.229 ± 0.007
Palik, Im	295-373	1.007 ± 0.003	1.375 ± 0.016
Pells & Shiga	295	1.408	2.618
Pells & Shiga	470	1.452	4.488
Pells & Shiga	670	1.438	6.545
Winsemius	90 [450]	1.440	294.44
Winsemius	295 [600]	0.744 ± 0.002	20.077 ± 0.724
Winsemius	725 [1050]	0.902 ± 0.078	33.452 ± 1.130

values of κ_f is again likely due to experimental configurations and samples. Pells & Shiga used a large sample of highly polished Au in vacuum with the temperature held constant during measurement. Inouye fabricated spherical gold nanoparticles embedded in a glass matrix by sputtering and used ultra-fast laser pulses to heat the nanoparticles to initially extremely high ($\sim$ 1700K) electron temperatures, measuring γ_f as a function of time after the pulse.

Although Inouye's work is more applicable here in a sample sense, i.e., using nanoparticles instead of bulk Au, his analysis was carried out at high electron temperatures and thus may be unrealistic to use in this work. Further analysis by Rashidi-Huyeh *et al.* [68] suggest that heat loss to the surrounding matrix was not taken into account, therefore giving a less accurate result for κ_f. Since nanoparticles in this dissertation are large enough to be considered bulk (i.e. no size-dependent effects) it is reasonable to assume κ_f from Pells & Shiga to be more accurate than the value arrived at by Inouye.

3.3.2 The Bound Electron Damping Term γ_b

Data from Inouye [61] is used to determine the initial bound electron damping term γ_{b0} and the thermal coefficient κ_b. There is a lack of data from other sources so objective comparisons cannot currently be made. Briefly, Inouye rapidly heated a nanoparticle-SiO_2 matrix using 200fs laser pulses and measured sample optical density with a probe beam tunable over the wavelength range λ=450nm-1.2μm as a function of time after the pulse. By applying Mie theory to the optical density signal, the free and bound electron contributions were found.

Inouye's data gives γ_b=2.40 $\times 10^{14}$ rad/s at T=301.5K, increasing to 2.47 $\times 10^{14}$ rad/s at $T_e \approx$ 1700K. T_e refers to the electron temperature, which is not thermalized with the lattice temperature T_l following pulsed heating. The thermal coefficient for the bound electron damping term κ_b is determined to be 5.42 $\times 10^9$ rad/s K.

3.3.3 The Energy Gap

Christensen & Seraphin [52] report that as the crystal lattice is expanded by 0.1 atomic units, mimicking a temperature increase of 920K, the top of the *d*-band is lowered by approximately 0.4 eV. The same calculations also show the Fermi energy decreasing by 0.45 eV with respect to the same zero, providing a value for ξ = -0.54 $\times 10^{-4}$ eV/K. Winsemius measured a temperature dependence of the energy gap in Au to be ξ = -1.7 $\times$ 10^{-4}eV/K, consistent with the Christensen band structure calculations showing the *d*-band decreasing with increasing temperature. The values of Winsemius shall be used in this work.

3.4 Numerical Modeling

Numerical modeling of the temperature dependent dielectric function is done using Maple with which powerful numerical techniques can be applied to evaluating the integral in equation (3.2.2). The numerically-generated dielectric functions are denoted $\epsilon^{num}(T)$ and are functions of wavelength ($\lambda = 2\pi c/\omega$) and temperature.

3.4.1 Variable Sweeps

Sweeps of all variables are carried out in order to investigate the resultant changes in ϵ^{num}. Spikes, oscillations and other suspicious features often appear in the bound contribution and are not representive of physical phenomena, but are singularities in the numerical evaluation of equation (3.2.2).

Using values obtained from the previous sections in this chapter, $\epsilon^{num}(T)$ are produced at arbitrary temperatures T over the range 295K to 1295K. These values are then input into various models, introduced in Chapter 5, to study the absorbance and differential reflectivity of nanoparticle samples which are then compared to experimental results.

In Figures 3.11-3.16, the real and imaginary parts of the dielectric function are displayed as Figures (a) and (b) respectively. Other variables are held constant as each is swept independently between $\pm$ 50% of initial values. Table 3.2 shows the initial parameters values and sweep ranges.

Figure 3.11 shows the resulting dielectric functions as the plasma frequency ω_p is varied. Increasing ω_p decreases the real part, but increases the imaginary part over the wavelength range of interest. The gradient in the visible and NIR ranges become more negative for the real part and more positive for imaginary part.

Figure 3.12 shows the resulting dielectric functions as the free electron damping term γ_f is varied. Increasing γ_f has little effect in the UV-blue parts of the spectrum as one would expect. However, in the visible and NIR, increasing γ_f tends to make the gradient of the real part more positive with increasing wavelength. For the imaginary part, the slope generally increases relatively uniformly throughout the visible-NIR region, with some gradient flattening and cross-overs occuring in the NIR at larger values of γ_f.

Figure 3.13 shows the resulting dielectric functions as the bound electron damping term γ_b is varied. As one would expect, this has the greatest influence on the bound contribution. Increasing γ_b increases the amplitude of the oscillations in the bound contribution for both the real and imaginary parts, but these are numerical artifacts. Physically, a larger bound electron damping term would increase the magnitude of the real and imaginary parts and have little effect on the free electron contribution. For the imaginary part, a smaller γ_b increases the negative gradient near the point of inflection (located near $\lambda \sim 490$nm) resulting in a lower value for the minima. Larger γ_b pushes the minima to both higher values and toward the red end of the spectrum. As the wavelength increases into the red and NIR, the influence of γ_b becomes less pronounced.

Figure 3.14 shows the resulting dielectric functions as the gap energy $\hbar\omega_g$ is varied. For both real and imaginary parts, a larger energy gap influences the crossover point between bound and free contributions. As the value of ω_g increases, the peaks in the real part decrease in magnitude and are shifted towards the blue end of the spectrum. The imaginary part responds similarly, with the mid-point of the main slope, initially positioned near $\lambda \sim$ 500nm, being blue-shifted to near $\lambda \sim 400$nm.

Figure 3.15 shows the resulting dielectric functions as the Fermi energy E_F is varied. Both the real and imaginary parts are displaced to the left as the bound contribution is given less influence in the visible range of the spectrum. The peaks also narrow for the real part and the minima in the imaginary part are shifted more negative and toward the red. The bound-free onset slope is steeper.

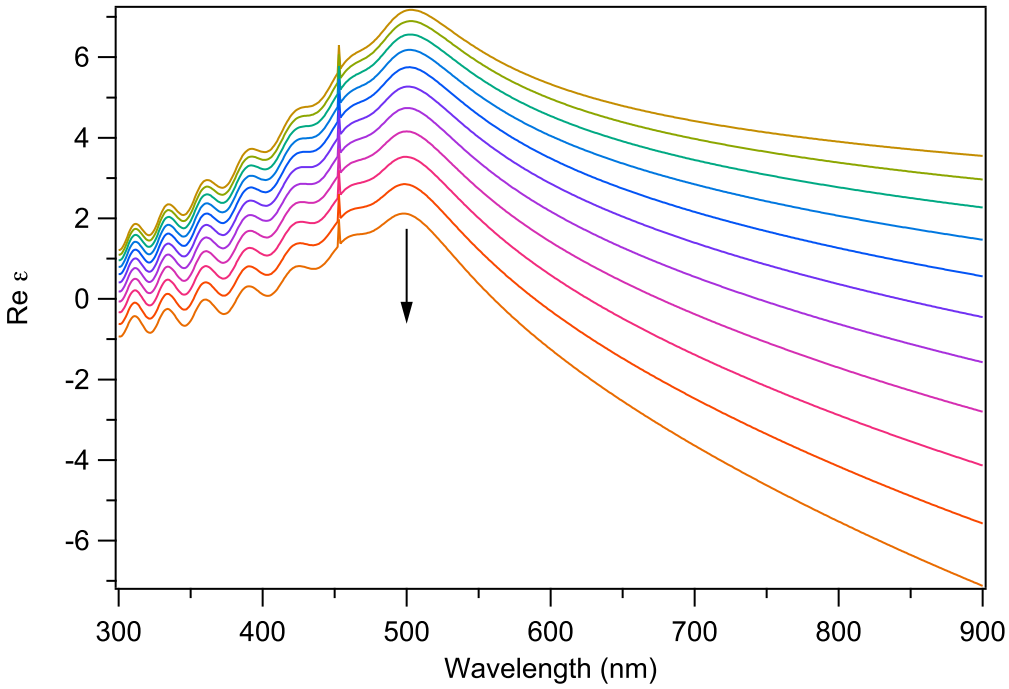

(a) Real part

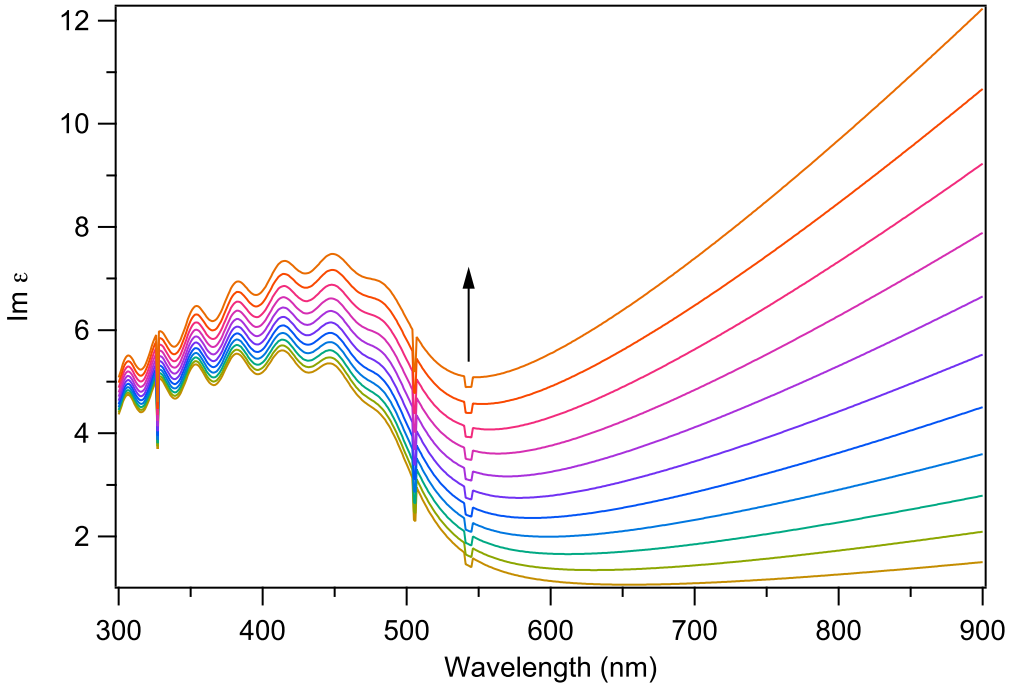

(b) Imaginary part

Figure 3.11: ω_p sweep over the range $\omega_p = 3.44 \rightarrow 10.32 \times 10^{15}$ rad/s. The arrow indicates increasing ω_p.

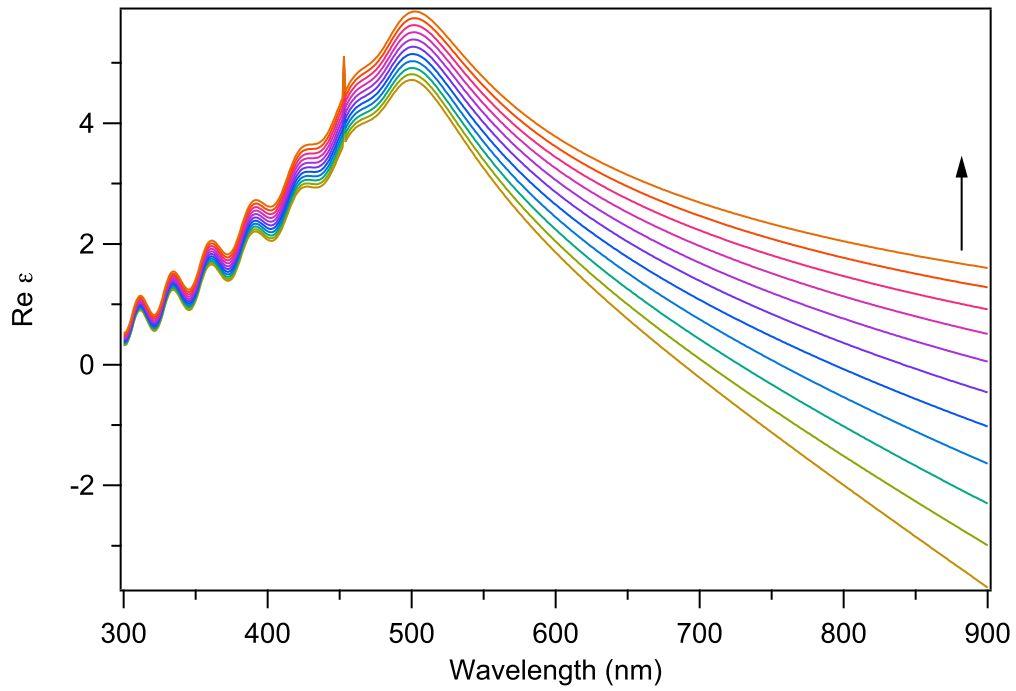

(a) Real part

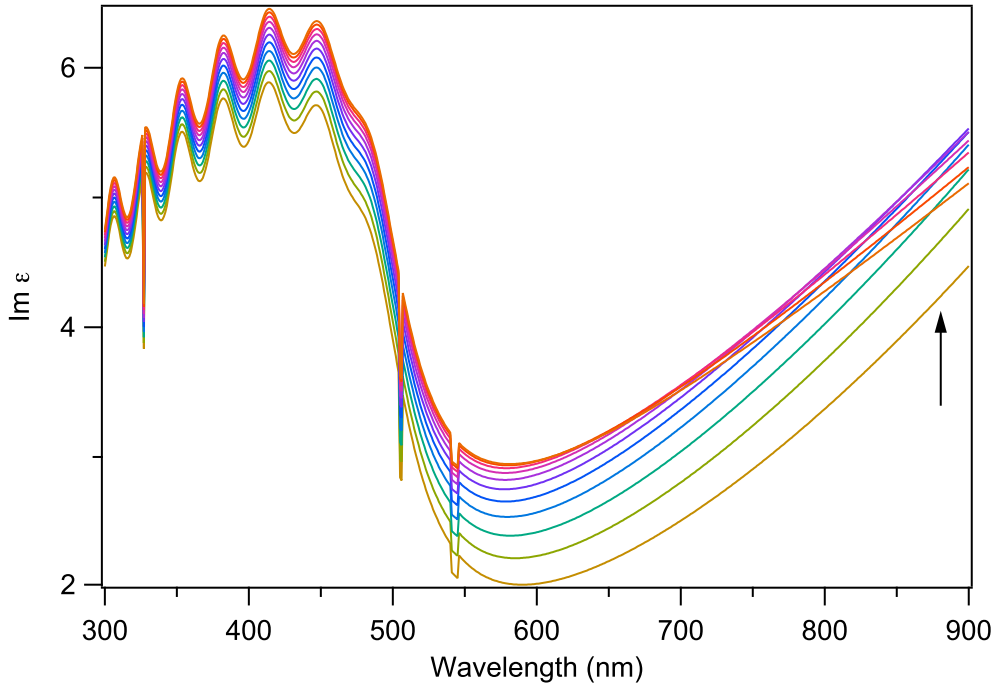

(b) Imaginary part

Figure 3.12: γ_f sweep over the range $\gamma_f = 1.05 \rightarrow 3.15 \times 10^{15}$ rad/s. The arrow indicates increasing γ_f.

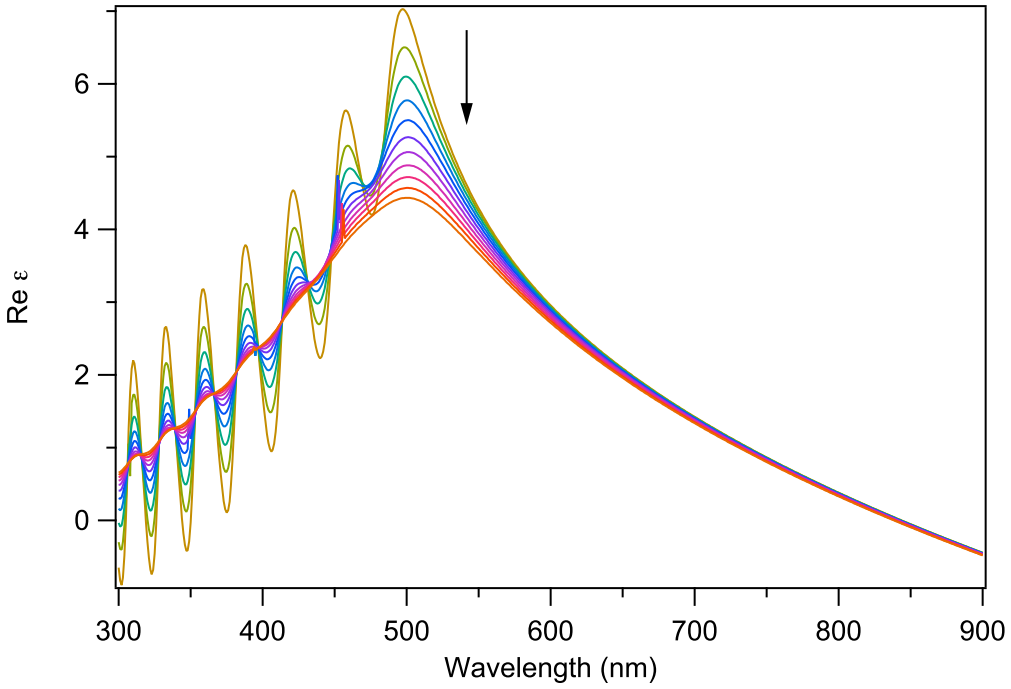

(a) Real part

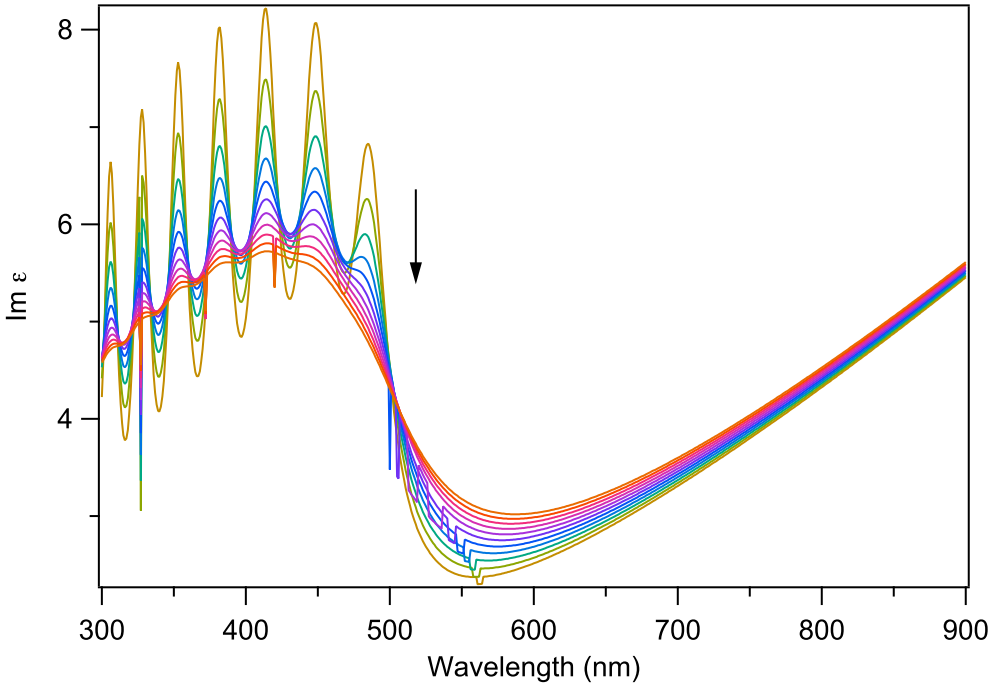

(b) Imaginary part

Figure 3.13: γ_b sweep over the range $\gamma_b = 1.2 \rightarrow 3.6 \times 10^{15}$ rad/s. The arrow indicates increasing γ_b.

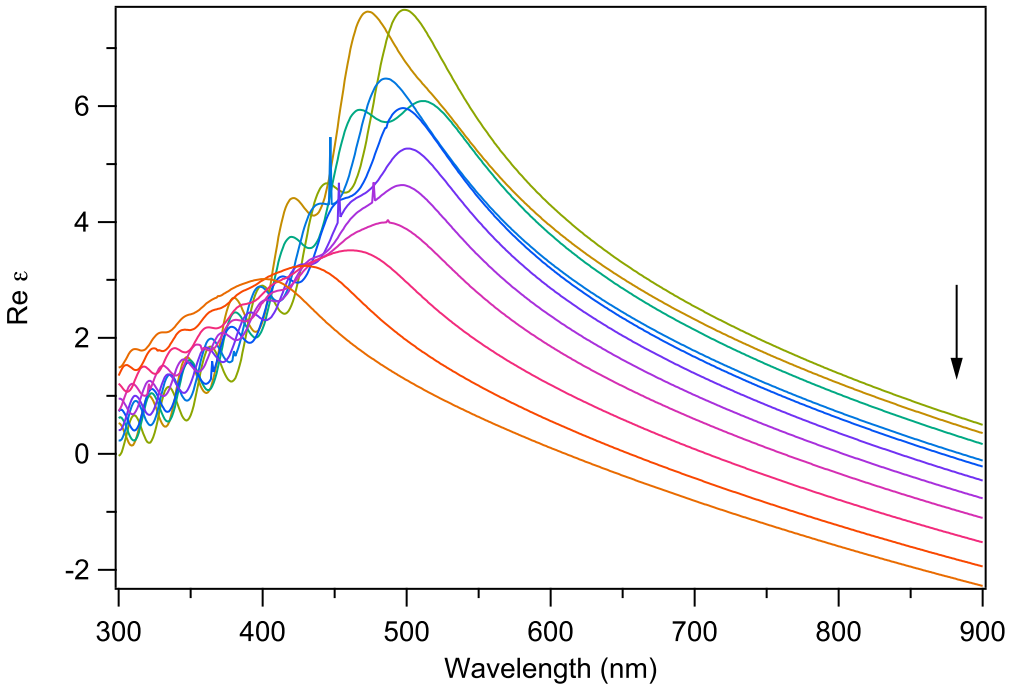

(a) Real part

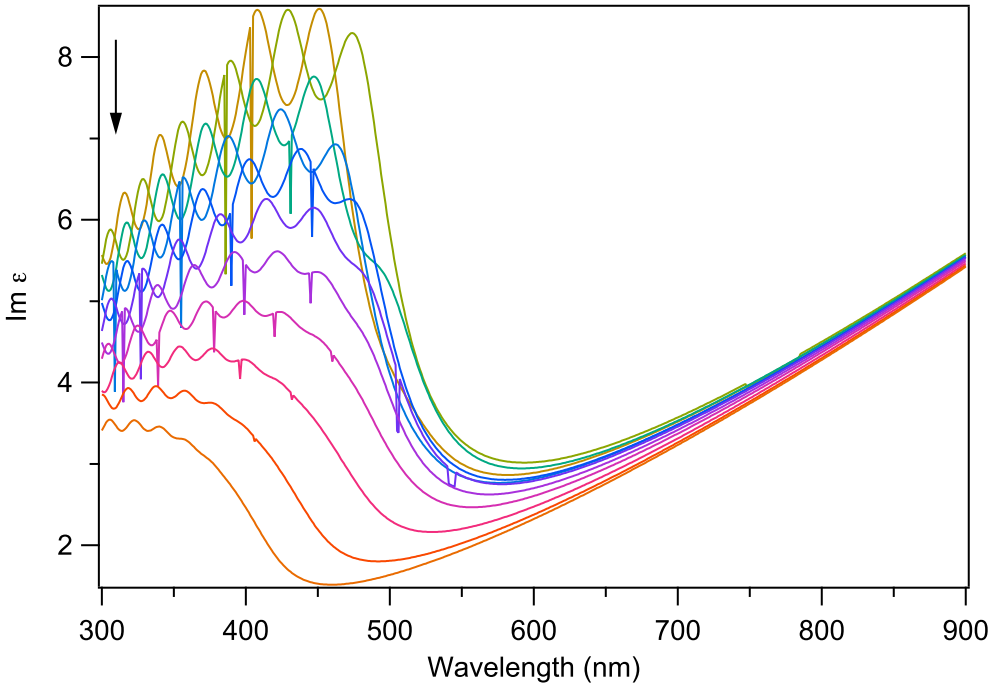

(b) Imaginary part

Figure 3.14: ω_g sweep over the range $\omega_g = 1.5 \rightarrow 4.5 \times 10^{15}$ rad/s. The arrow indicates increasing ω_g.

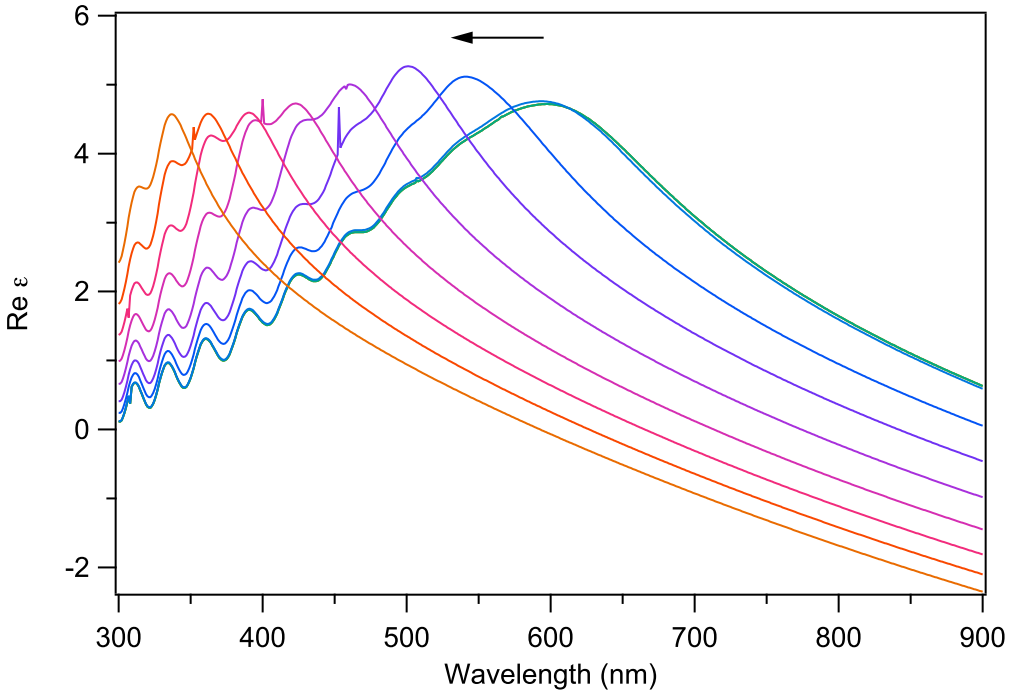

(a) Real part

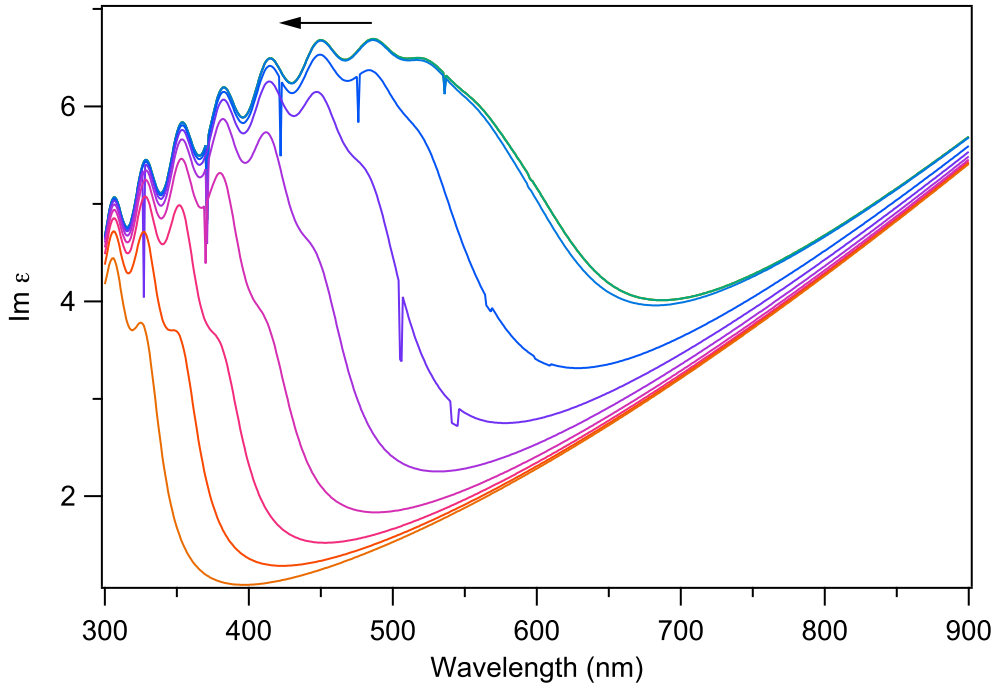

(b) Imaginary part

Figure 3.15: E_F sweep over the range $E_F = 1.25 \rightarrow 3.75$ eV. The arrow indicates increasing E_F.

Figure 3.16 shows the resulting dielectric functions as the integral upper limit (UL) value is varied. The integral in equation (3.2.2) is numerically evaluated with a finite upper limit instead of the infinite limit as printed. Using an infinite limit results in the computed bound contribution being exceedingly small. The initial value of the upper limit is chosen to be the ionization energy of Au. The real part experiences an approximately uniform increase across spectrum with increasing UL, with the oscillations due to numerical integration increasing in the bound contribution. The imaginary part looks haphazard, but enough detail is present to show that a larger UL increases oscillation amplitude. There is no influence in the visible-NIR regions.

3.4.2 Results & Discussion

The parameters used to generate $\epsilon^{num}(T)$ are given in Table (3.3), together with the temperature dependent variables established in previously in this chapter. Figure 3.17 present values of $\epsilon^{num}(T)$ over the temperature range T = 295K-1295K. As the temperature is increased, the values for the real part decrease over the wavelength range with the slope in the red-IR region becoming more negative. The opposite is true for the imaginary part, with the values increasing with increasing temperature and the slope in the red-IR region becoming more positive.

The generated imaginary part of the dielectric function for Au at two temperatures are shown in Figure 3.18, together with E. Palik's and Pells & Shiga's data. $\epsilon^{num}(T)$ compares favorably to the published data from Pells & Shiga, although some notable differences arise. The numerical model is unable as yet to account for fine detail in the dielectric function, consequences of specific transitions between energy bands, as can be seen in Figure 3.18. The fine details are smeared out as a result of taking a single value of γ_b in equation (3.2.2). More realistic data would result if specific transitions and lifetimes were considered, although this would greatly increase the complexity of the numerical model and the fitting procedure. The model cannot faithfully represent the dielectric function for the low-wavelength/high-energy regime, $\lambda \lesssim$ 450nm for this reason, although the general trend is reproduced. For the visible and red parts of the spectrum, relying more on the free electron contribution, the numerical results compare well.

Rashidi-Huyeh *et al.* [57] recently conducted an analysis of Pells & Shiga's data and obtained the thermooptic coefficients, dn/dT and dk/dT, of Au. Using data supplied by $\epsilon^{num}(T)$, curves of the thermooptic coefficients of Au were produced over the range 295K-395K in order for comparisons to be made. Figure 3.19 shows the thermooptic coefficients of Au as determined by Rashidi-Huyeh and from the numerical model. Figure 3.19(a) shows fair agreement between two curves with similar features and magnitudes being reproduced. The main peak in the dn/dT spectrum is at 537.8nm from Rashidi-Huyeh and at 497nm from the $\epsilon^{num}(T)$ generated values. In the UV-blue region of the spectrum, Rashidi-Huyeh shows a peak located at 369nm, whereas the $\epsilon^{num}(T)$ model does not exhibit a similar feature due to the oscillations caused by the numerical evaluation method. Toward the red-NIR region, both curves show dn/dT increasing with wavelength over the specified range, but the modeled coefficients have a larger slope. Figure 3.19(b) again shows similar features between Rashidi-Huyeh's data and the numerical model, with the main peak being located at 477.2nm from Rashidi-Huyeh and 466.0nm from the numerical model. Again, detail for the low-wavelength region is lacking in the numerical model. The major differences arise

Table 3.2: Initial values, plus sweep ranges, for parameters in the numerical evaluation of $\epsilon^{num}(T)$.

Parameter	Initial Value	-50%	+50%
ω_p	6.88×10^{15} rad/s	3.44×10^{15}	10.32×10^{15}
γ_f	2.10×10^{15} rad/s	1.05×10^{15}	3.15×10^{15}
γ_b	2.40×10^{15} rad/s	1.2×10^{15}	3.6×10^{15}
ω_g	3.0×10^{15} rad/s	1.5×10^{15}	4.5×10^{15}
E_F	2.5 eV	1.25	3.75
UL	1.40×10^{16} rad/s	0.7×10^{16}	2.1×10^{16}

Table 3.3: Parameters and thermal coefficients used to generate values of the temperature dependent dielectric function, $\epsilon^{num}(T)$.

Parameter	Value (T=295K)	Thermal Coefficient	Value
ω_p	12.3×10^{15} rad/s	Θ_m	1.613×10^{-4} /K
γ_f	1.31×10^{14} rad/s	β	4.32×10^{-5} /K
γ_b	2.60×10^{16} rad/s	κ_f	1.047×10^{12} rad/sK
$\hbar\omega_g$	2.53 eV	κ_b	5.42×10^{9} rad/sK
E_F	2.5 eV	ξ	-1.7×10^{-4} eV/K
K	2.8×10^{24}		

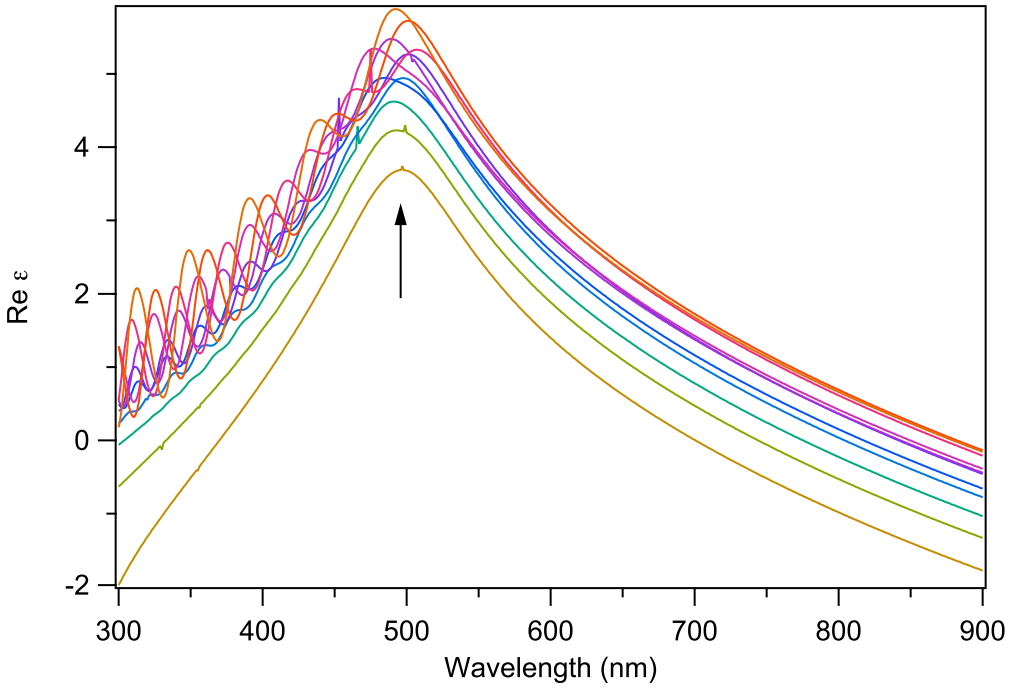

(a) Real part

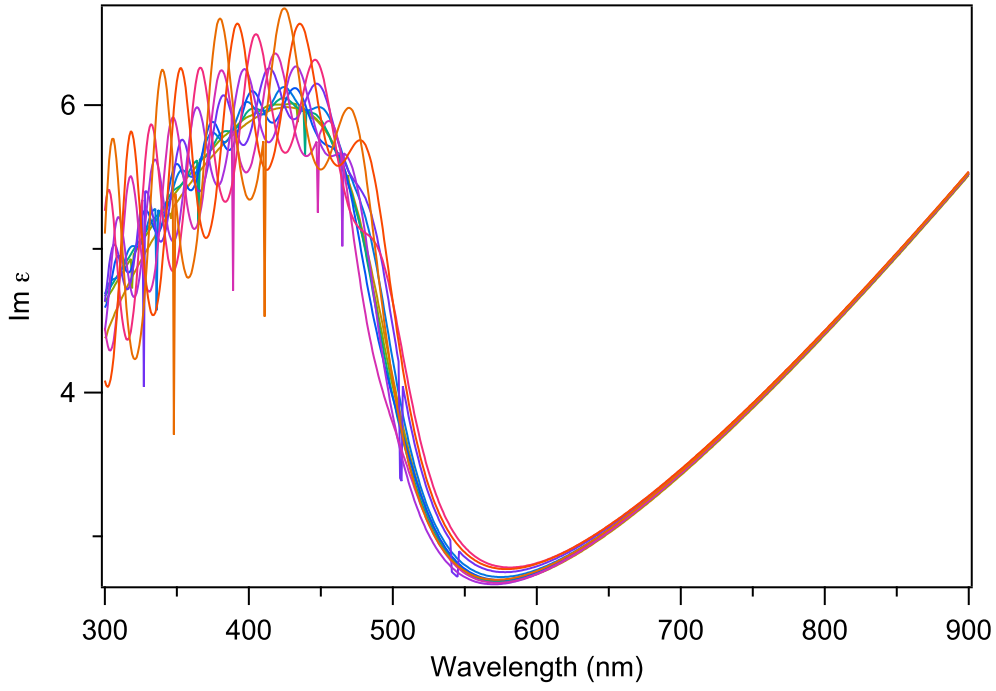

(b) Imaginary part

Figure 3.16: Integral upper limit (UL) sweep over the range UL = $0.7 \rightarrow 2.1 \times 10^{16}$ rad/s. The arrow indicates increasing UL.

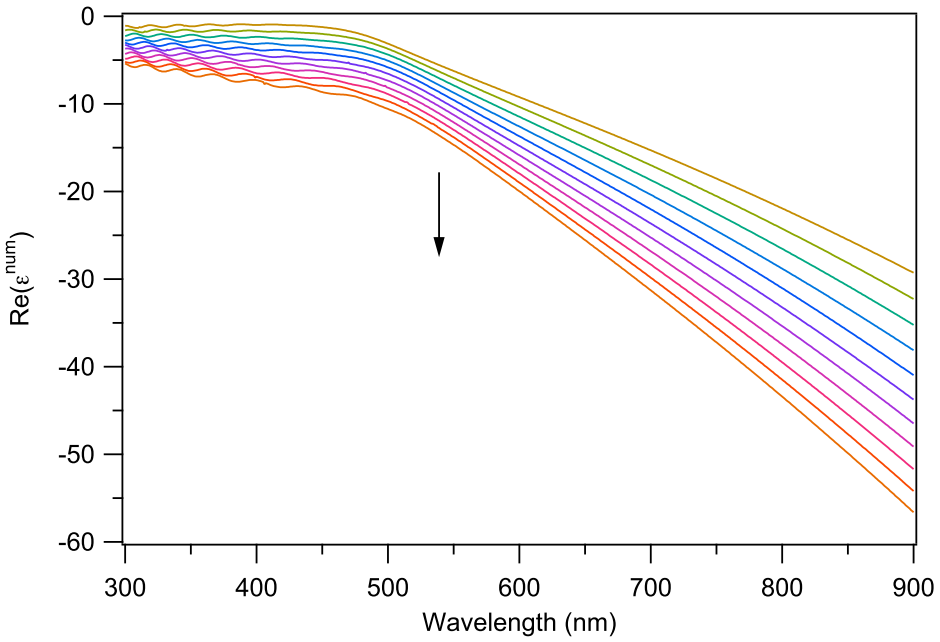

(a) The real part of $\epsilon^{num}(T)$.

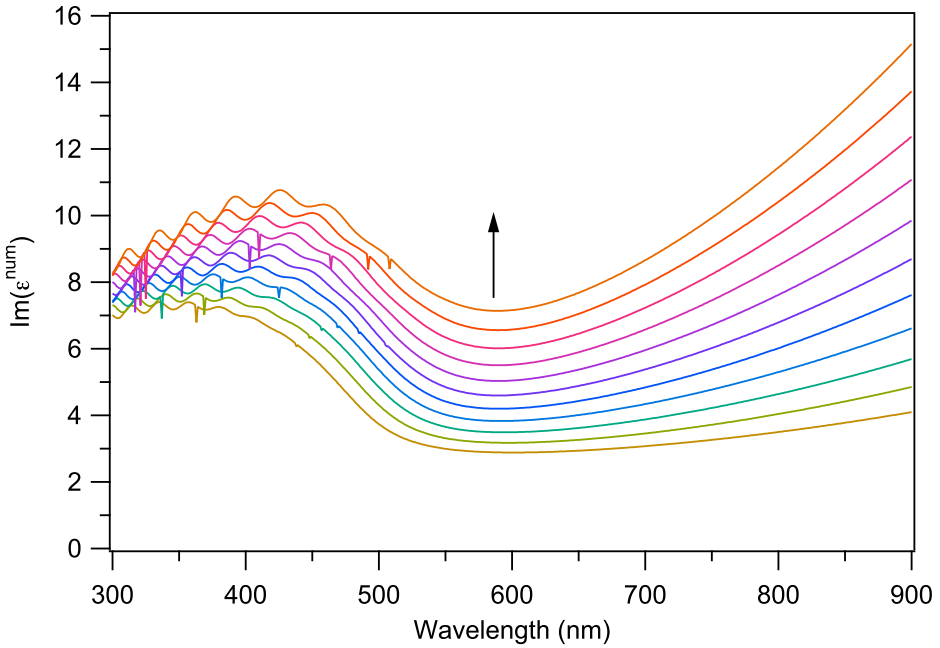

(b) The imaginary part of $\epsilon^{num}(T)$.

Figure 3.17: The numerically generated values of the dielectric function $\epsilon^{num}(T)$ for temperatures T = 295K-1295K. The arrow represents the direction of increasing temperature.

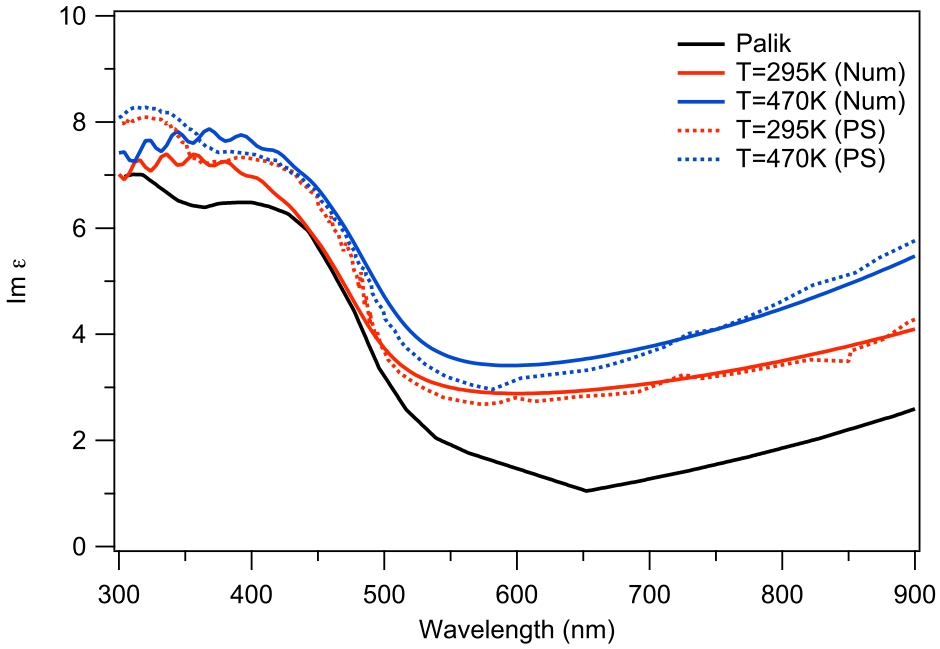

Figure 3.18: Imaginary part of dielectric functions. Shown is data from Palik, Pells & Shiga, and the numerical output of the dielectric function of Au at two temperatures.

from the signs and the red-IR behavior of dk/dT. Rashidi-Huyeh consistently shows that dk/dT is negative over the wavelength range of interest with a flattening curve towards the red-IR range. The numerical model supplies positive dk/dT values, with the curve increasing in the red-IR range.

3.4.3 Application to Oblate Spheroids

The dielectric functions $\epsilon^{num}(T)$, in conjunction with the results from Section 3.1.3, can now be used to investigate the temperature dependence of the polarizability and total cross-section of an oblate spheroid. Figure 3.20 shows α_x vs. wavelength at four different temperatures. The consequences of expansion on the optical properties, presented earlier in this Chapter, have a very small effect on the polarizabilities, regardless of expansion isotropy, over the revelent wavelength and temperature ranges. Nevertheless, the curves shown in Figures 3.20 - 3.23 assume anisotropic expansion along the major axis.

As the temperature of the spheroid is increased, the peaks in the polarizability (Figure 3.20) and cross-section (Figure 3.21) are lowered in magnitude and are shifted toward the blue. This is primarily due to the changes in $\epsilon^{num}(T)$ over the temperature range and can be explained in terms of the resonance condition ϵ_{1m}. Figure 3.17(a) shows as the temperature is increased, the real part of $\epsilon^{num}(T)$ decreases. The value of $\epsilon^{num}(T)$ satisfying the resonance condition for ϵ_{11} now occurs at a shorter wavelength, thus, the polarizability experiences a blue-shift. The decreasing magnitude and increasing width of the polarizability peaks is due to the imaginary part of $\epsilon^{num}(T)$ increasing with increasing temperature.

Any changes in the optical response of oblate spheroidal nanoparticles with changing temperature is due primarily due to modifications of the dielectric function of Au and only very weakly on the effects of thermal expansion on the nanoparticle itself.

Figures 3.22 shows the ratio of cross-sections $\sigma^p_{abs}/\sigma^p_{scat}$ at four different temperatures using the ϵ^{num}. The magnitude of $\sigma^p_{abs}/\sigma^p_{scat}$ decreases with increasing temperature, due to σ^p_{scat} increasing faster than σ^p_{abs}, shown in Figure 3.23. This gives an overall increase in total cross-section σ^p_{tot} with increasing temperature as seen in Figure 3.21.

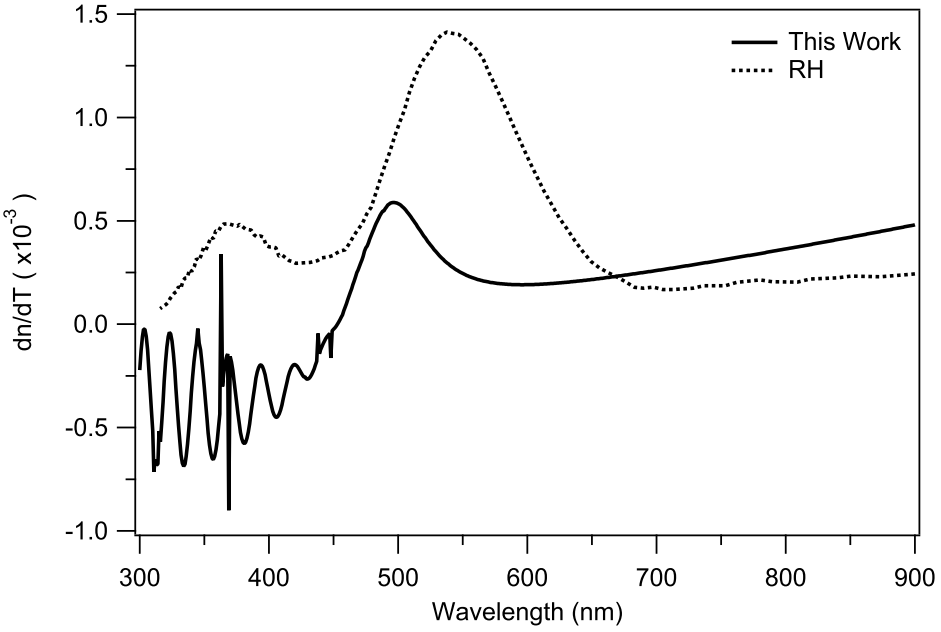

(a) dn/dT

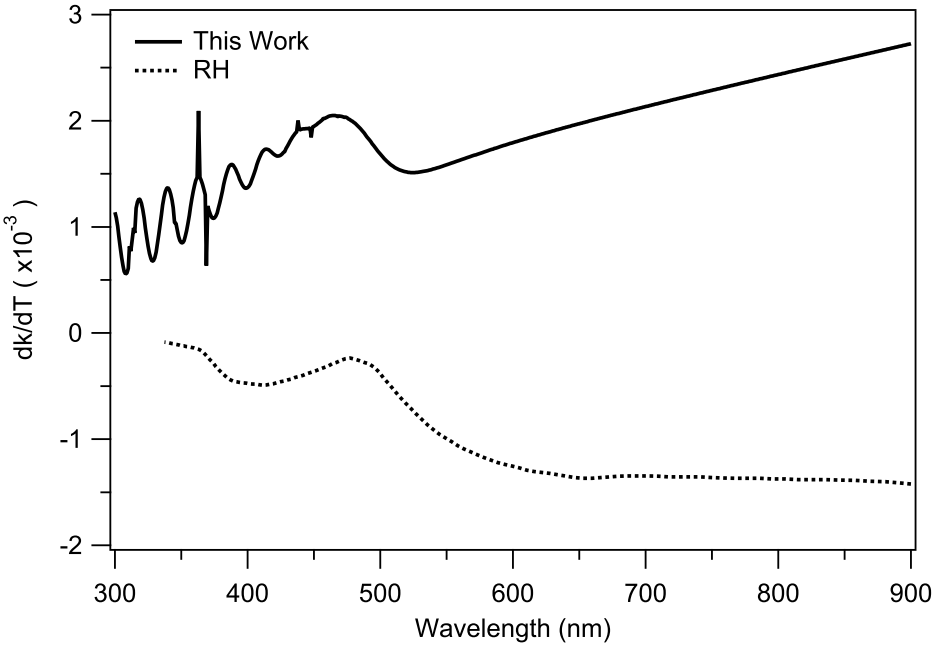

(b) dk/dT

Figure 3.19: The thermooptic coefficients dn/dT and dk/dT for Au for Au from Rashidi-Huyeh *et al.* (RH) and by the numerical model used in this work.

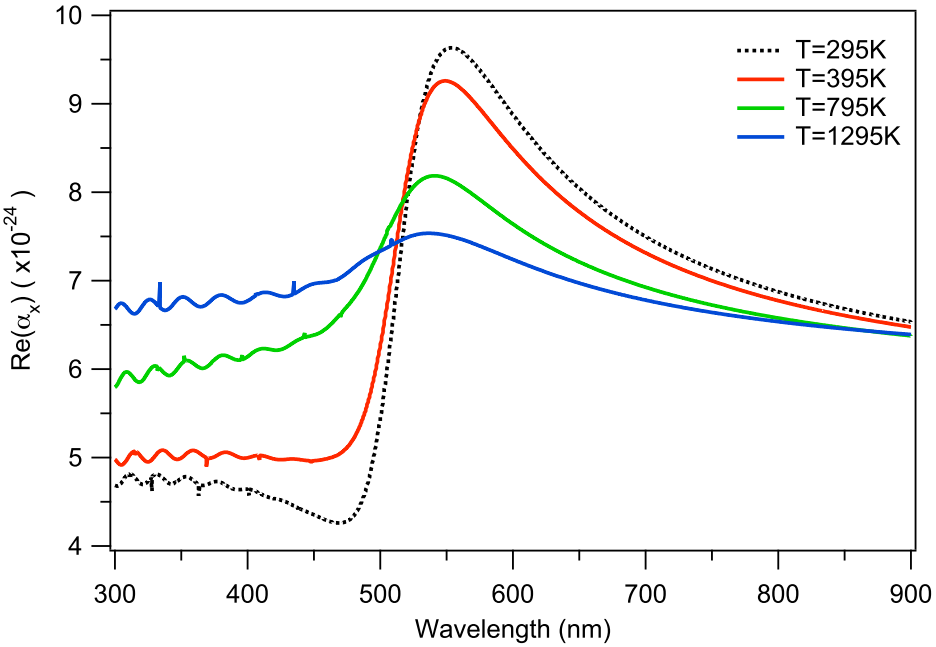

(a) The real part of α_x as a function of temperature.

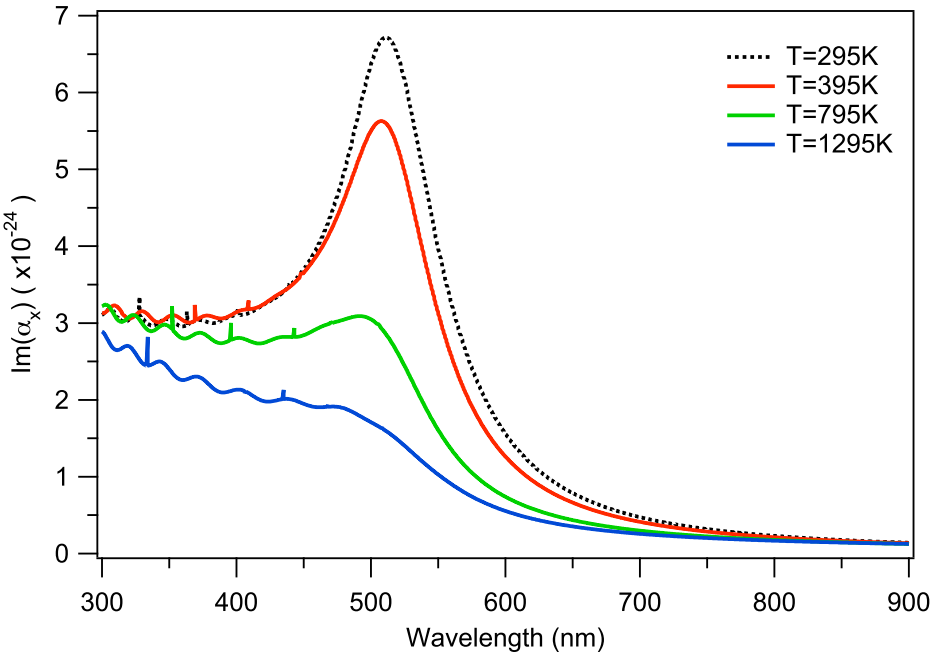

(b) The imaginary part of α_x as a function of temperature.

Figure 3.20: The real and imaginary parts of the polarizability along the major axis, α_x, as a function of wavelength for an oblate spheroid dimensions $z_0 = 10$nm, $r_0 = 20$nm, $R_0 = 0.5$ at four different temperatures assuming anisotropic expansion. The numerically generated dielectric functions $\epsilon^{num}(T)$ are used.

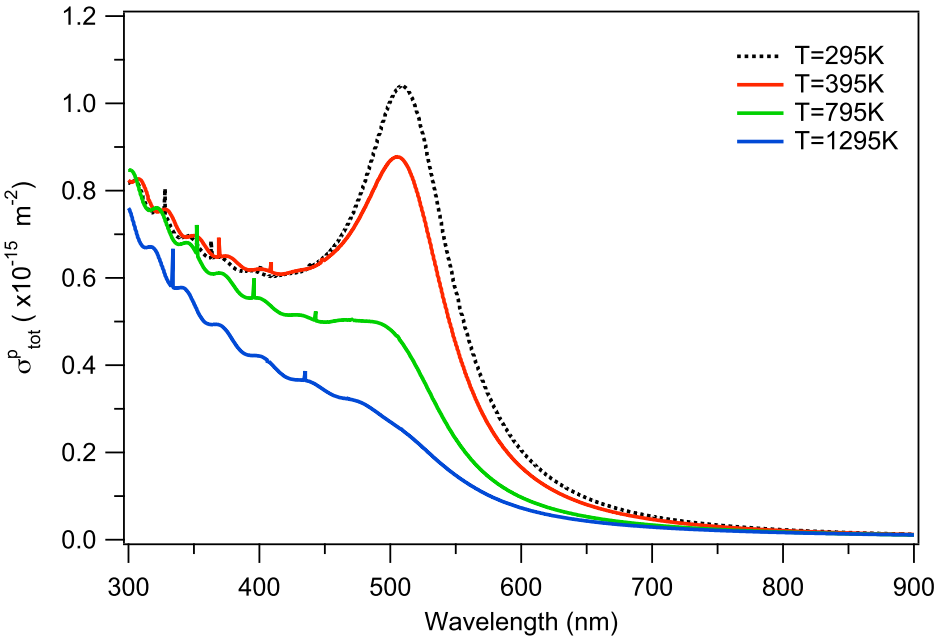

Figure 3.21: The total p-polarized cross-section, σ^p_{tot}, as a function of wavelength for an oblate spheroid dimensions $z_0 = 10$nm, $r_0 = 20$nm, $R_0 = 0.5$ at four different temperatures in the anisotropic case. The numerically generated dielectric functions $\epsilon^{num}(T)$ are used.

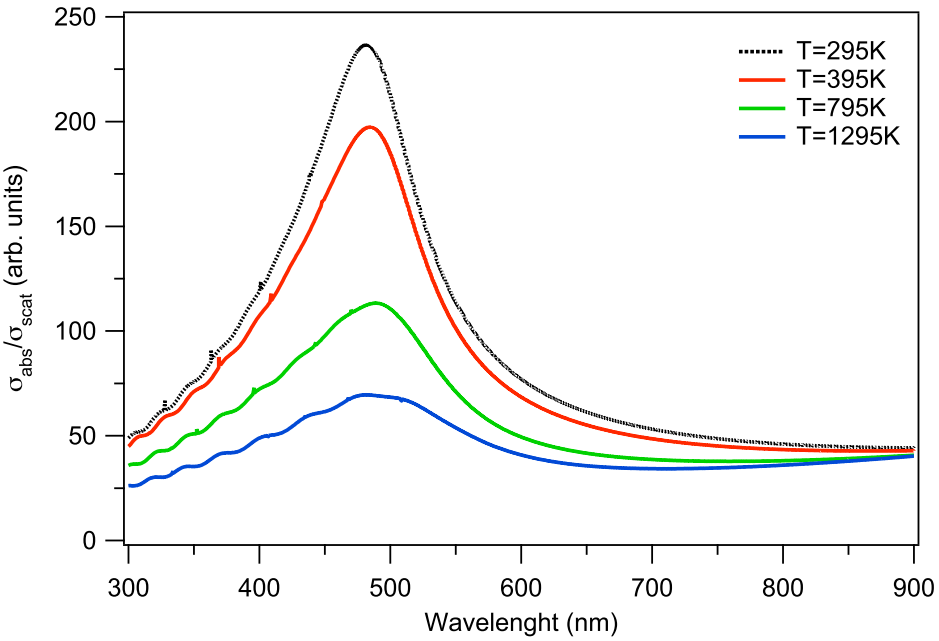

Figure 3.22: $\sigma^p_{abs}/\sigma^p_{scat}$ as a function of wavelength for an oblate spheroid dimensions $z_0 = 10$nm, $r_0 = 20$nm, $R_0 = 0.5$ at four different temperatures assuming anisotropic expansion. The numerically generated dielectric functions $\epsilon^{num}(T)$ are used.

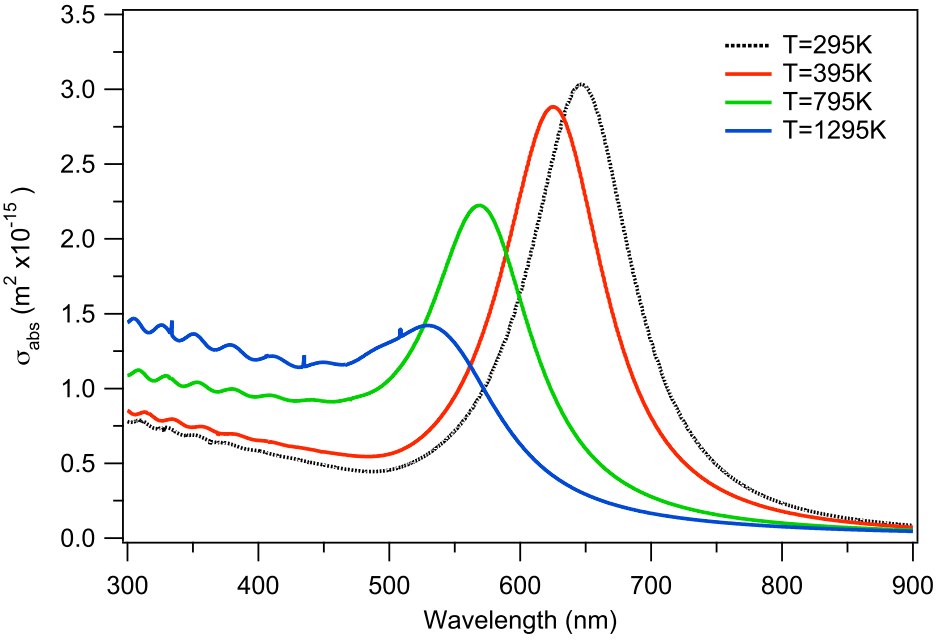

(a) σ_{abs}

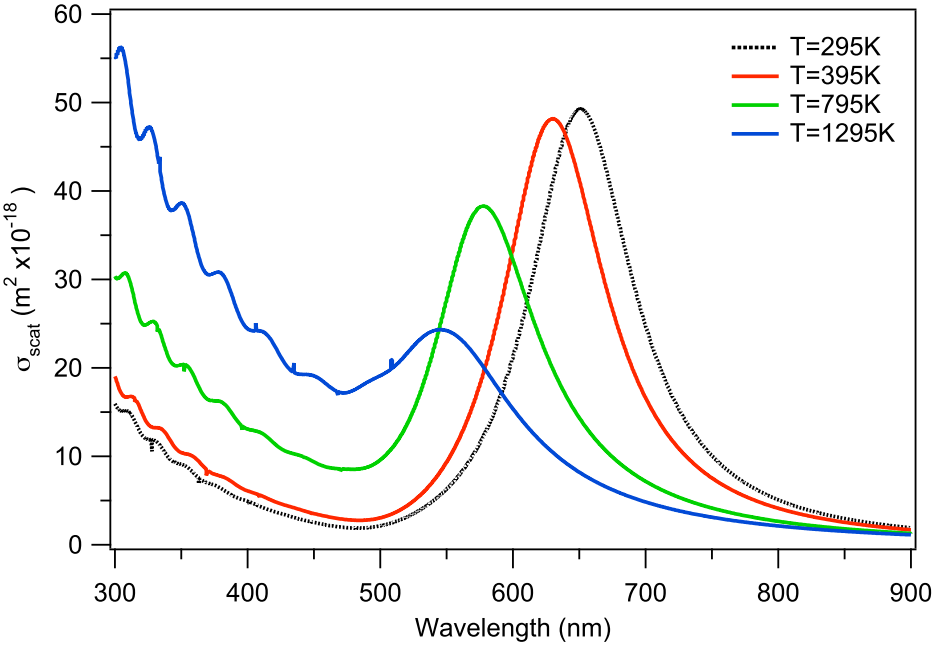

(b) σ_{scat}

Figure 3.23: The absorption and scattering cross-sections as a function of wavelength for an oblate spheroid dimensions $z_0 = 10$nm, $r_0 = 20$nm, $R_0 = 0.5$ at four different temperatures assuming anisotropic expansion. The numerically generated dielectric functions $\epsilon^{num}(T)$ are used.

Chapter 4

Thermal Dynamics

The previous chapter showed how the optical properties of oblate spheroids change with temperature. In order to fully appreciate the problem at hand, it is necessary to examine the thermal dynamics of a functioning plasmonic thermooptical device. The temperature $T(\mathbf{r}, t)$, a function of position and time, is sought for all space in the immediate vicinity of a hot nanoparticle supported on an insulating substrate in an ambient air environment. The governing heat equation to be solved is the heat equation [69]

$$\nabla^2 T(\mathbf{r}, t) + \frac{g(\mathbf{r}, t)}{k} = \frac{1}{D}\frac{\partial T(\mathbf{r}, t)}{\partial t} \tag{4.0.1}$$

where $g(\mathbf{r}, t)$ is a source term, k is the thermal conductivity and $D = k/\rho C_p$ is the thermal diffusivity of the material in question. If there is no heat generation within the medium, $g = 0$, and the Fourier equation is obtained

$$\nabla^2 T(\mathbf{r}, t) = \frac{1}{D}\frac{\partial T(\mathbf{r}, t)}{\partial t}. \tag{4.0.2}$$

For a steady-state solution, equation (4.0.2) simplifies to the Laplace equation,

$$\nabla^2 T(\mathbf{r}, t) = 0. \tag{4.0.3}$$

These heat equations must be solved, with appropriate boundary conditions, for the entire nanoparticle-BK7-air system. In this Chapter, the equations (4.0.1)-(4.0.3) are solved numerically using the finite-element approach of FEMLab [70].

To begin, thermal dynamics on the nanoscale and for short-time scales are introduced. Next, simple models are created and the solutions for the heat equations (4.0.1)-(4.0.3) are obtained in order to determine the feasibility of using FEMLab. These results are compared with the macroscopic theory of a sphere cooling in an infinite medium [71] and to experimental results obtained from pulsed-laser heating of Au nanoparticles suspended in water [40].

Models of nanoparticle-BK7-air systems are then created with oblate spheroids of various axis ratio R to investigate the thermal dynamics of each. The temperatures of the nanoparticle, air and substrate are obtained as a function of time during the heating and cooling phases in order to gain insight of the thermal dynamics of the system, possible constraints affecting device performance and methods to optimize device operation.

4.1 Nanoscale & Short Time Effects

As the primary consideration of this Chapter is focused on the thermal dynamics of nanoscale particles, nanoscale length and short-time scales must be taken into account. The heat equations (4.0.1)-(4.0.3) are macroscopic in nature and like other macroscopic-based theories, break down on the nanoscale [37] [72]. In general, heat conduction results from collisions between electrons and phonons and such collisions are often described in terms of the 'mean-free path', i.e., the average distance travelled between two successive collisions. Macroscopic models assume that the physical domain of interest is large enough to allow many collisions before a measurement is taken. The mean-free path of electrons in metals is on the order of nanometers at room temperature, so the macroscopic model breaks down for very small ($\lesssim$ 1nm) particles, as the assumption of many collisions on the order of a mean-free path is rendered invalid.

In a similar fashion, the 'mean-free time', also called the relaxation time, defined as the average time between two successive collisions, is assumed to be so small in the macroscopic models that many collisions take place in the physical domain before a measurement is taken. These time scales are roughly on the order of picoseconds for electons in metals, increasing to nanoseconds for phonons in insulators. As a general rule of thumb, time scales on the order of a nanosecond or less should receive special attention. Therefore, dealing with fast-transient processes using macroscopic models is also invalid. Problems involving heat conduction on the nanoscale and/or over short time scales must be examined carefully before applying macroscale models. This shall now be done for Au nanoparticles using the thermal de Broglie relation and the relaxation time.

An electron in a non-interacting electron gas at temperature T will have energy

$$E = \frac{3}{2} k_B T, \tag{4.1.1}$$

where k_B is the Boltzmann constant. The de Broglie relation is given as

$$\lambda = \frac{h}{p} \tag{4.1.2}$$

where h is Planck's constant and $p = \sqrt{2mE}$ is the momentum. Substituting equation (4.1.1) into equation (4.1.2) results in an expression for the thermal de Broglie wavelength

$$\lambda_T = \frac{h}{\sqrt{3mk_BT}}. \tag{4.1.3}$$

For electrons at $T = 300$K, λ_T is on the order of $\sim$ 5nm. If the particle size is less than λ_T, wave effects become important and heat conduction is no longer described accurately by the classical diffusion model. The mean-free path length and the thermal de Broglie wavelength are not synonymous but are often the same order of magnitude.

For time scales on the order of picoseconds after excitation, using a single term to describe the temperature of the particle is unrealistic. During excitation, the electron gas is heated rapidly and subsequent collisions with the lattice in the first few picoseconds lead to equilibrium between the electron temperature T_e and the lattice temperature T_l. The sink term $G(T_e - T_l)$ due to non-equilibrium electron-phonon interactions must be included

on the right-hand side of equation (4.0.1) if solutions are sought in the picosecond regime immediately after excitation.

The relaxation time for a sphere of radius r is given as

$$\tau = \frac{r^2}{D} \tag{4.1.4}$$

Considering a Au particle of radius 10nm, $\tau \sim 10$ ps. As one is interested in the time evolution of temperature on the order of nanoseconds (corresponding to a frequency of 1MHz) it can be assumed that $T_e \approx T_l = T$, i.e. the electron and lattice temperatures are equal and no differentiation is needed between the two. It should be noted however that in experiments seeking to increase the modulation frequency above 10MHz, full investigation into the role of electron-lattice thermalization should be considered.

The heat equations (4.0.1)-(4.0.3) can be simplified on the nanoscale by removing any spatial dependence in T. The Biot number Bi is a dimensionless variable defined as

$$Bi = \frac{h_T L_c}{k} \tag{4.1.5}$$

where h_T is the heat transfer coefficient, L_c the characteristic length, equal to the volume to surface area ratio. The Biot number can be used to establish a criteria under which the temperature distribution in an object can be considered uniform. If $Bi \ll 0.1$, one can assume that no temperature gradient exists inside the object so $T(\mathbf{r}, t) \approx T(t)$. For example, consider a spherical gold particle of radius 10nm. Typically, $5 \leq h_T \leq 25$ W/m^{2}K depending on the environment and $k = 317$ Wm^{-1}K^{-1} for Au. $Bi \approx 1 \times 10^{-9} \ll 0.1$, so on this length scale, the assumption of no temperature gradient in the particle is justified.

4.2 FEMLab

Numerical modeling is carried out in FEMLab. FEMLab is a highly customizable and very powerful finite-element analysis program that solves partial differential equations (PDEs) using a variety of algorithms for a number of physics and engineering problems. A brief outline to modeling in FEMLab follows.

First a structure is created in the built-in CAD drawing mode which mimics the physical geometries of the problem. Each structure is a subdomain, the material properties of which can be chosen from the built-in material library or input manually. The boundary conditions of the geometry are then defined. The choice of boundary conditions are extensive and may be customized at will. Creating the geometry, initializing the subdomain parameters and applying boundary conditions constitute the physics of the problem.

A mesh must be applied to the model geometry after the physics of the problem have been defined. A mesh is a partition of the geometric model into small elements of simple shape on whose vertices and edges PDEs are solved numerically. Having a larger number of elements increases accuracy and spatial resolution, especially when working with complex geometries, but greatly increases computational overhead. Finally, the numerical solving algorithms are applied to solve the problem. Solving algorithms include stationary linear and non-linear solvers, time-dependent linear solvers, eigenvalue and parametric solvers, which are completely customizable in their own right.

The heat conduction models that are included by default with FEMLab are the macroscopic models. Before using FEMLab to solve the problem of the nanoparticle-BK7-air system, feasibility studies are carried out by comparing FEMLab solutions to macroscopic theory and nanoscale experimental results.

4.2.1 Sphere Cooling in an Infinite Medium

Cooper [71] used the Laplace transform method to obtain analytic solutions for a sphere cooling in an infinite medium. The temperature of the sphere $T_s(t)$ for $t \gg \tau$ is given as

$$T_s(t) = T_{m,i} + \frac{(T_{s,i} - T_{m,i})}{6\sqrt{\pi}} \frac{k_s\sqrt{D_s}}{k_m\sqrt{D_m}} \left(\frac{\tau_s}{t}\right)^{3/2} \tag{4.2.1}$$

where k is the thermal conductivity, D the thermal diffusivity and the subscripts s, m and i refer to the sphere, the medium and the initial values respectively. Figure (4.1) shows the temperature of spheres of various radii, evaluated using equation (4.2.1) and solutions from FEMLab, during the first 1μs of the cooling phase. The initial sphere temperature $T_{s,i} = 500$K and the air $T_{m,i} = 295$K.

The FEMLab and analytic solutions appear to converge over a time scale $t > 1\mu$s. Shorter times ($t \leq 100$ns) show much different results. In particular, the analytic solutions result in a singularity as $t \to 0$ as t is present in the denominator in equation (4.2.1). The analytic solution is macroscopic in nature, so nanoscale effects are not taken into account. The surrounding medium is treated as being infinite, however this is not possible using FEMLab as the computation domain must be finite for obvious reasons.

4.2.2 Cooling of Au Nanoparticles in Water

The second method of comparison is with the experimental data of Hu *et al.* [40]. Briefly, Hu carried out ultrafast pump-probe spectroscopy on various size Au nanoparticles suspended in water and measured the bleach intensity as a function of time following 120ps pulse excitation. The magnitude of the bleach signal is proportional to the nanoparticle temperature [60].

A model mimicking Hu's physical geometry is created in FEMLab. Individual Au spheres, of the same radii as measured by Hu, are placed in water. The nanoparticle-water boundary condition is chosen to be continuous and the outer water boundary is chosen to be convective. Hu does not specifically mention the temperatures of the sphere and water. Instead, he estimates the temperature difference ΔT between the nanoparticles and water as a result of pulsed-laser heating using Beer's law. The FEMLab model is evaluated for $\Delta T = 80$K, with the initial sphere and water temperatures set to $T_s = 375$K and $T_w = 295$K respectively. The cooling phase is modeled during the initial 500ps for comparison to experimental data.

Figure (4.2) shows the temperature as a function of time for a sphere cooling in water. The solid lines correspond to the FEMLab solutions, the points are Hu's experimental bleach signal data normalized to temperature. Comparing the experimental data with FEMLab solutions show a good qualitative match on a short time scale. The experimental data shows initial ($t < 100$ps) cooling as being much quicker than the FEMLab model, which maybe due to electron-phonon thermalization on this timescale which FEMLab does not

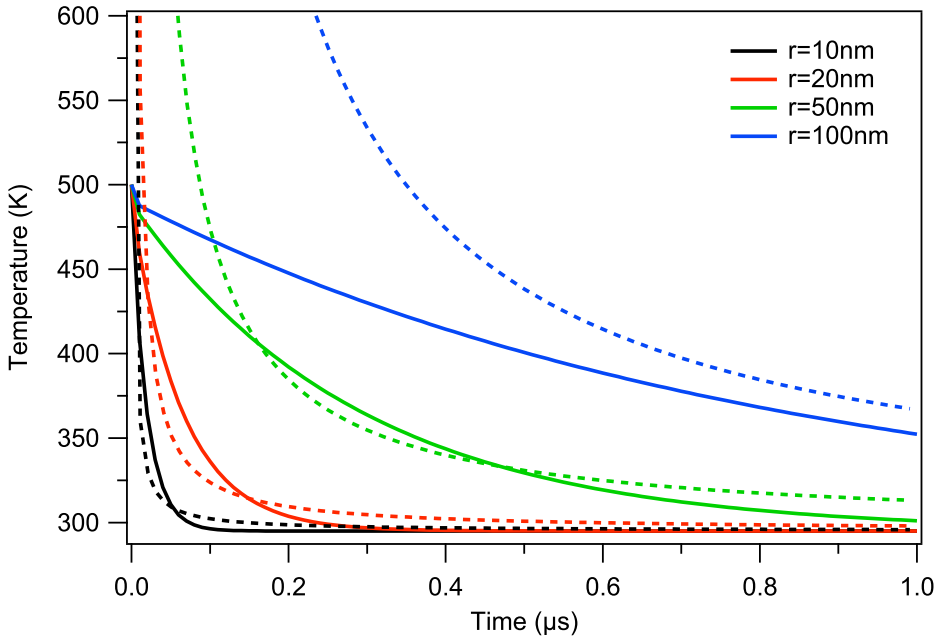

Figure 4.1: A comparison between cooling for Au spheres, initially at $T = 500$K, of various radii surrounded by air at $T = 295$K. Solid lines correspond to FEMLab numerical solutions, dashed lines are data from equation (4.2.1).

take into account. This may also be due to simplistic model created in FEMLab; in reality, many particles are suspended in water, not just one as the model assumes. At longer times ($t > 200$ps), the modeled temperatures converge with the experimental data as one would expect, as eventually the spheres and water will reach equilibrium.

4.2.3 Conclusions

Both comparisons with Cooper and Hu show that smaller spheres cool quicker as a result of larger surface/volume ratio. FEMLab solves the macroscopic models of heat conductivity and convection in these simulations but the radiative mode is not included. FEMLab gives realistic and reliable qualitative results for times $t > 200$ps, given simplistic assumptions, when compared with the macroscopic analytical solution of Cooper and with the experimental nanoscale cooling of Hu. More detailed study is certainly merited but lies outside the scope of this work.

4.3 Oblate Spheroids on a BK7 Substrate

The physical model for heat transfer studies is described as follows. A single Au nanoparticle is supported on the surface of an insulating BK7 substrate surrounded by air. There is no truncation of the nanoparticle due to the substrate surface, i.e., the particle is perfectly spheroidal during heating and cooling. The nanoparticle is assumed to be in good thermal contact with the substrate and the surrounding air.

Three distinct subdomains are defined within the computational domain; the Au nanoparticle, the substrate and the surrounding air. Next, the material properties of the subdomains are defined. The values for material properties such as density, heat capacity, thermal conductivity, together with heat source terms Q and initial temperatures are entered. Table 4.1 shows the relevant subdomain properties. Only the Au nanoparticle is absorbing, i.e. the heat source term originates from the absorption of light by the nanoparticle. Absorption by the air and the substrate is negligible and thus Q for these subdomains is set to zero.

A continuity boundary is selected for the nanoparticle and substrate surfaces. The outer BK7 surface is chosen to be at constant temperature $T = 295$K. BK7 has a low thermal conductivity and the substrate is thick compared to the nanoparticle so this choice of boundary condition is justified. The outer air boundary is chosen to be convective because air is a low density fluid and therefore very effective at convective cooling. The effects of radiative cooling are not included. Realistically, the nanoparticle is not completely isolated, but is in close proximity to others. A realistic model would naturally include as many nanoparticles as possible, but this vastly increases computational overhead. Including every nanoparticle is unrealistic even on the most powerful multiprocessor clusters. However, this problem may be alleviated by utilizing periodic boundary conditions in FEMLab. A smaller domain is created within the geometry which is roughly the size of the nanoparticle-nanoparticle spacing and boundary conditions specifying equal flux are applied. Figure (4.3) illustrates the FEMLab geometry.

Due to the simplicity of the model geometry, a fine meshing procedure is applied. A time-dependent linear solver using the UMFPACK [73] code is used. The options governing the operation of the UMFPACK code are numerous; the default options within FEMLab are chosen.

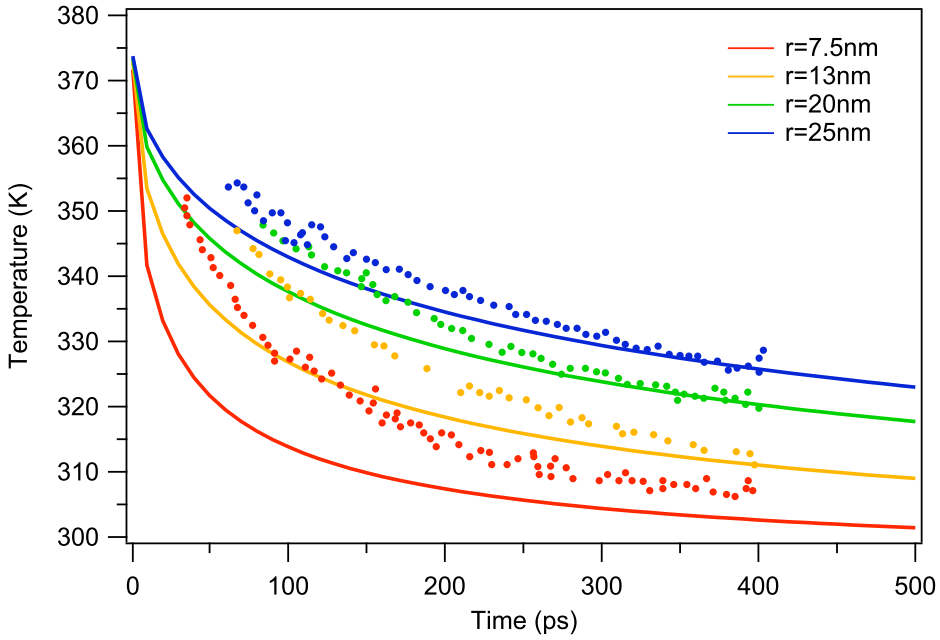

Figure 4.2: The temperature of Au spheres of various radii cooling in water following pulsed laser excitation. The initial sphere and water temperatures are T_s = 375K and T_w = 295K respectively. Solid lines lines correspond to FEMLab numerical solutions, points are experimental data from Hu.

Table 4.1: Material properties input into FEMLab

	Air	Water	BK7	Au
Thermal Conductivity, k (W/mK)	0.0257	0.611	1.114	317
Density, ρ (kg/m^3)	1.205	1000	2510	19300
Heat Capacity, c (Ws/kgK)	1005	4180	858	129
Heat Source, Q (W/m^3)	0	0	0	$\tilde{Q}_{NP}$

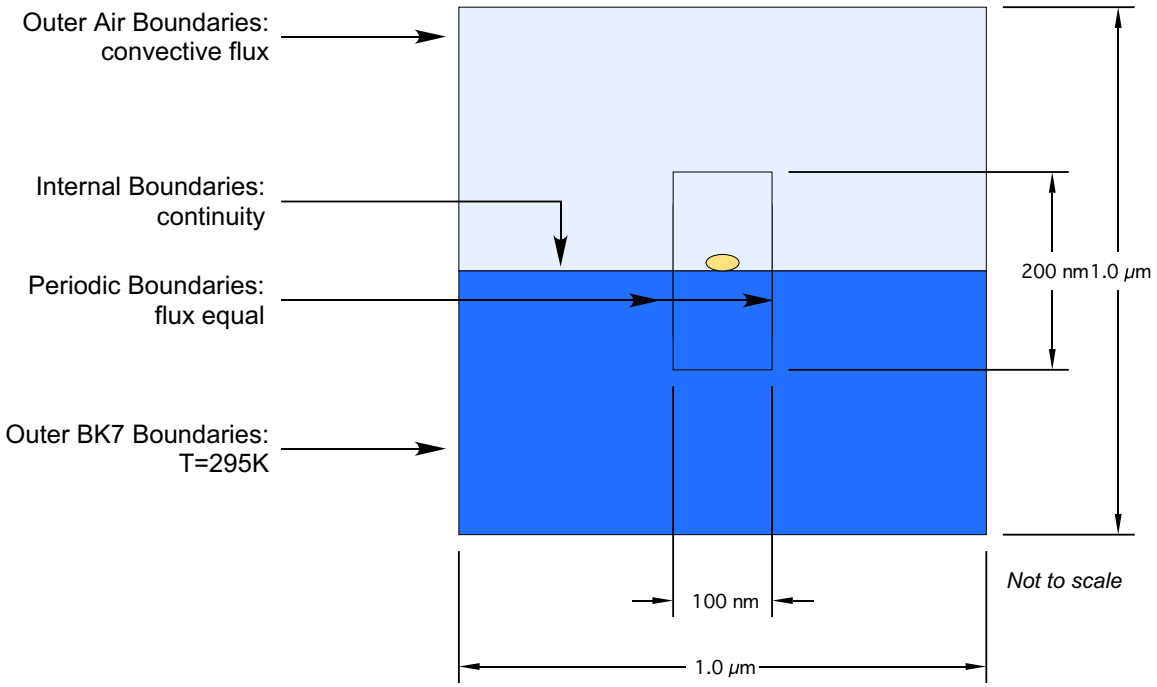

Figure 4.3: A schematic of the FEMLab geometry showing outer and internal boundaries and applied boundary conditions.

4.3.1 Heating

Heat generated within the nanoparticle is due only from the absorption of light and no heat is generated within the BK7 substrate or air. Since the nanoparticles are small and thus the Biot condition satisfied, one can regard the temperature distribution inside the nanoparticle as being uniform. As the particle temperature increases from the initial temperature, a thermal gradient is established between the particle and the surroundings leading to outward heat flux from the particle which locally heats the air and substrate.

FEMLab allows input of volume heat source, so an expression relating the effective heat source term per nanoparticle, $\tilde{Q}_{NP}$ is derived as follows. A continuous-wave (CW) pump laser beam at wavelength λ and of power P_0 is normally incident on the nanoparticle sample. The power absorbed, P_{abs}, by the nanoparticles in the beam area is

$$P_{abs} = P_0(1 - R^0 - 10^{-Abs}) \tag{4.3.1}$$

where Abs is the experimentally measured absorbance at the pump wavelength and R^0 is the reflectivity of the substrate, typically around 4%. The power absorbed per nanoparticle is therefore

$$P_{abs,NP} = \frac{P_{abs}}{AN} \tag{4.3.2}$$

where A is the pump beam spot area and N is the number density of nanoparticles on the surface. The volume heat source term, defined as the heating power per unit volume, is

$$\tilde{Q}_{NP} = \frac{P_{abs,NP}}{\tilde{V}} \tag{4.3.3}$$

$$= \frac{P_0(1 - R^0 - 10^{-Abs})}{AN\tilde{V}} \tag{4.3.4}$$

where $\tilde{V} = \frac{4}{3}\pi r^2 z$ is the average oblate spheroid nanoparticle volume.

$\tilde{Q}_{NP}$ is therefore a function of the pump power and is input into FEMLab. Assuming typical values of $P_0 = 1$W, $Abs = 0.2$, $A = 8000\mu\text{m}^2$, $N = 1 \times 10^{14}\text{m}^{-2}$, $R^0 = 0.04$ and $V = 4000\text{nm}^3$, $\tilde{Q}_{NP} \approx 1 \times 10^{17}\text{W/m}^3$.

Figure (4.4) shows the typical graphical output of FEMLab for a heated nanoparticle on BK7 substrate.

4.3.2 Cooling

When the pump beam is turned off, the heat generation source term is removed and the particle cools by conduction to the substrate and air and convection to the air. Radiative cooling is so small as to be negligible as the emissivity of gold is extremely low. The cooling phase is modeled by setting $\tilde{Q}_{NP} = 0$ and the computation is run using the solution at the moment the heat source term is removed.

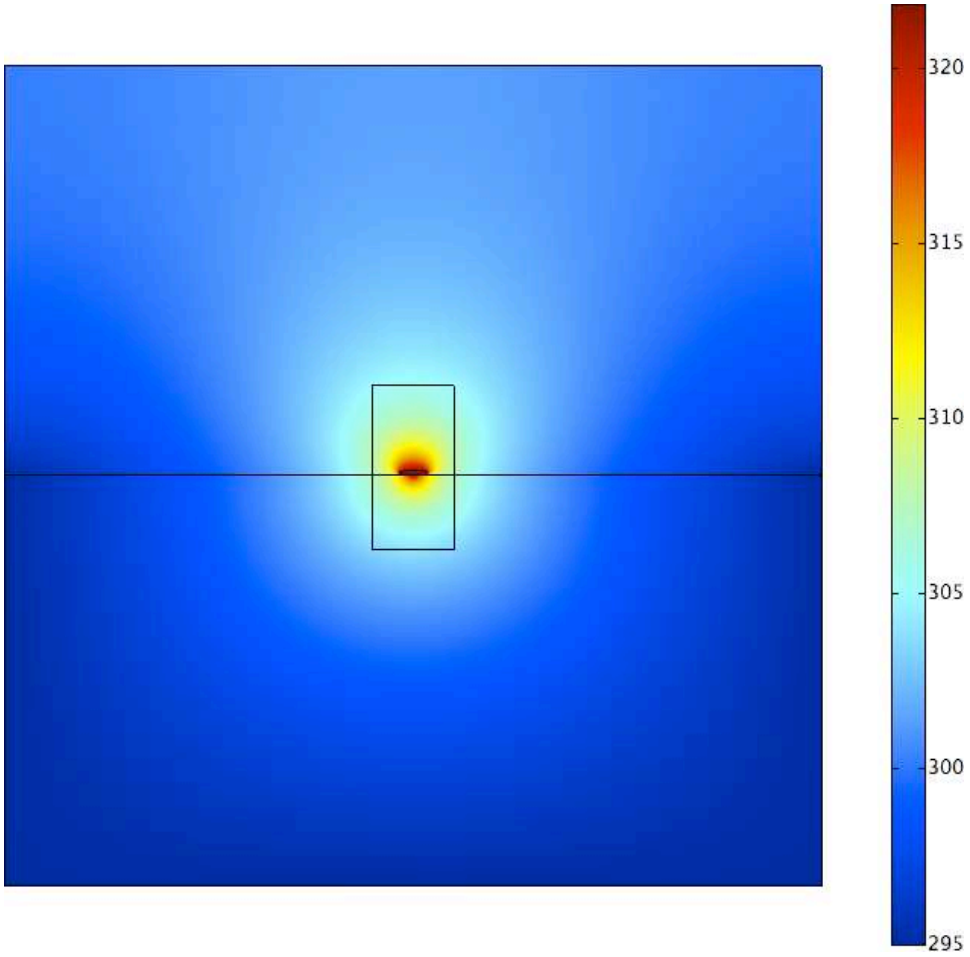

Figure 4.4: Typical FEMLab graphical output showing the hot oblate spheroid nanoparticle on a BK7 substrate. The temperature scale is in degrees Kelvin.

4.3.3 Results & Discussion

Figure (4.5) shows the temperature of oblate spheroidal nanoparticles of various axis ratio R and at a point in the BK7 substrate, 50nm below the nanoparticle, as a heat source term of $\tilde{Q}_{NP} \approx 1 \times 10^{17}\mathrm{W/m^3}$ is applied. The 50nm point beneath the particle was chosen arbitrarily. The more spheroidal nanoparticles (smaller R), heat slower and reach a lower temperature than the spherical nanoparticles ($R = 1.0$), possibly as a result of the increased surface and contact area of the spheroid to the substrate. Heating times for all particles are very quick, reaching 90% of the final temperature within the first 100ns. The point 50nm below the nanoparticle in the BK7 substrate also heats up rapidly, but not as fast as the nanoparticles, and does not reach the same temperature. Figure (4.6) shows the temperature difference $\Delta T = T_{NP} - T_{BK7}$ between the nanoparticle and the substrate, with the largest temperature difference occurring for the spherical nanoparticle, suggesting that the smaller contact area between nanoparticle and substrate results in a larger nanoparticle temperature.

Figure (4.7) shows the temperature of oblate spheroidal nanoparticles of various axis ratio R and a point in the BK7 substrate, 50nm below the nanoparticle, when the heat source term is removed. The model continues on from the heating phase, so the initial conditions are supplied at the time when the heat source is removed. The more spheroidal nanoparticles (smaller R), cool slower than the spherical nanoparticles ($R = 1.0$), possibly as a result of the increased contact area to the substrate. The substrate acts as an efficient insulator with most of the heat being transfered via convection with the air rather than via conduction with the substrate. The nanoparticle and substrate reach the ambient temperature of 295K within 400ns. Cooling times for all particles are very quick, reaching 90% of the final temperature within the first 100ns. The point 50nm below the nanoparticle in the BK7 substrate also cools down rapidly, but not as fast as the nanoparticles. Figure (4.8) shows the temperature difference $\Delta T = T_{NP} - T_{BK7}$ between the nanoparticle and the substrate, with the largest temperature difference occurring for the spherical nanoparticle, suggesting that the a smaller contact area between nanoparticle and substrate results in a larger nanoparticle temperature.

The performance, in terms of modulation rate, of a thermooptic plasmonic device will be maximized when the nanoparticle can heat and cool quickly while preventing heat conduction to the substrate. The substrate has been shown to insulate the nanoparticle and nanoparticles with a larger contact area taking marginally longer to heat up and cool down. The contact area with the nanoparticle must be minimized to prevent heat conduction to the substrate, whereas the contact area with a fluid must be maximized. The radiative mode is not included, as the radiation losses from gold are negligible due to the small emissivity. There is strong evidence to suggest that heat transfer via the dipole-dipole interactions between nanoparticles is enhanced [74] [75]. The radiative thermal conductance between closely spaced nanoparticles is proportional to the radius to power six and inverse separation distance to power six. FEMLab does not yet include this nanoscale radiative mode.

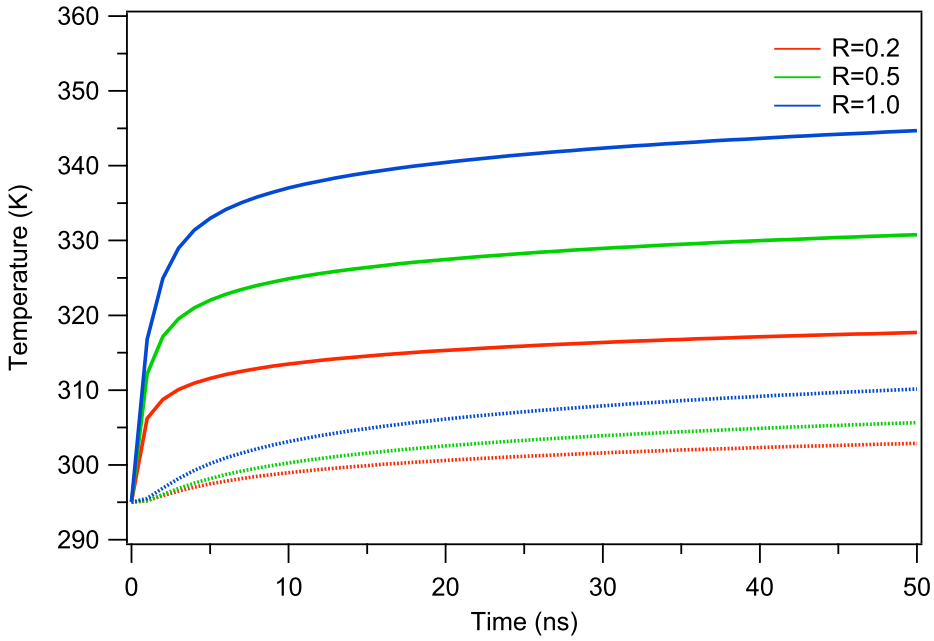

Figure 4.5: The temperature of oblate spheroids (solid lines) of various axis ratios R and the BK7 substrate (dashed lines) with the heat source $\tilde{Q}_{NP} = 1 \times 10^{17}\mathrm{W/m^3}$. Spheroids are of constant volume.

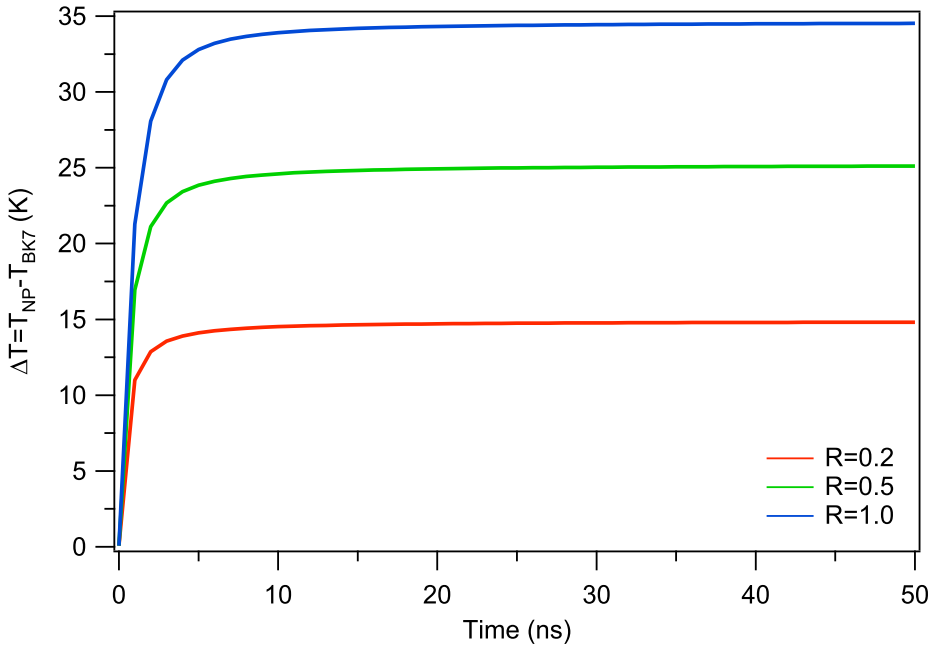

Figure 4.6: The temperature difference ΔT during the heating phase between the oblate spheroids nanoparticle and the BK7 substrate with the heat source $\tilde{Q}_{NP} = 1 \times 10^{17}\mathrm{W/m^3}$. Spheroids are of constant volume.

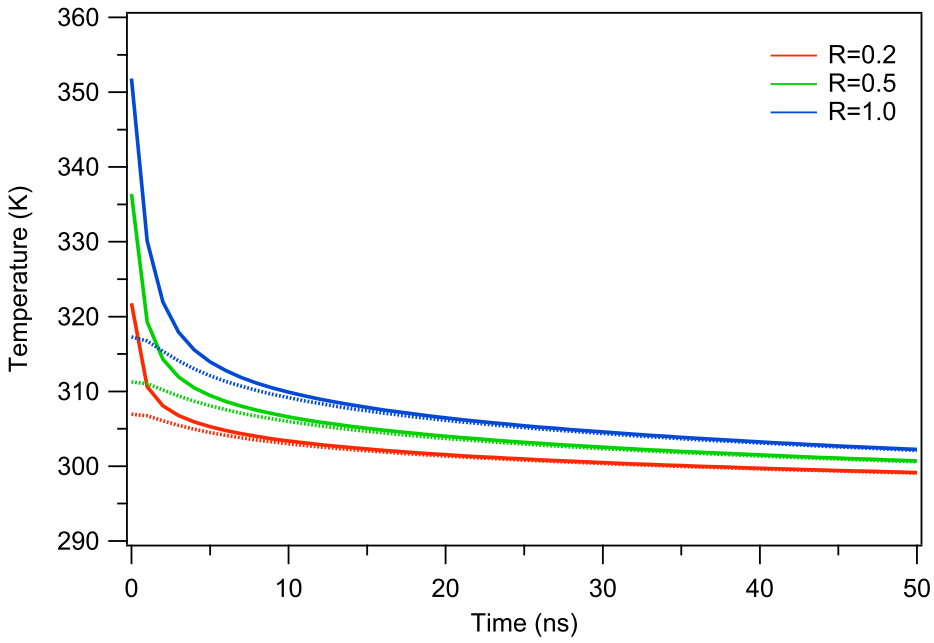

Figure 4.7: The temperature of oblate spheroids (solid lines) of various axis ratios R and the BK7 substrate (dashed lines) with the heat source term removed. Spheroids are of constant volume.

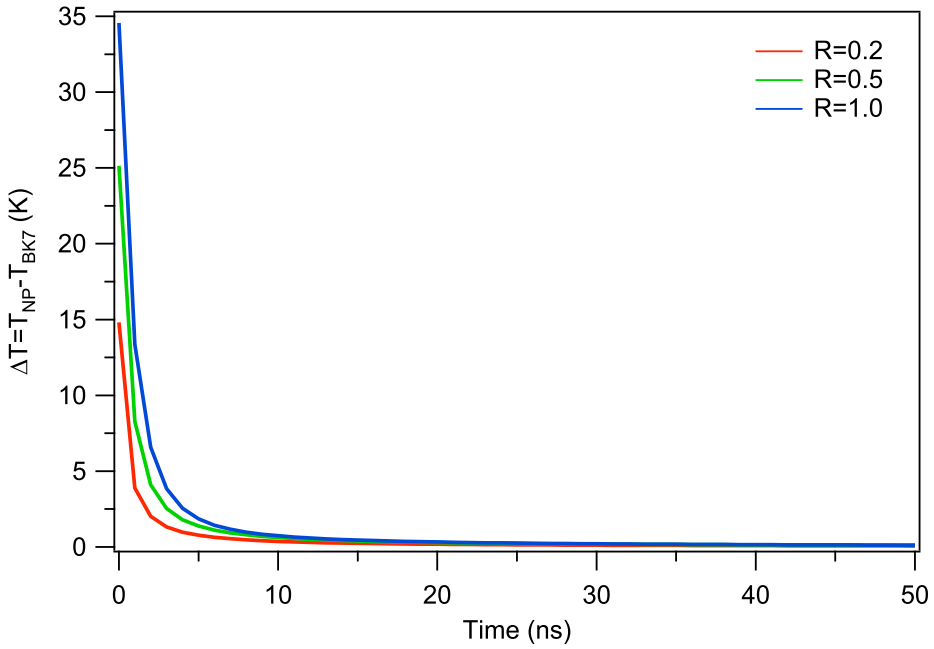

Figure 4.8: The temperature difference ΔT during the cooling phase between the oblate spheroids nanoparticle and the BK7 substrate with no heat source term. Spheroids are of constant volume.

Chapter 5

Sample Fabrication Methods

Chapter 2 introduced the theoretical framework describing SP excitation by light on spheroidal nanoparticles. In particular, the wavelength at which a peak in the absorbance spectrum occurs is related to the shape parameter η. In general, the more pronounced the shape, e.g., flattened discs for oblates and elongated needles for prolates, the absorbance peak is further red-shifted. Table 5.1 shows the values of ϵ_{11} and η for both spheroidal cases required to match the resonance condition at that particular wavelength.

To investigate thermal effects in Au nanoparticles, a suitable sample exhibiting strong absorption characteristics at the desired pump and probe wavelengths is required. Lereu used a high power CW fiber laser operating at $\lambda = 1.48\mu$m as the pump to provide the SP excitation mechanism. Three fabrication techniques were investigated in order to produce samples with strong absorption for a range of pump wavelengths. The experimental methods and applicable results of nanoparticle sample fabrication are presented in this Chapter. Simulations of the optical response, using parameters obtained from scanning probe microscopy, are also presented.

5.1 Glancing Angle Deposition

Nanostructured thin films with a range of morphologies may be manufactured over large areas by the glancing angle deposition (GLAD) method. Early experiments by Mbise [76] showed filaments of material tilted at a pronounced angle to the surface normal. Using this technique Robbie *et al.* fabricated porous thin films with densities as low as 15% of bulk [77]. By controlling the mechanical parameters of the deposition, such as dynamic control of substrate orientation, several complex sculptured thin films were reported with potential applications in optical and bio-chemical studies [78] [79]. Similarly, Hrudey *et al.* review how GLAD, which traditionally has been applied to inorganic material, may be used to create thin films of organic nanostructures [80].

During deposition, hot atoms evaporating from the source material will reach the cold substrate surface. Upon impact, they will undergo random motion on the substrate, eventually stopping at a defect site. Further material coalesces to this nucleation point and the film begins to grow from many similar isolated islands. When the substrate is tilted with respect to the direction of material flux, the surface-bound atoms, clusters and islands will shadow regions of the surface from incident material. As more material is deposited,

columnar structures begin to form and grow in a direction almost parallel to the direction of deposited material flux.

The tilt angle θ_β of the columnar structures is related to the deposition angle θ_α, illustrated in Figure 5.1, by an empirical relation known as the tangent rule

$$\tan\theta_\beta = \frac{2}{3}\tan\theta_\alpha. \tag{5.1.1}$$

Figure 5.2 shows an SEM image of 2μm of CaF_2 deposited at a rate of 20Å/s onto a clean Si substrate tilted at $\theta_\alpha = 60°\pm 2°$. The column tilt angles are measured to be $\theta_\beta = 50°\pm 5°$, showing good agreement with equation (5.1.1).

GLAD is investigated as a possible method of fabricating nanoparticles with controllable dimensions.

5.1.1 Experimental Method

It is well known that deposition of CaF_2 thin-films result in a roughened surface with root-mean-square (RMS) surface roughness proportional to the CaF_2 film thickness [81]. Therefore, CaF_2 is used to deliberately and controllably roughen the substrate surfaces. BK7 glass substrates were used for UV-Vis-NIR spectroscopic and atomic force microscopy (AFM) measurements and Si substrates were used for scanning electron microscopy (SEM) imaging. Each are processed identically. After a standard chemical cleaning process, various thicknesses of CaF_2 were deposited on the substrates at normal incidence ($\theta_\alpha = 0°$) via e-beam deposition. The CaF_2-coated substrates were then tilted within the evaporation chamber and various thicknesses of Au deposited at $\theta_\alpha = 85°$. Both films were deposited at a rate of ~ 5Å/sec as measured by a quartz film thickness monitor.

Spectroscopic measurements were carried out in a scanning UV-Vis-NIR spectrophotometer employing a reference beam line and identical polarizing filters on both the sample and reference beam lines. Reference samples, with identical CaF_2 films but no Au, were used in order to minimize any substrate and CaF_2 effects. Absorbance spectra were obtained for the p-polarization over a wavelength range 300nm-900nm. The optimum operating region for the polarizing filters is from 400nm to 1.2μm.

Scanning electron microscopy, using a Hitachi 4300 system, was performed on the Si-substrate samples in order to minimize sample charging effects. No conductive overcoat layer was deposited to prevent any unintended coalescence with existing Au nanoparticles. AFM imaging was performed with a Digital Instruments Multimode Nanoscope 3 in tapping mode using DNP-S10 triangular-shaped probe tips with force constant of 0.12N/m. The samples were imaged in air at ambient room temperature and pressure.

The number density N, nanoparticle dimensions r_0 and z_0 and the average nanoparticle-nanoparticle separation obtained from microscopy are input into two models for comparison with experimental absorbance spectra. The modified thin-film approximation (MTFA) formalism is relatively accurate for low coverage nanoparticle films of physical size $\ll \lambda$ supported on a dielectric substrate, but does not take into account multipole resonances or nanoparticle-nanoparticle interactions. The second model, GranFilm [82], is a comprehensive open-source package that enables multipole resonances, nanoparticle-nanoparticle interactions and truncation of island films on a substrate to be computed, but places restrictions on the orientation of the nanoparticles. The parameters input into GranFilm include

Table 5.1: The shape parameters η and minor-to-major axis ratios R for prolate and oblate spheroids required to exhibit strong absorption at a wavelength λ. N/A indicates that a resonance is not possible at this wavelength.

λ (nm)	ϵ_{11}	η_{obl}	R_{obl}	η_{pro}	R_{pro}
442	-1.183	N/A	N/A	N/A	N/A
514.5	-3.986	0.416	0.384	1.221	0.573
632.8	-9.520	0.145	0.143	1.048	0.299
830.8	-29.413	0.044	0.044	1.01	0.140
1480	-87.884	0.015	0.015	1.003	0.077

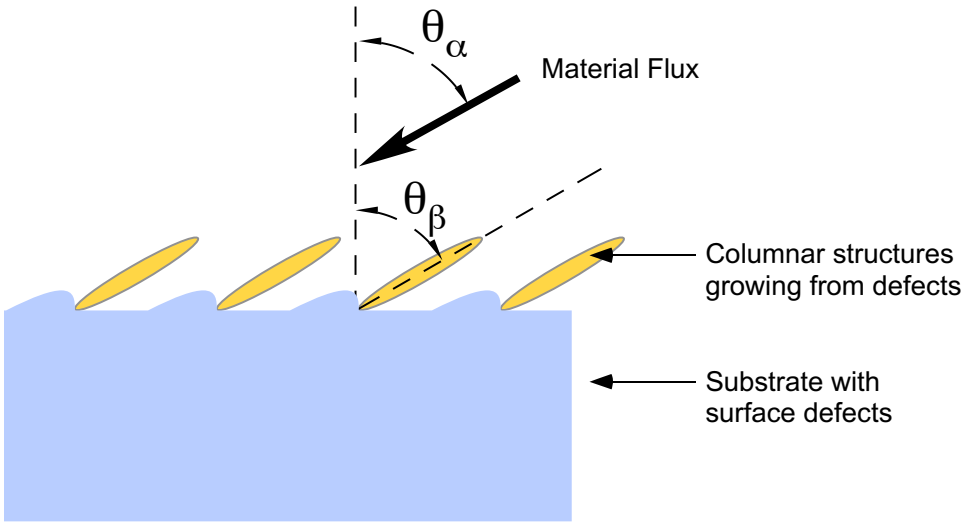

Figure 5.1: A schematic of columnar growth during glancing angle deposition (GLAD).

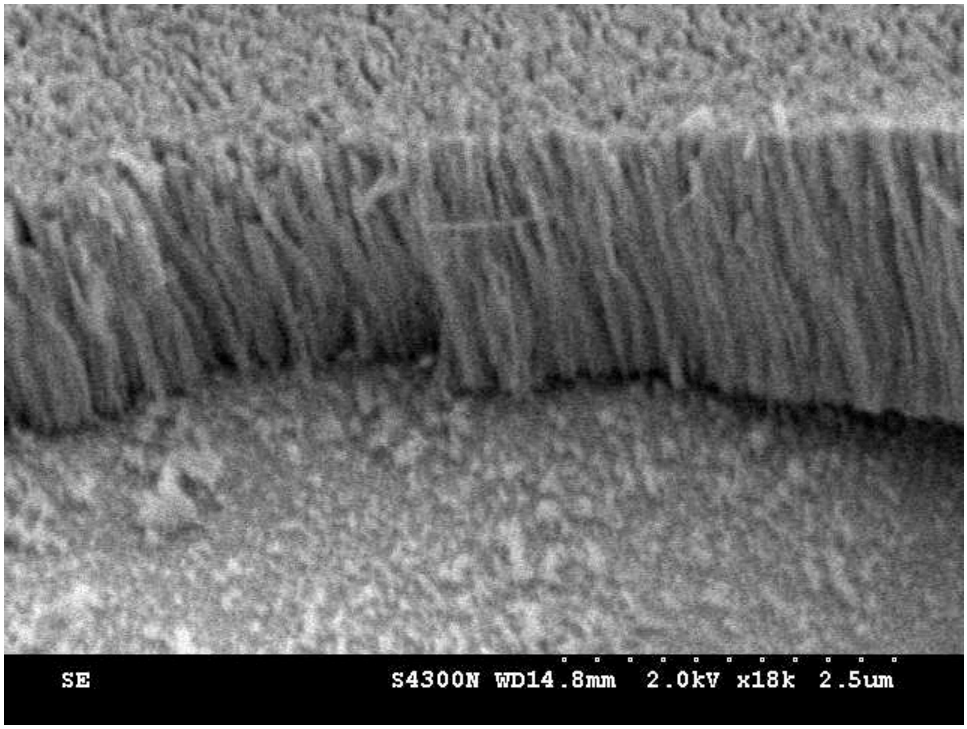

Figure 5.2: A scanning electron microscope cross-sectional view of CaF_2 columns, approximately 2μm long, grown on Si. The sample stage is tilted at 50°.

the average dimensions of the nanoparticle, the effective 'lattice constant' - analogous to the nanoparticle-nanoparticle separation - of an array of nanoparticles on the substrate, angle of incidence and polarization of incident light, together with the optical properties of Au, BK7 and CaF_2. Both the MFTA and GranFilm programs will be used extensively throughout this dissertation.

5.1.2 Results and Discussion

Figure 5.3 shows an AFM image of 50nm Au ($\alpha = 85^o$) on 50nm CaF_2. The direction of material flux is from left to right across the image, evident from the abrupt terminations on the right-hand side of the particles. Elongated structures are visible in the image. The direction of material flux during deposition is from left to right, as the slightly truncated right-hand sides of the nanoparticles suggest. Each are similar in size, shape and orientation. Surface coverage is high, with the nanoparticles often overlapping and growing on top of others.

Figures 5.4(a) through 5.9(a) show SEM images of various Si-substrate samples showing well orientated nanoparticles with major axes parallel to the direction of material flux. The nanoparticles are close-packed, well defined and have a elongated geometry similar to prolate spheroids. Pertinent experimental data, together with values input into each model, is presented in Table 5.2.

ImageJ [83] was used to determine N, r_0 and z_0 for each of the samples. The minor-to-major axis ratio $R_{pro} = r_0/z_0$ and prolate spheroidal shape parameter $\eta_{pro} = (1 - R_{pro}^2)^{-1/2}$ are calculated.

Figures 5.4(b) through 5.9(b) show the experimental and modeled absorbance spectra of various BK7-substrate samples. No particular scaling or normalization processing was applied to any of the spectral data presented as the native absorbance measurement (spectrophotometer) and model outputs (MFTA and GranFilm) are comparable. Each of the experimental spectra show similarities, for example, a broad main absorption peak in the 500-800nm range due to surface plasmon resonance on the nanoparticle, together with a smaller peak around 400nm due to interband transitions in Au. Both the MTFA and GranFilm models show these details in varying degrees of clarity.

Samples with 50nm Au and different CaF_2 deposition parameters show distinctly different absorbance spectra. nanoparticles on smoother surfaces exhibit a substantially red-shifted broad peak in the NIR as a consequence of η approaching unity. The highest density of nanoparticles is obtained on smoother surfaces with the density decreasing as surface roughness increases.

The different widths of the absorption peaks may be explained with reference to the distribution of nanoparticle geometry and nanoparticle-nanoparticle interactions. The MTFA model takes into account a Gaussian distribution of nanoparticle shape parameter about the average whereas GranFilm does not. The nanoparticle-nanoparticle interaction can be modeled in GranFilm by assuming the nanoparticles exist on a square or hexagonal lattice and by the user varying the lattice constant (i.e., nanoparticle-nanoparticle separation). The MFTA model lacks this capability. The average nanoparticle-nanoparticle separation on all samples was determined from SEM images and is shown in Figure 5.10 as a function of CaF_2 thickness. These values are input into GranFilm as the lattice constants for a square nanoparticle array.

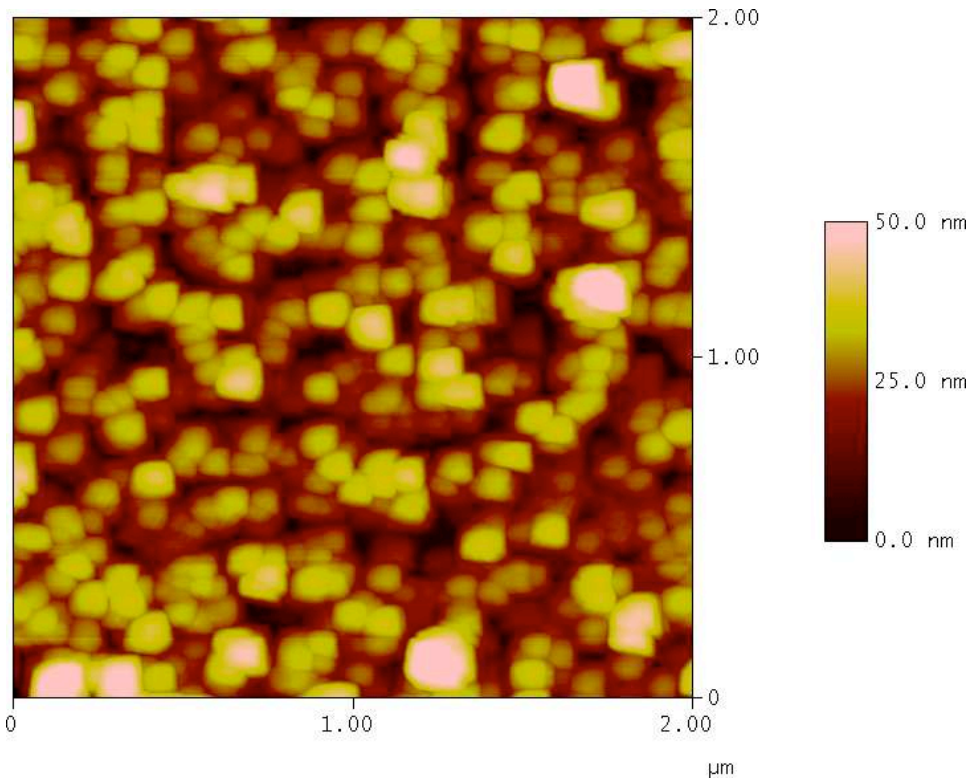

Figure 5.3: AFM image of 50nm Au on 50nm CaF_2. The direction of material flux during deposition is from left to right, as the slightly truncated right-hand sides of the nanoparticles suggest.

Table 5.2: Average major and minor nanoparticle axis lengths and the prolate spheroid shape parameter η for a variety of different sample configurations. Also tabulated are the average nanoparticle-nanoparticle separations, input into the GranFilm model as the lattice constants.

CaF_2 (nm)	Au (nm)	N (10^{14} m^{-2})	z_0 (nm)	r_0 (nm)	$\eta_{pro} \pm$ st. dev.	Avg. NP-NP separation (nm)
20	50	10.0	56.6	21.4	1.080 ± 0.027	34.9
25	50	10.2	69.7	28.6	1.097 ± 0.034	40.2
50	50	8.7	72.9	33.4	1.125 ± 0.054	57.9
100	50	7.7	80.0	34.4	1.107 ± 0.046	78.2
200	50	4.8	81.5	36.5	1.118 ± 0.065	87.9
378	50	4.4	89.3	44.7	1.155 ± 0.133	109.1
50	100	2.4	106.2	45.7	1.107 ± 0.044	76.0
50	200	2.0	181.6	52.0	1.044 ± 0.010	76.2
50	300	1.9	240.3	56.4	1.029 ± 0.004	74.3

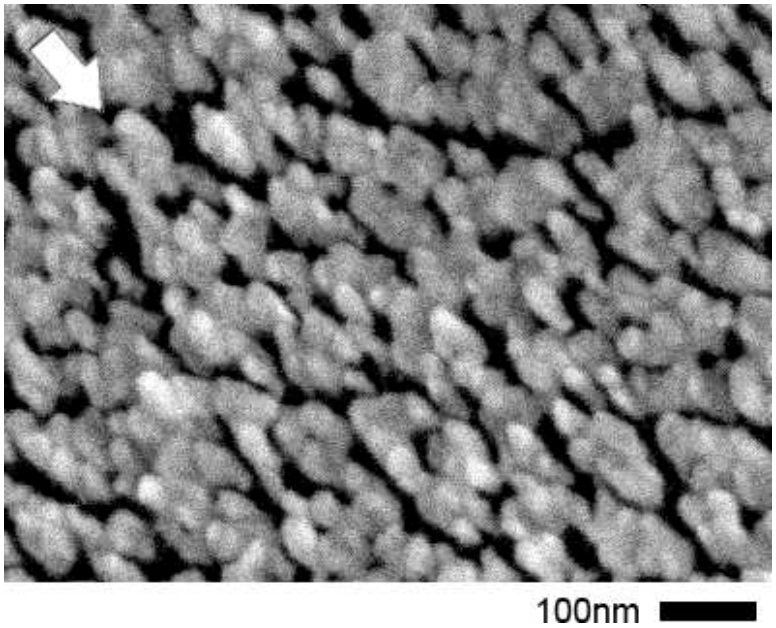

(a) SEM image showing high coverage of nanoparticles which are difficult to individually resolve. Nanoparticles have a well-defined orientation, growing in the direction of material flux as indicated by the arrow.

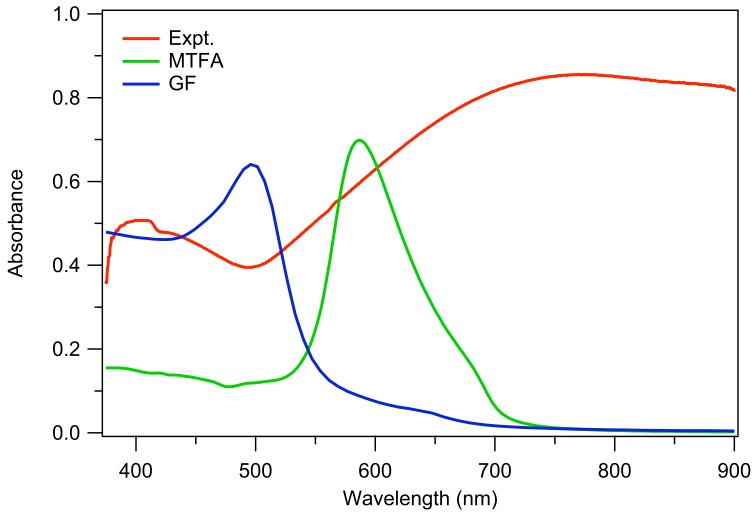

(b) Experimental and modeled absorbance spectra showing peaks located at 769.6nm, 585.7nm and 495.7nm for the experimental, MTFA and GranFilm (GF) models respectively.

Figure 5.4: 50nm Au on 25nm CaF_2.

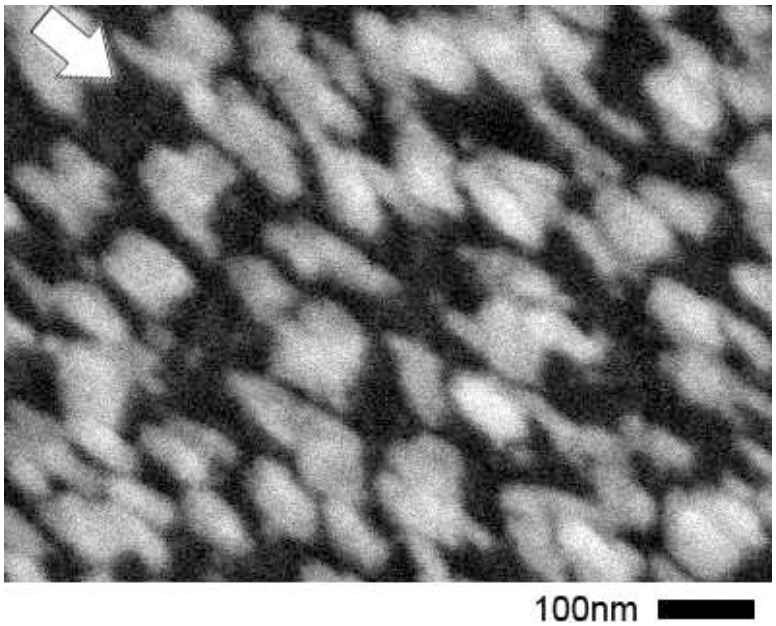

(a) SEM image showing medium coverage of nanoparticles which can be resolved individually to a degree. Nanoparticles have a well-defined orientation, growing in the direction of material flux as indicated by the arrow. The SEM image lacks clarity and sharpness as a result of charging effects due to the insulating 100nm CaF_2 layer on the Si substrate.

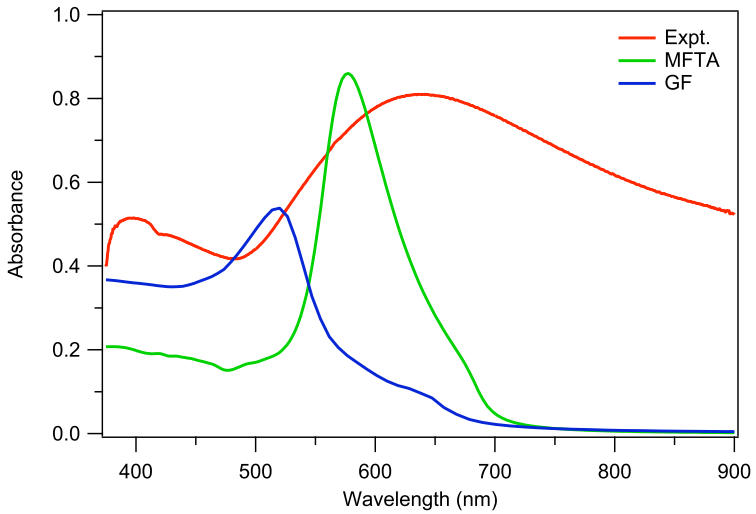

(b) Experimental and modeled absorbance spectra showing peaks located at 638.0nm, 577.5nm and 520.1nm for the experimental, MTFA and GranFilm models respectively.

Figure 5.5: 50nm Au on 100nm CaF_2.

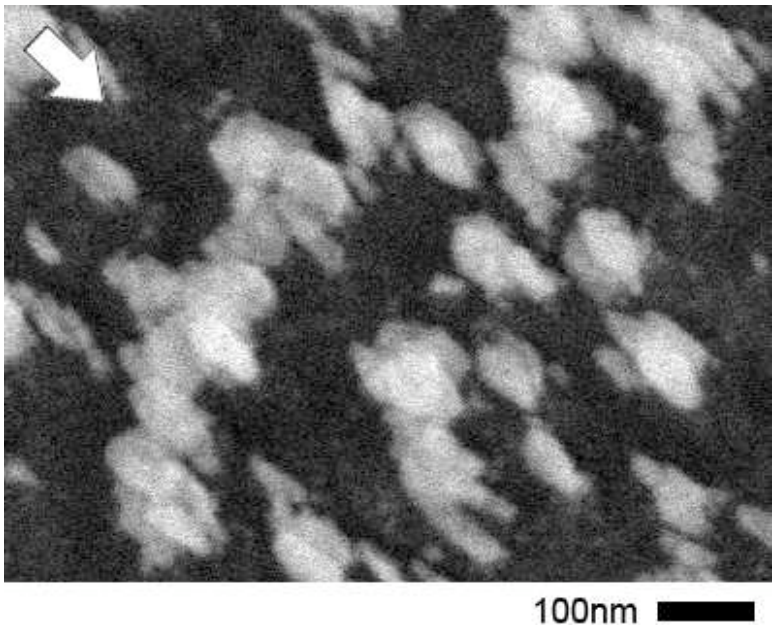

(a) SEM image showing relatively low surface coverage of nanoparticles which can be resolved individually. Again, the nanoparticles have a well-defined orientation, growing in the direction of material flux as indicated by the arrow. The SEM image lacks clarity and sharpness as a result of charging effects due to the insulating 378nm CaF_2 layer on the Si substrate.

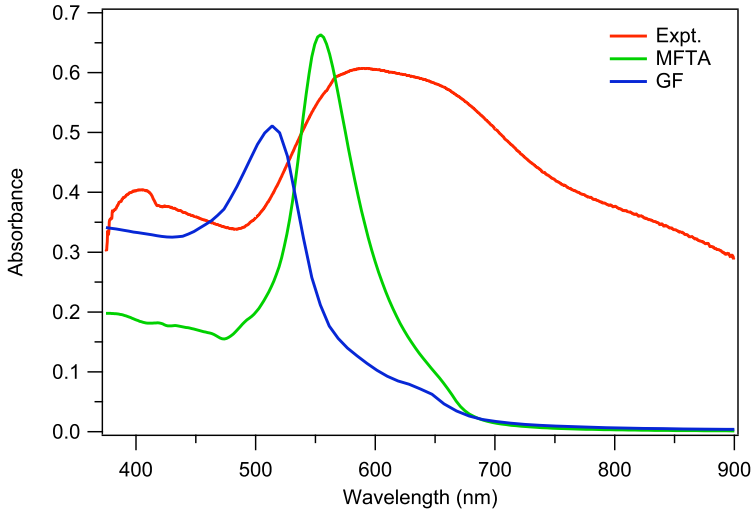

(b) Experimental and modeled spectra showing peaks located at 589.0nm, 554.3nm and 513.8nm for the experimental, MTFA and Gran-Film models respectively.

Figure 5.6: 50nm Au on 378nm CaF_2.

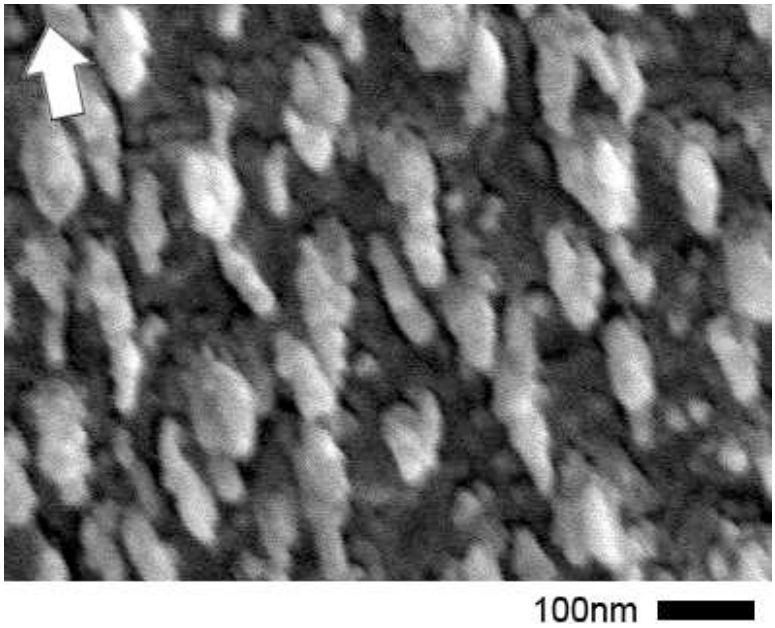

(a) SEM image showing individual elongated nanoparticles with a well-defined orientation. The arrow indicates the direction of material flux during deposition. The nanoparticles can be individually resolved.

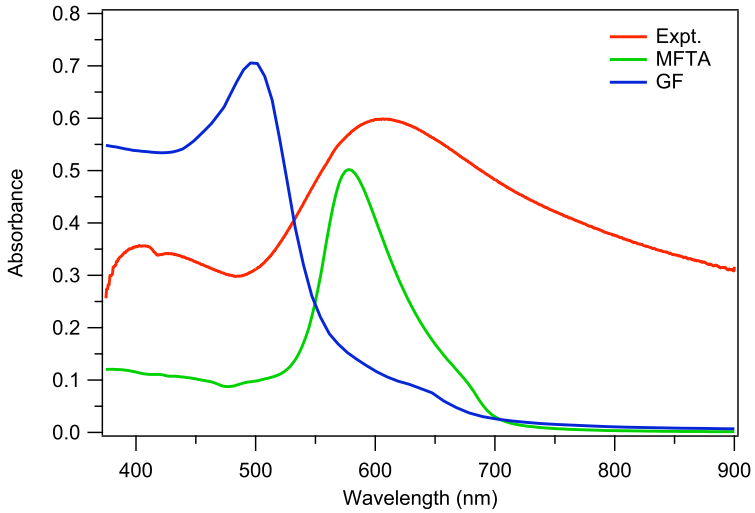

(b) Experimental and modeled spectra showing peaks located at 603.8nm, 577.5nm and 501.6nm for the experimental, MTFA and Gran-Film models respectively.

Figure 5.7: 100nm Au on 50nm CaF_2.

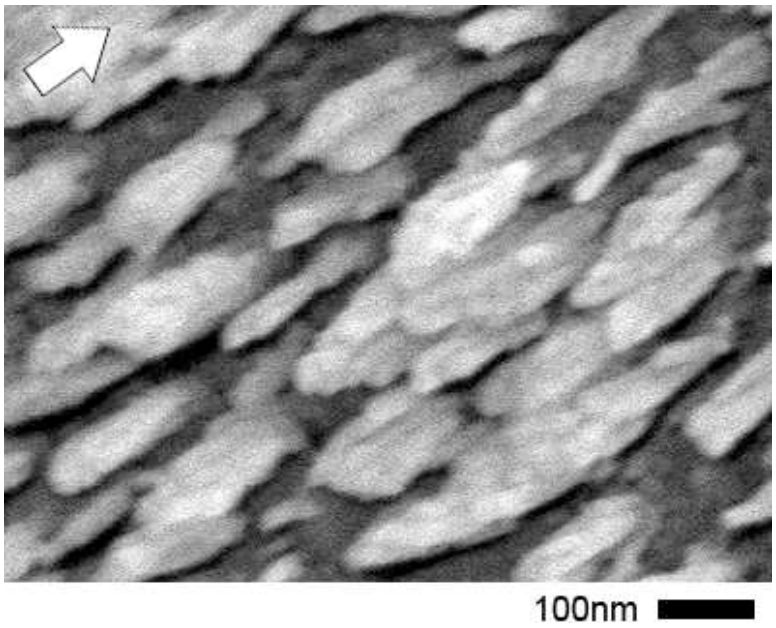

(a) SEM image showing individual elongated nanoparticles with a well-defined orientation. The arrow indicates the direction of material flux during deposition. The nanoparticles may be individually resolved. However, due to the increase in material deposited on the surface, the nanoparticles now begin to overlap and coalesce, resulting in a broader red-shifted absorption peak in (b).

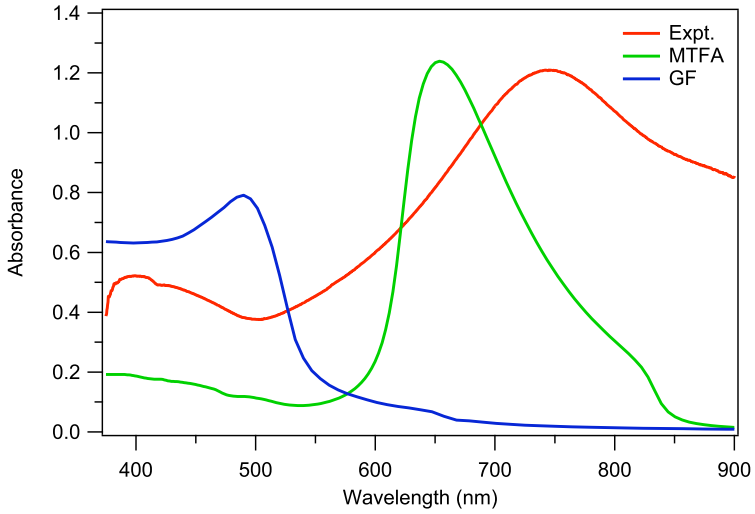

(b) Experimental and modeled spectra showing peaks located at 742.2nm, 653.5nm and 490.0nm for the experimental, MTFA and Gran-Film models respectively.

Figure 5.8: 200nm Au on 50nm CaF_2.

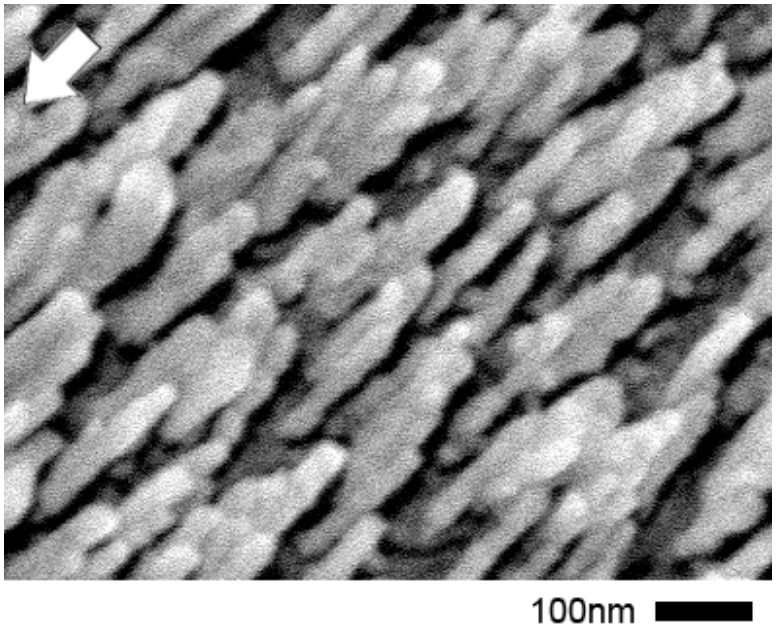

(a) SEM image showing individual elongated nanoparticles with a well-defined orientation. The arrow indicates the direction of material flux during deposition. The nanoparticles may be individually resolved. However, due to the increase in material deposited on the surface, the nanoparticles now begin to overlap and coalesce, resulting in a broader red-shifted absorption peak in (b).

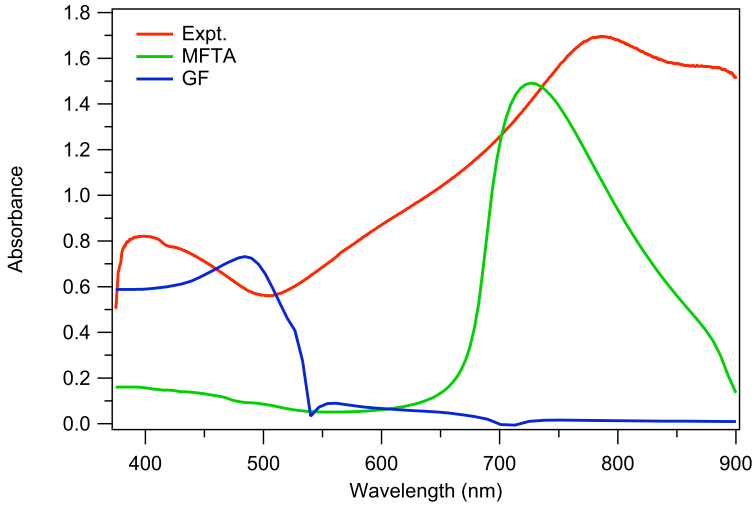

(b) Experimental and modeled spectra showing peaks located at 785.4nm, 726.1nm and 484.4nm for the experimental, MTFA and Gran-Film models respectively.

Figure 5.9: 300nm Au on 50nm CaF_2.

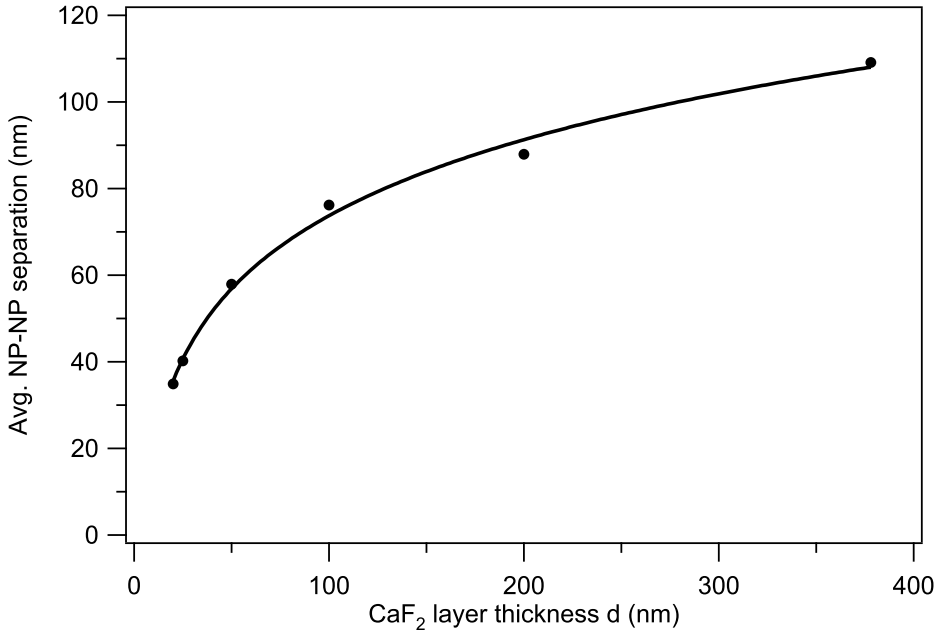

Figure 5.10: Average nanoparticle-nanoparticle spacing versus CaF_2 layer thickness.

A surface with a smaller RMS surface roughness will act as small obstructions impeding the flux of evaporating Au during deposition. A much rougher surface, with larger RMS surface roughness, provides larger obstacles and a greater surface area to impede evaporating Au atoms. As the initial Au atoms anchor onto the CaF_2 surface, growth is predominantly in the direction of material flux. However during the deposition process, Au arriving at later times will undergo random motion over the nanoparticle surface until it reaches thermal equilibrium. As a result, Au is not necessarily added to the nanoparticle's tip, but has the possibility of coalescing anywhere on the accessible surface of the nanoparticle. It appears nanoparticle growth in this fashion should be considered as an increase in all particle dimensions, with a propensity for growth along a certain direction.

Samples with 50nm CaF_2 and Au deposition parameters varied show distinctly different spectra also. The average major axis length is comparable with the amount of Au deposited. Although the minor axis length also increases, η is reduced and results in the resonance being red-shifted. The number density of nanoparticles decreases slightly with an increased Au deposition, but the total absorbance of the samples increases substantially due to the increase in coverage.

The MTFA model compares better with the experimental data than GranFilm with increasing surface roughness. It is unlikely that the nanoparticles are perfect prolate spheroids, as has been assumed for the purpose of modeling, but may be better described using a combination of prolate and oblate spheroids and ellipsoids.

The MTFA and GranFilm models compare well with experimental data with respect to reproducing the main features in the absorbance spectra. However, both the MTFA and GranFilm models lack agreement when compared quantitatively to the experimental absorbance spectra. The MTFA produces spectra with main absorption peak positions that are consistently closer to the experimental values than GranFilm when using experimentally determined model inputs.

The GranFilm spectra are, however, strongly dependent on the lattice constant input. Figures 5.11 and 5.12 show the modeled absorbance curves for two distinct nanoparticle shapes over a range of different lattice constants (nanoparticle-nanoparticle separation) with $\eta = 1.0910$ and 1.0206, corresponding to $R_{pro} = 0.4$ and 0.2, respectively. In both cases, comparison is made with the spectra of a uniform thin-film structure of vacuum-Au-CaF_2-BK7 and the spectra of a similarly shaped nanoparticle from the MTFA model. As the lattice constant is decreased (nanoparticles closely spaced) in the GranFilm model, the absorbance spectra tends towards the thin-film spectra, with the peaks being blue-shifted, as one would expect. As the lattice constant is increased (nanoparticles widely spaced) the absorbance peaks are red-shifted towards the MTFA spectra.

5.1.3 Conclusions

The optical response of Au nanoparticles deposited onto roughened dielectric substrates is dependent on the severity of surface roughness and the film deposition parameters. In particular, a rougher surface with Au deposited at a glancing angle produces distinct spheroid-shaped nanoparticles resulting in stronger resonances with narrower linewidths. Smoother films result in broad red-shifted absorbance spectra due to densely packed, needle-shaped particles. By selecting both CaF_2 and Au deposition parameters, the density, shape and therefore optical response of Au nanoparticles can be controlled.

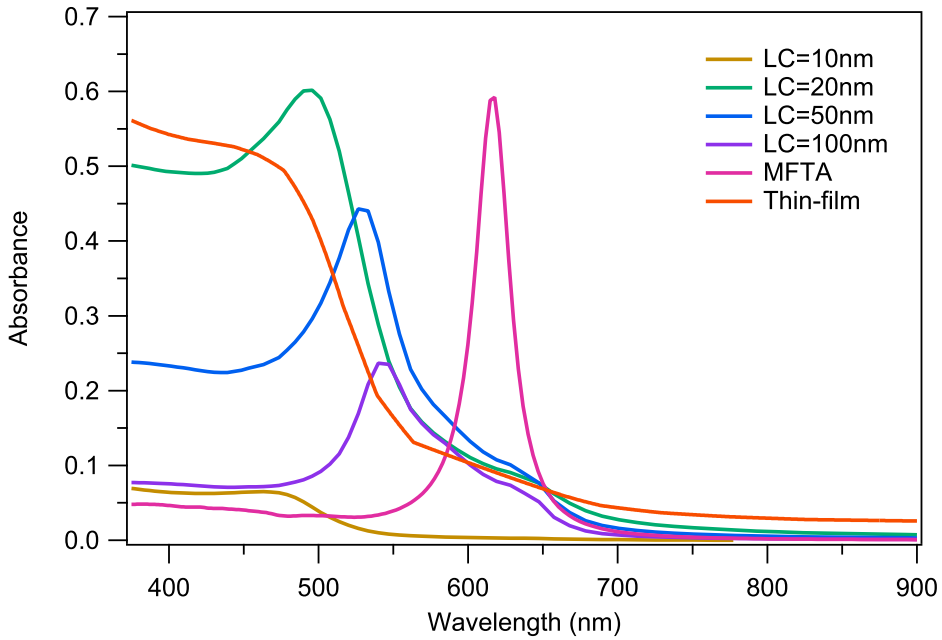

Figure 5.11: Modeled absorbance spectra for different values of the GranFilm lattice constant (LC) for an array of prolate spheroidal nanoparticles with $\eta_{pro} = 1.091$, i.e., $z_0 = 50$nm, $r_0 = 20$nm. As the lattice constant decreases the absorbance spectra approaches that of a 50nm thick continuous Au film on 50nm CaF_2. Conversely, as the lattice constant is increased, the spectra tends towards that given by the MTFA model.

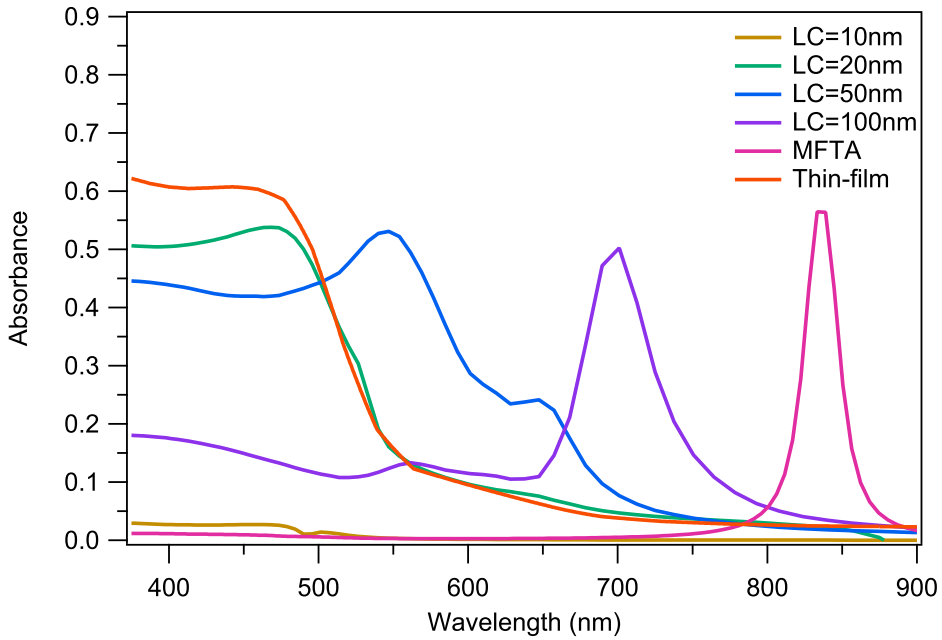

Figure 5.12: Modeled absorbance spectra for different values of the GranFilm lattice constant (LC) for an array of prolate spheroidal nanoparticles with $\eta_{pro} = 1.0206$, i.e., $z_0 = 100$nm, $r_0 = 20$nm. As the lattice constant decreases the absorbance spectra approaches that of a 100nm thick continuous Au film on 50nm CaF_2. Conversely, as the lattice constant is increased, the spectra tends towards that given by the MTFA model.

Clearly, the size and distribution of the surface roughness features is a large factor on nanoparticle formation, growth and final dimensions. Greater control of the optical response may be realized by specifically engineered surface roughness features such as lithographically produced anchor points over a large area. Additional improvements may be realized by employing a sample position control system during deposition. Further work into the formation and growth of vapor-deposited nanoparticles may result in controlled anisotropic growth, enabling the shape of nanoparticles to be tailored more accurately.

GLAD can create particles of carious sizes and shapes. But particles are quite large ($\sim$ 300nm) with large surface coverage. Whereas this might offer advantages in certain fields such as optical filter fabrication, SERS, for this study of thermo-optical effects, the GLAD method as described above was felt to be unsuitable. To obtain samples with strong absorption at a pump wavelength of λ=1.48μm, the particles must be longer and narrower. Depositing more Au to shift the absorption peak into the IR will lead in micron-sized particles, resulting in longer heating and cooling times.

The method of using nanoscale surface features as anchors for nanoparticle growth is promising, leading to the second fabrication method, laser lithography.

5.2 Laser Lithography

M. Buncick demonstrated the growth of ellipsoidal nanoparticles on submicron post structures created using nanosphere lithography [16]. This section presents results of investigations assessing using large-area lithographically produced nanostructures as nanoparticle growth nucleation sites. Such a surface would have controllable roughness, similar to CaF2 layers of the previous section, but with the added advantage of being periodic over a large area, unlike the randomness of the CaF2 approach.

All lithography processes involve the deposition of light- or electron-sensitive chemical layers called resists. Upon exposure to light or electrons of a specific energy range, polymer modifications occur in the resist, making the exposed resist more (positive tone)or less (negative tone) soluble in a developer solution. When a resist-coated substrate is exposed through a mask, the pattern on the mask is transfered to the resist. A developer solution dissolves the exposed or unexposed resist, depending on the resist tone, revealing the substrate beneath. Further processing steps, such as metallization, result in physical structures with a pattern faithful to the original mask. Finally, the remaining resist is stripped away by washing with a solvent. A standard lithographic process is illustrated in Figure 5.13.

A variation of optical lithography, laser interference lithography (LIL) [84] [85], is used in this work. In contrast with optical and electron-beam lithography, LIL requires no mask nor is the beam scanned across the surface. However, the patterns available are limited to very simple line-space gratings and periodic geometric structures. Whereas this is an obvious disadvantage in the semiconductor industry, where large-area simple periodic structures are required, the LIL method is ideal.

Briefly, laser light of a suitable wavelength is split into two portions of approximately equal intensity. Both beams are spatially filtered and recombined at the surface of a photoresist coated substrate. The resulting standing-wave interference pattern exposes the resist, transferring the interference pattern to the resist. The sample may be exposed several times, rotating the substrate between each exposures, to obtain different patterns. The typical spacing of structures is given by

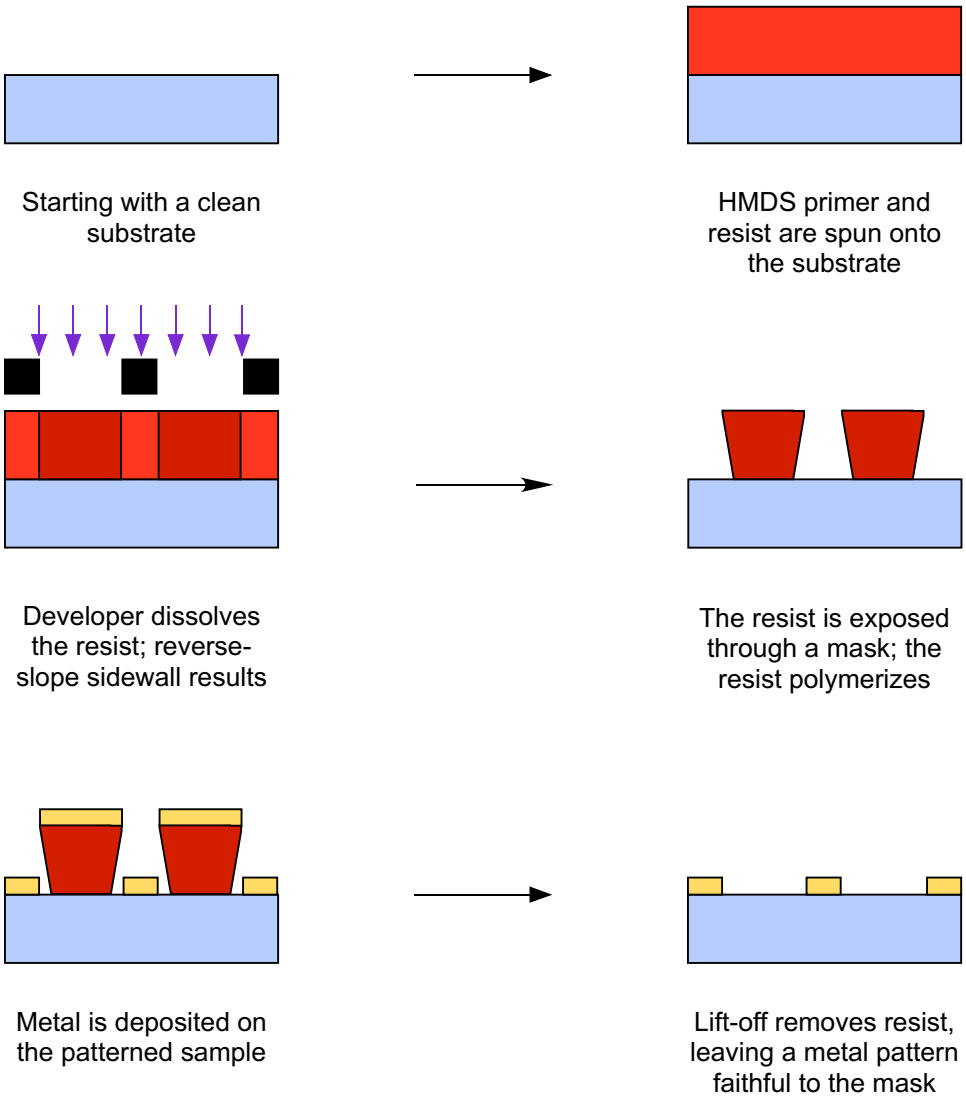

Figure 5.13: A typical lithographic process.

$$\Lambda = \frac{\lambda}{2\sin(\theta/2)} \tag{5.2.1}$$

where λ is the wavelength of the laser used and θ is the angle between the two recombining beams.

5.2.1 Experimental Method

All processing, other than exposure and metallization, is carried out in a ventilated hood with suitable lighting to filter UV and blue light. BK7 glass substrates are cleaned and treated with an adhesion promoter by spin-coating HMDS at 2.0 kRPM for 30 seconds. Next, photoresist SPR955-CM is spun onto the HMDS-coated substrate at 5.0 kRPM. Figure 5.14 shows the manufacturer's spin-speed data sheet. With a spin speed of 5.0 kRPM, an approximate resist thickness of 500nm is achieved. The substrates are then soft-baked on a hotplate at 100°C, measured with a Chromel/Alumel-type thermocouple, for 90 seconds as per the manufacturer's recommendations. The soft-bake step assists in evaporation of solvents and hardens the resist. The spin speeds for HMDS and resist are kept constant.

The substrates are placed on a coupling prism with index matching gel and are mounted in a rotatable stage in the optical set up shown in Figure 5.15. The prism is used to prevent back-reflections from the substrate surfaces which can further expose the resist and lead to undesirable effects on the resulting pattern. A HeCd laser beam with emission lines at 325nm and 442nm is used as the exposure tool. The 442nm wavelength is selected, with the 325nm line blocked. Upon emerging from the laser aperature, the beam is passed through a polarization rotator to ensure *s*-polarization at the sample surface, and split into two approximately equal intensity portions by a non-polarizing beam splitting cube. Both beams are then passed through identical spatial filters, consisting of a 20X microscope objective focused onto a 5μm pinhole. One beam path includes a neutral density filter prior to the spatial filter assembly. The intensity of each beam is measured separately at the sample with a photodiode and adjustments to the neutral density filter made to ensure equal beam intensities.

The beam recombination angle θ is set at 90° with the beams positioned to overlap on the substrate surface. A mechanical shutter is placed in front of the laser aperature to prevent exposure during the sample loading and rotation phases. When the sample is in place, the shutter is opened for a specific length of time, exposing the resist.

After the desired exposure step(s), the sample is post-exposure baked, as recommended by the manufacturer, on a hotplate at a temperature of 110°C for 90 seconds. The sample is removed and allowed to cool to room temperature before being placed in the CD-26 developer solution for a specific length of time. Development is stopped by immersing the sample in deionized water. The sample is removed, dried using a stream of nitrogen and loaded into an electron-beam evaporator vacuum chamber for the metallization process. 5nm of Cr for adhesion followed by 20nm of Au are deposited at $\sim$ 5Å/s, at a chamber pressure of $\sim 1 \times 10^{-6}$ Torr, on the patterned surface to aid SEM imaging.

Lift-off, where the resist is removed to leave behind only metallized structures in the interference pattern, is the final step in the fabrication process. A successful lift-off requires reverse-slope vertical sidewalls, shown in Figure 5.13, in order to prevent removal of the

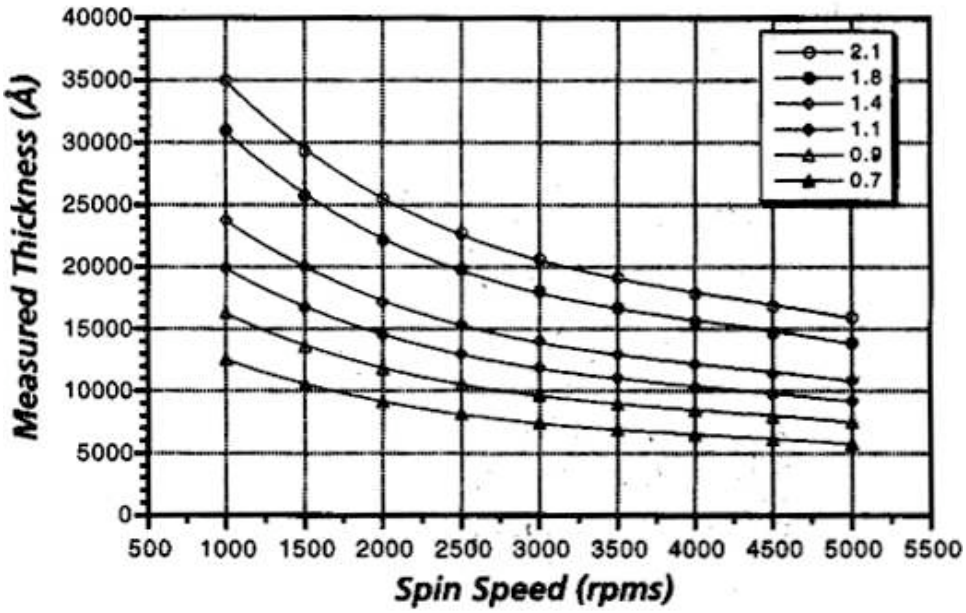

Figure 5.14: Rohm & Haas SPR955-CM spin-speed curves.

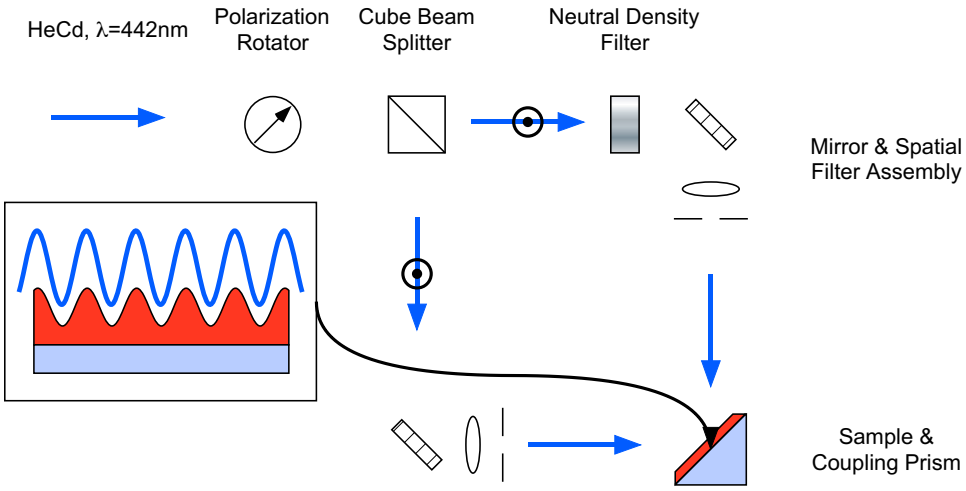

Figure 5.15: Laser Interference Lithography (LIL) Optical Setup. Inset shows the sinusoidal interference pattern formed by the recombination of beams and the resulting pattern transferred into the photoresist.

metal when the resist is stripped away. Lift-off is problematic with LIL as the light intensity, therefore the exposed photoresist, has a sinusoidal profile at the surface. To achieve lift-off, the resist must be fully exposed to the surface. Otherwise, metallization results in the metal being deposited on the resist and is removed during the lift-off step. Complete exposure can be achieved by carefully selecting appropriate exposure and development times. Approximate exposure times can be calculated from the energy dose required to expose the photoresist and output power of the exposure tool. Thicker resists require a longer exposure time or higher exposure dosage in order to expose down to the substrate. The developer dissolves the resist at different rates depending on the degree of exposure. Too short of a develop step will not remove much resist, too long will start to dissolve the unexposed resist, affecting the pattern quality. Exposure and development times are optimized visually following an iterative method in which the patterned features on the substrate are examined using electron microscopy.

The variables involved in fabricating lithographic samples are numerous and include the resist thickness, exposure (t_e) and development times (t_d), developer type, concentration and temperature, to name a few. Only two variables, the exposure and develop times, are changed in the LIL experiments. Effort is made to ensure all others kept constant unless otherwise noted.

5.2.2 Results & Discussion

Figures 5.16 - 5.18 show SEM images of samples with different exposure times. Figure 5.16 shows features that are barely visible. Figure 5.17 shows features visible, well transferred into the resist, but do not reach substrate. Lift-off subsequently fails as the metal is deposited onto the resist. Figure 5.18 shows a sample having undergone a long exposure. The resist is exposed and removed down to the substrate, but with catastrophic consequences. The resist structures fail due to height instability, suggesting the resist layer is too thick or pattern too small to be supported by this resist. The collapsing resist structures topple into eachother, resulting in this 'domino' effect. Figure 5.19 shows two exposures of length with a 90 degree rotation between exposures. Periodic arrays of nanoscale squares would result if lift-off were successful.

The structural failure of the resist must be addressed if the LIL method is to be successful. The spacing between the features can be increased by selecting a longer exposure wavelength or reducing the beam overlap angle, or the resist may be made thinner by a faster spin speed or dilution with an appropriate solvent. 442nm is already at the limit of exposure wavelengths for SPR955-CM and exposing with a longer wavelength may not result in any polymerization within the resist at all. Modifying the optical set up is an option, but undesirable due to the intensive optical realignment procedures. Faster spinning of the resist is possible, but only upto 6.0 kRPM, the upper limit on current spin-coater, which would not significantly reduce the resist thickness as illustrated in Figure 5.14. Diluting the resist with an appropriate solvent was chosen.

The manufacturer's data sheet for SPR955-CM lists ethyl lactate (EL) as the major solvent by percentage volume. Mixing measured volumes of resist and EL will further dilute the resist, resulting in thinner layers. Four concentrations of resist:EL mixtures were created using a calibrated volume dropper in the ratio 1:1, 1:2, 1:4, 1:8. Samples were fabricated with different resist concentrations and the exposure and development times

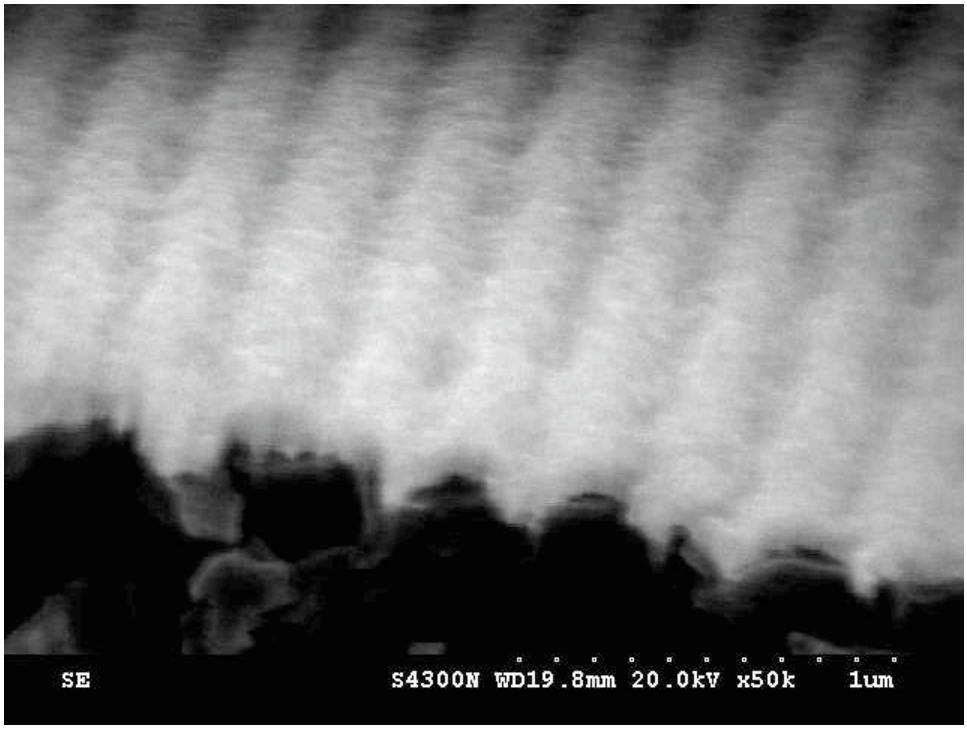

Figure 5.16: Cross-sectional SEM image of sample LL13-3, $t_e = 30$s, $t_d = 90$s. The interference pattern from the laser interference is barely visible on the surface, suggesting a longer exposure is required. The blurred edges are caused by the 20nm Au conductive coating peeling away from the resist. The sample stage at tilted to 60°. Contrast and brightness has been enhanced in order to highlight faint detail.

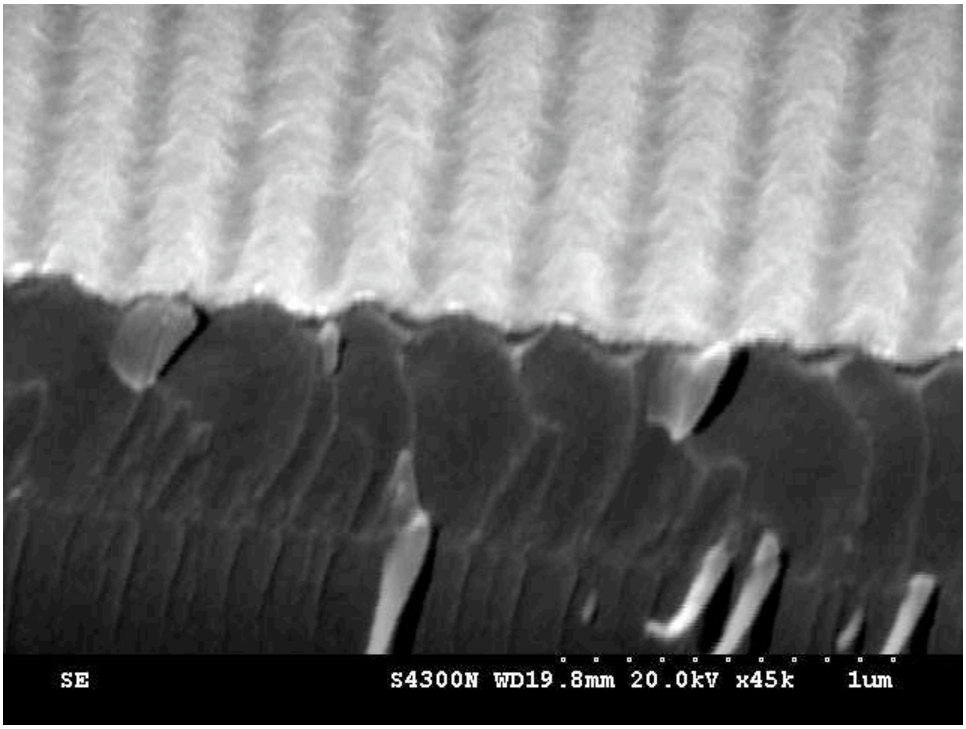

Figure 5.17: Cross-sectional SEM image of sample LL13-6, $t_e = 60$s, $t_d = 90$s. This sample exhibits a much clearer pattern than in Figure 5.16 having been exposed for longer duration. The sinusoidal interference pattern has been transfered into the resist and is clearly visible. The sample stage is tilted at 60°. Contrast and brightness has been enhanced in order to highlight detail.

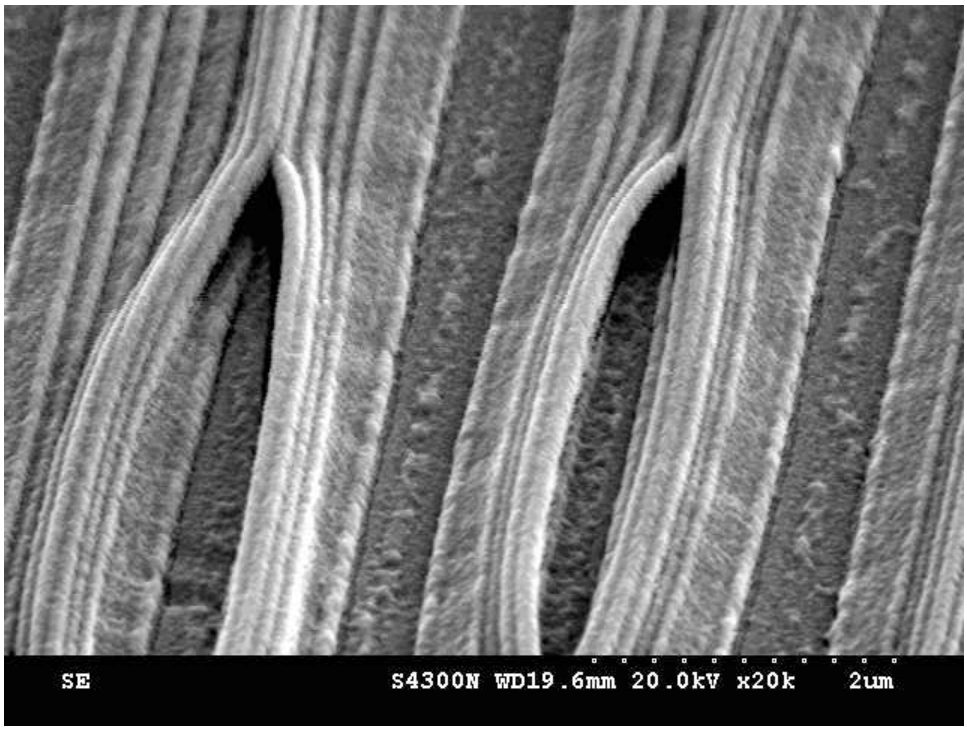

Figure 5.18: Cross-sectional SEM image of sample LL13-9, $t_e = 90$s, $t_d = 90$s. This sample was over-exposed, leading to the resist failing and buckling. The sample stage is tilted at 60°. Contrast and brightness has been enhanced in order to highlight detail.

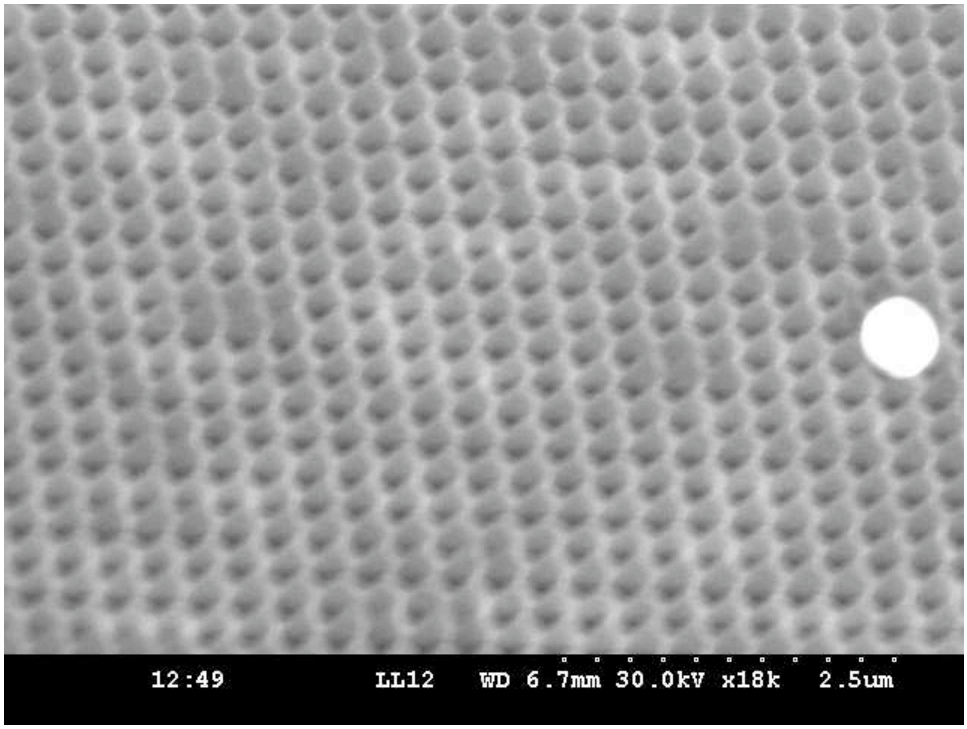

Figure 5.19: Cross-sectional SEM image of sample LL12-2. Two $t_e = 60$s exposures with a 90° rotation, $t_d = 90$s. This sample shows the periodic 2D structure formed by two equal exposures. The bright object to the right of the image is a gold particle sputtered during deposition. The sample stage is tilted at 45°. Contrast and brightness has been enhanced in order to highlight detail.

adjusted accordingly. Resist exposure and removal down to substrate is now possible, but due to the thinner resist and sinusoidal interference pattern, lift-off is difficult as the reverse slope sidewall profile is hard to obtain. Figures 5.20 - 5.22 show SEM images of various lift-off attempts on thinner resist samples. Some areas on show excellent lift-off results. However, nearby areas on the same sample show the results of failed liftoff as shown in Figure 5.22. These results are typical. It was difficult to obtain successful lift-off over a large area, as shown in Figure 5.20, and more difficult to reproduce the results.

5.2.3 Conclusions

The LIL method certainly offers promise in fabricating nanoparticle and nanoparticle anchor arrays over a large area. However, success with LIL remained tantalizingly out of reach in these experiments, but shows reasonable progress can be made with no specialized lithographic equipment. Success may be possible by using a bleached resist which has a threshold exposure level and is well-suited to the sinusoidal intensity profiles of the laser interference pattern.

5.3 Metal Island Films

Metal-islands (MIs) are essentially small discontinuous films obtained by vacuum deposition of very small amounts ($\lesssim$ 5nm) of metal onto a substrate. The optical properties of MIs have been studied extensively [86] [87] and are often described as nanoparticles having oblate spheroidal geometry. MIs initially have a large shape and size distribution, although heat treatment by annealing will narrow the distribution considerably. The fabrication of MI samples is relatively easy and well understood.

MIs are investigated in this section as a method to fabricate suitable nanoparticle samples. The previous two methods, GLAD and LIL, showed great promise for nanoparticle fabrication methods, however they were found unsuitable for the problem at hand. In this respect, MIs are ideal, consisting of small ($\lesssim$ 100nm) isolated nanoparticles whose size and shape can be controlled to a certain degree by the deposition and annealing parameters. The disadvantage is that MIs cannot be grown to exhibit large shifts in the absorption spectra, as the GLAD method can, so the choice of eventual pump and probe beams is limited. This section will introduce the method used to fabricate MI samples ultimately used in the pump-probe experiments introduced later in Chapter 6.

5.3.1 Experimental Method

BK7 glass substrates are cut to 1in. x 1in. samples, each marked and given a unique identification. The substrates are cleaned, using a mild detergent with de-ionized (DI) water then with various solvents, in an ultrasonic agitation bath. The clean samples are removed, dried with high-purity dry nitrogen, and immediately loaded into a clean e-beam evaporation vacuum chamber.

Vacuum on the order of 1 $\times 10^{-6}$ Torr is obtained prior to deposition. Various thickness of Au, as measured by a quartz film thickness monitor, are evaporated at deposition rates $\sim 5\mathring{A}$/sec. Upon removal from the evaporator the absorbance spectra of each sample are

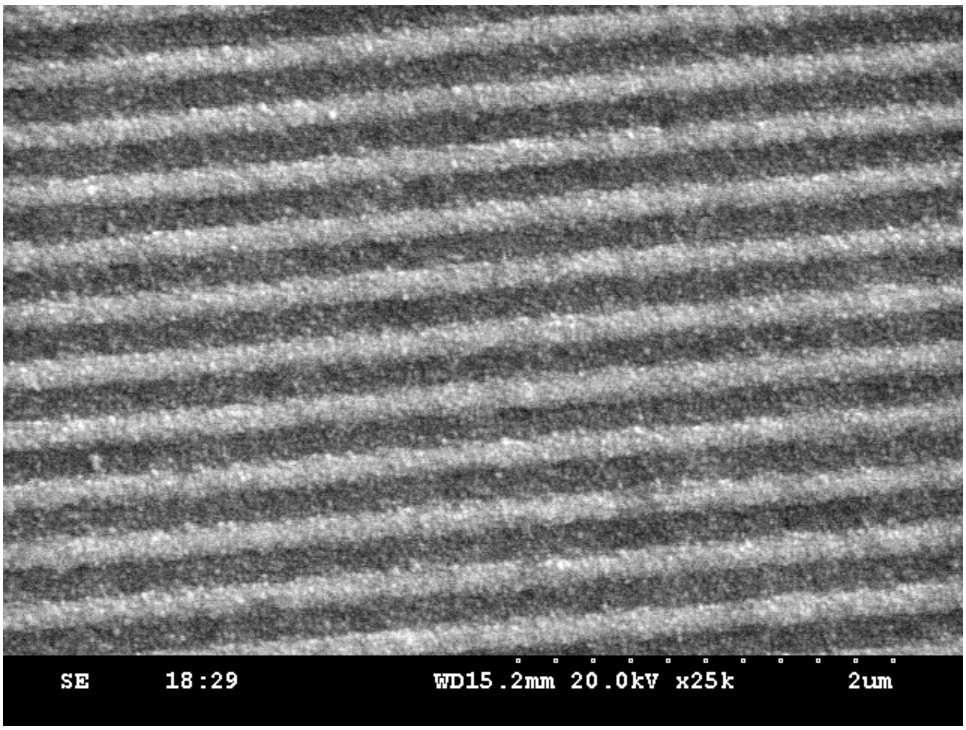

Figure 5.20: SEM image of sample LL21-4, t_e = 35s, t_d = 10s. This image shows the successful results of lift-off with Au lines clearly visible. The sample stage is not tilted. Contrast and brightness have been enhanced in order to highlight detail.

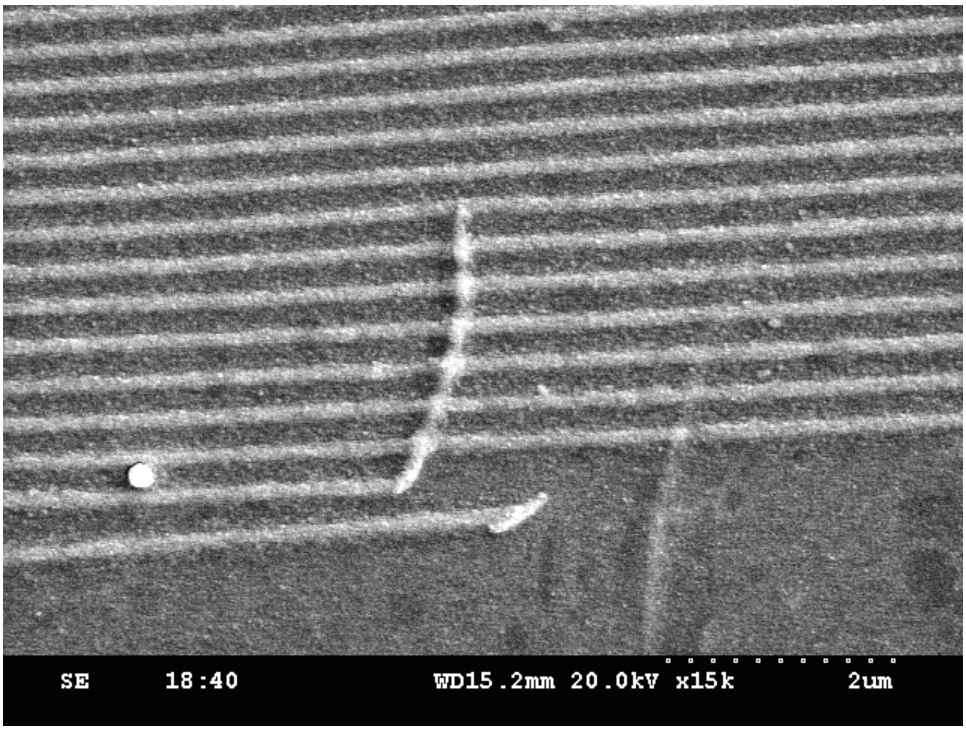

Figure 5.21: SEM image of sample LL21-4, $t_e = 35$s, $t_d = 10$s. This image shows poor lift-off with Au lines being broken and removed from the surface. The sample stage is not tilted. Contrast and brightness have been enhanced in order to highlight detail.

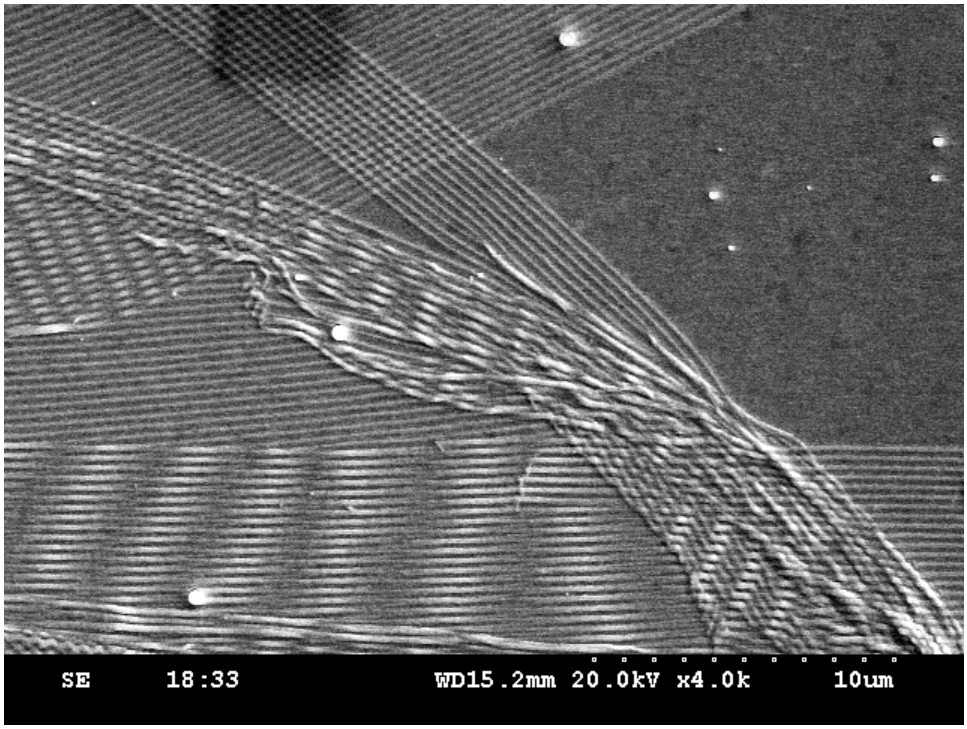

Figure 5.22: SEM image of sample LL21-4, $t_e = 35$s, $t_d = 10$s. This image shows poor lift-off with Au lines being broken and removed from the surface over a wider area than Figure 5.21. Unfortunately, results like this are typical. The dark rectangular region towards the top-left was previously imaged. The sample stage is not tilted. Contrast and brightness have been enhanced in order to highlight detail.

taken immediately, using a clean BK7 substrate as a reference, with p-polarized light. The polarizer films used show good transmission over their operating range of 400nm-1.2μm.

The annealing process is carried out on hot plate at various temperatures, measured with a Chromel/Alumel thermocouple, for a duration of 60 seconds. Studies show there is no discernible shift in the absorbance spectra between 60 second and 5 minute long anneals, although anneal durations of greater than 5 minutes were not performed. After annealing, absorbance spectra of each sample are obtained under the same conditions, with the shifts in the absorbance spectra noted.

5.3.2 Results & Discussion

Figures 5.23 - 5.25 show the absorption spectra for each sample obtained, prior and post-annealing at 200°C and 300°C, over a spectra range of 300nm to 900nm with a resolution of 0.2nm. The main details of these spectra are tabulated in Table 5.3 below.

Deposition of more Au results in a larger peak absorbance for all samples as both the number of nanoparticles and the surface area covered by nanoparticles increases. With no annealing, the absorption peaks are very broad due to the large distribution of nanoparticle size and shape. Annealing narrows and blue-shifts all spectra, regardless of sample, suggesting a narrowing of the nanoparticle size and shape distributions. Absorption peak blue-shifts are a result of the nanoparticles becoming more spherical (less oblate) after annealing. Higher annealing temperatures further narrow and blue-shift all samples to a greater degree. In theory, the absorption peaks may be blue-shifted to 483nm in Au, reached when the nanoparticle is a perfect sphere having a resonance condition ϵ = -2 as proscribed Mie. In reality, the nanoparticle cannot attain perfect sphericity because of surface tension and interactions with other nanoparticles.

The 3nm, 200°C sample process gave the highest absorbance at 514.5nm and therefore this method was chosen to fabricate samples for the pump-probe experiments. Figure 5.26 shows the p-polarized absorbance spectra taken at several sample orientations. For non-zero angles of incidence θ, it is possible to excite not only the long-wavelength $l = 1$, $m = 1$ mode, but also the short-wavelength $l = 1$, $m = 0$ mode. However, this resonance is predicted to exist around 340nm, and therefore could not be seen due to the poor performance of the polarizers in the UV spectral range.

Figure 5.27 shows a typical AFM image of PEGI66. Using this and similar images, the average nanoparticle size and surface density were found. The major axis r_0 = 35.2nm and the minor axis z_0 = 9.4nm. For a typical 500 x 500nm area, there was an average of 29 particles, suggesting $N = 1.16 \times 10^{14}$ m^{-2}. These parameters are input into both the modified thin-film approximation (MTFA) and GranFilm (GF) models.

Both models are different in how the optical properties of nanoparticles are calculated thus the particular parameters that provide the best fits with experimental data are also expected to differ. The MFTA inputs are the dimensions of the nanoparticle, the angle of incidence and polarization of light, the substrate and any applicable overcoating material and the number density N. GranFilm is a much more comprehensive package and includes inputs similar to the MFTA model in addition to options for the lattice constant (analogous to nanoparticle-nanoparticle spacing), nanoparticle truncation due to the substrate, inclusion of nanoparticle-nanoparticle interactions and more. Both models allow the dielectric

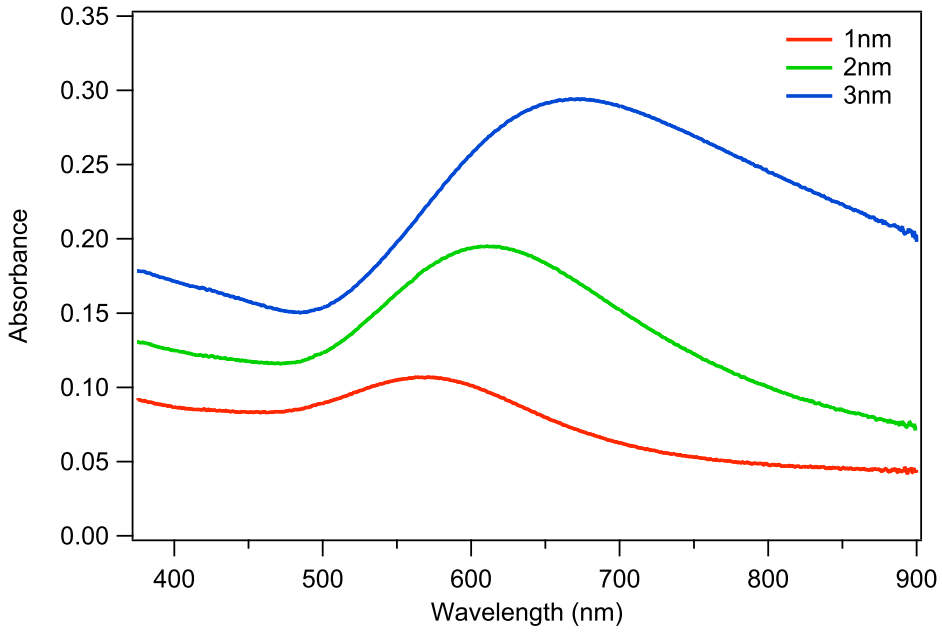

Figure 5.23: *p*-polarized absorbance spectra for samples of various evaporated film thickness (metal islands) with no anneal step.

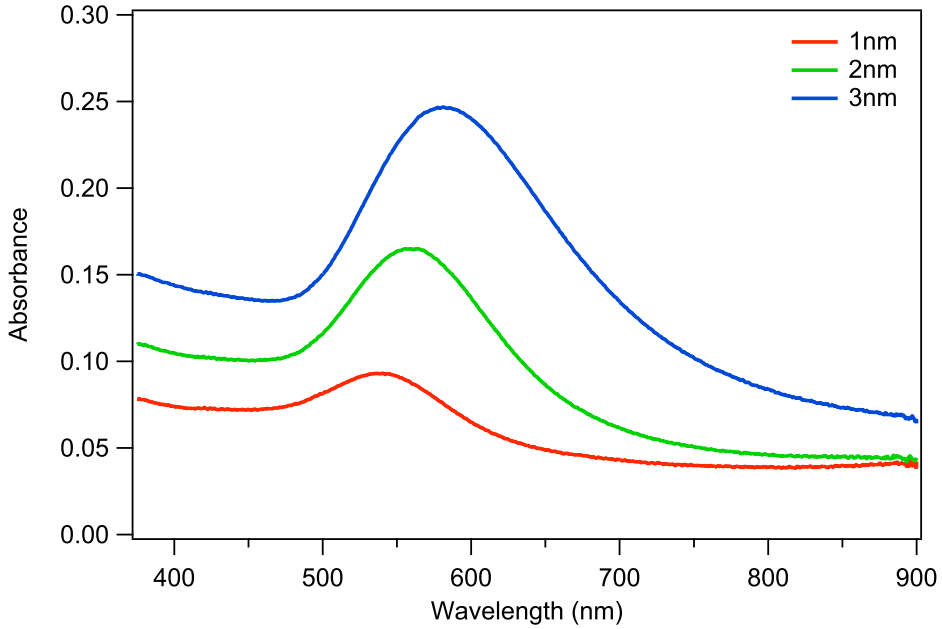

Figure 5.24: *p*-polarized absorbance spectra for samples of various evaporated film thickness (metal islands) with 200°C for 60 seconds anneal step.

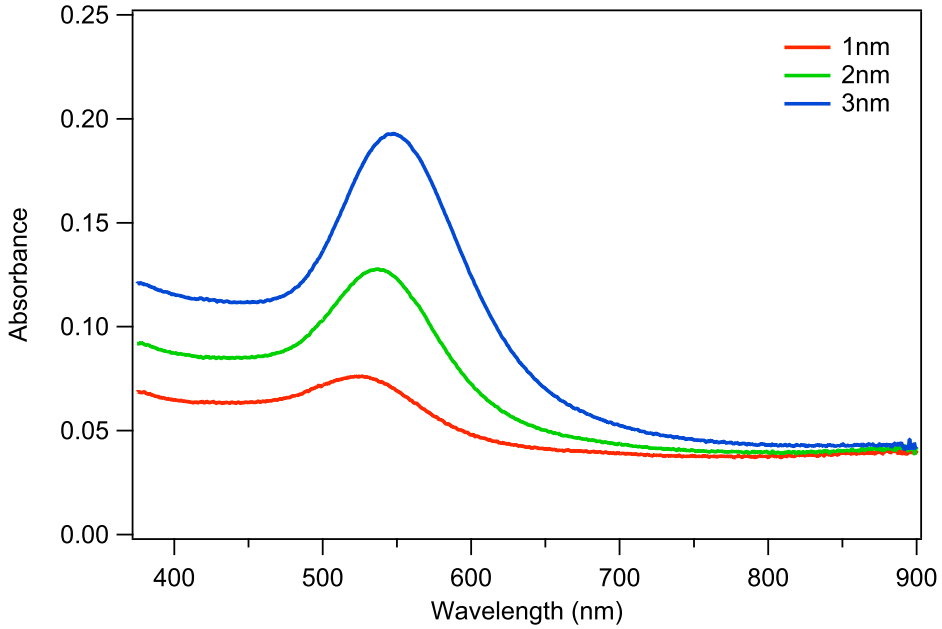

Figure 5.25: p-polarized absorbance spectra for samples of various evaporated film thickness (metal islands) with 300°C for 60 seconds anneal step.

Table 5.3: Absorbance data from 1, 2 and 3nm Au metal island film deposition thicknesses on BK7 glass showing the absorbance maxima and position, together with the absorbance at $\lambda = 514.5$nm.

Au (nm)	Anneal	Abs. Max	λ_{max} (nm)	Abs. (514.5nm)
1	none	0.107	571.2	0.094
2	none	0.195	611.6	0.132
3	none	0.294	671.6	0.162
1	200°C, 60 sec	0.093	540.6	0.087
2	200°C, 60 sec	0.165	559.0	0.131
3	200°C, 60 sec	0.247	581.2	0.169
1	300°C, 60 sec	0.076	522.2	0.075
2	300°C, 60 sec	0.128	537.8	0.116
3	300°C, 60 sec	0.193	548.0	0.158

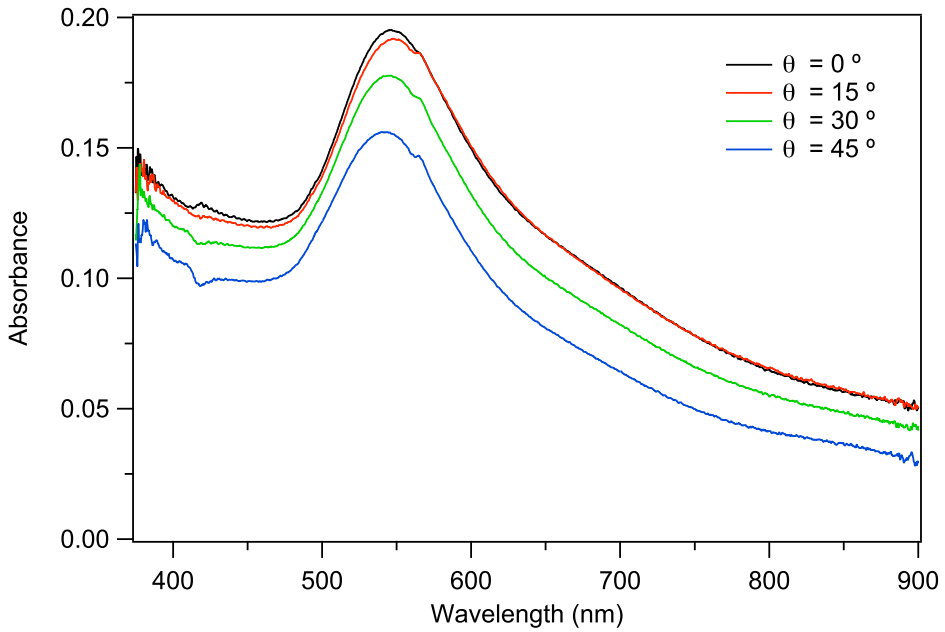

Figure 5.26: p-polarized absorbance spectra for PEGI66. Baseline measurements are taken with a clean BK7 reference slide. The polarizers show good transmission over the wavelength range 400nm to 1.2μm. The main peak visible is the $l = 1$, $m = 1$ mode. The $l = 1$, $m = 0$ mode would be visible around 300nm, but is not shown due to the limited spectral range.

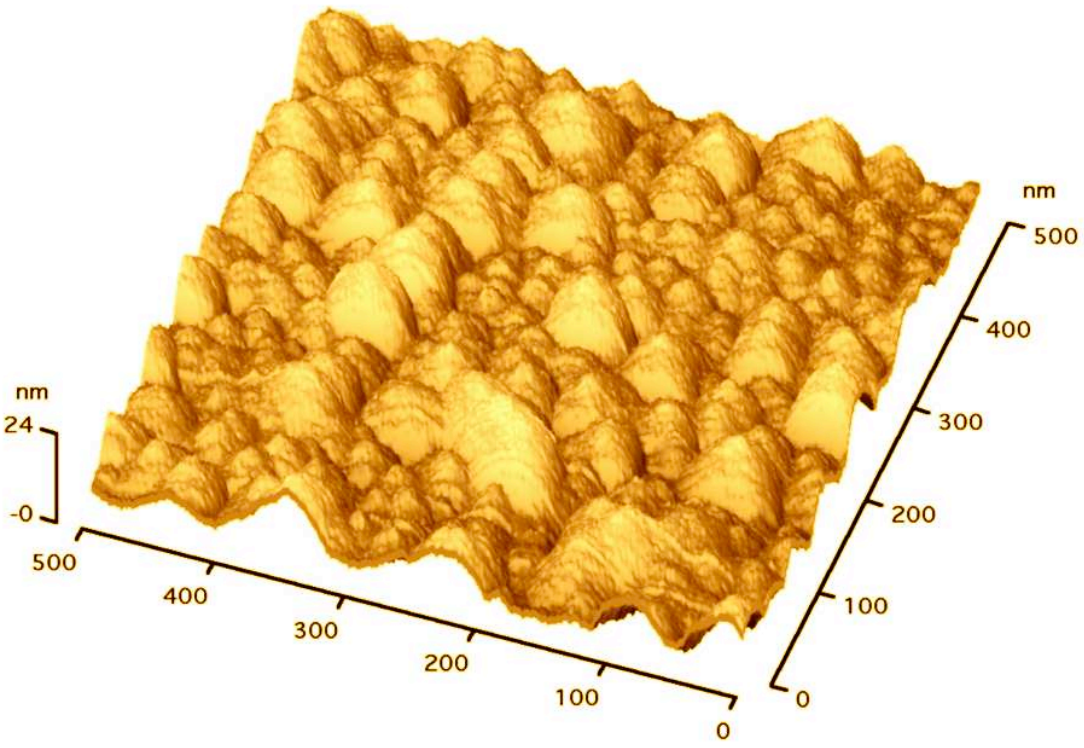

Figure 5.27: Typical AFM image of PEGI66 surface.

functions of substrate, overcoating and nanoparticle materials to be called from external libraries.

The substrate material, angle of incidence and polarization, and the nanoparticle dimensions are held constant for both models. However, two dielectric functions for Au; E. Palik's (ϵ^{Pal}) and the numerically generated dielectric function at $T = 295$K ($\epsilon^{num}(T = 295K)$) from Chapter 3, are used in order to make comparisons between the two.

Figure 5.28 shows the MTFA-generated absorbance spectra as N is varied. When the experimentally determined value is used, the model fails due to the product $N\sigma_{tot} > 1$, thus the number densities used are of the order of a magnitude less than that determined via microscopy. Figure 5.28(a) uses E. Palik's data for ϵ whereas Figure 5.28(b) uses $\epsilon^{num}(T = 295K)$. The maxima in the absorbance spectra occur consistently at the same wavelength for different N, but differ slightly depending on the dielectric function used. E. Palik's data results in absorbance peaks at 531.8nm, whereas $\epsilon^{num}(T = 295K)$ results in peaks at 538.0nm, a difference equal to 6.2nm. This difference is due to small discrepancies between the real parts of the two dielectric functions. The $\epsilon^{num}(T = 295K)$ generated absorbance spectra are also broader than the ϵ^{Pal} due to the small discrepancies between the imaginary parts of the two dielectric functions.

Figure 5.29 shows the absorbance at the corresponding peak wavelength as a function of N. ϵ^{Pal} provides consistently higher values of absorbance than $\epsilon^{num}(T = 295K)$ for the same values of N. Again, this is due to the small discrepancies between the two dielectric functions.

Figure 5.30 shows the experimental absorbance spectra together with the MTFA models for both dielectric functions. The values of N have been fit to match the peak experimental absorbance, resulting in $N = 3.34 \times 10^{13}$ m^{-2} for ϵ^{Pal} and 4.72×10^{13} m^{-2} for $\epsilon^{num}(T = 295K)$.

The same procedure was applied to the GranFilm models by changing the lattice constant (LC). Figure 5.31 shows the GranFilm-generated absorbance spectra as LC is varied. The effective lattice constant as determined from microscopy is 92.8nm, and unlike the MTFA model, GranFilm successfully generates data using this value. Figure 5.31(a) uses E. Palik's data for ϵ whereas Figure 5.31(b) uses $\epsilon^{num}(T = 295K)$. Unlike the MFTA model, the maxima in the GranFilm absorbance spectra occur at the same wavelength for relatively large (> 100nm) LC, but experience blue-shifting as the lattice constant approaches zero for both dielectric functions. This is due to GranFilm calculating the nanoparticle-nanoparticle interaction contribution, which increases as the nanoparticle spacing decreases. At LC = 50nm, the absorbance spectra resembles a thin-film than an isolated nanoparticle.

In the following analysis, attention is focused on values of LC > 100nm. Using ϵ^{num} results in an absorbance peak at 543.5nm, whereas using $\epsilon^{num}(\lambda, T = 295K)$ results in a peak at 558.2nm, a difference of 14.7nm. Again, this difference is due to small discrepancies between the real parts of the two dielectric functions. A larger difference is evident in the GranFilm models compared to the MFTA models. This is due to the approach used by each model to calculate the optical response. The MFTA model calculates the absorbance via the total cross-section of the nanoparticle, whereas GranFilm calculates the absorbance by first calculating the Fresnel transmission and reflection coefficients and subtracting each from unity. The $\epsilon^{num}(T = 295K)$ generated absorbance spectra are also broader than the ϵ^{Pal} generated due to the small discrepancies between the imaginary parts of the two dielectric functions.

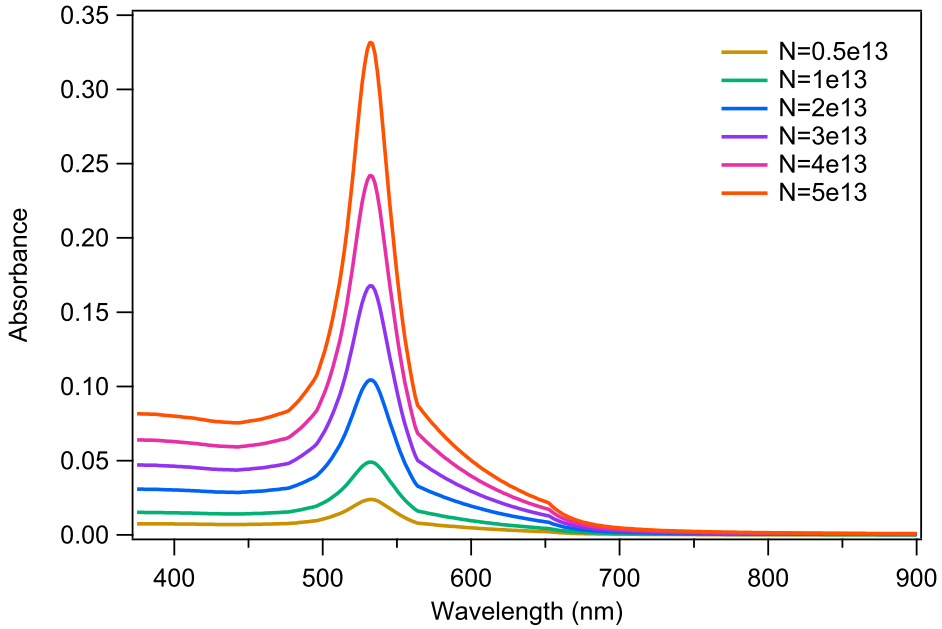

(a) Using ϵ^{Pal}

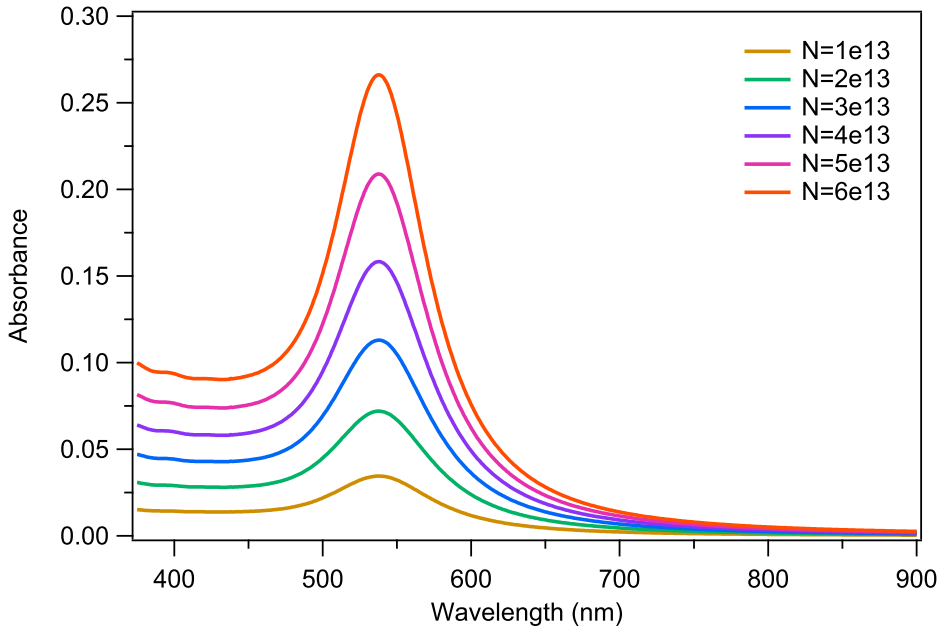

(b) Using $\epsilon^{num}(T = 295K)$

Figure 5.28: MTFA models with varying N for Au nanoparticles of dimension $r_0 = 35.2$nm, z_0= 9.4nm, supported on a BK7 substrate in air. The incident light is p-polarized at θ=0°.

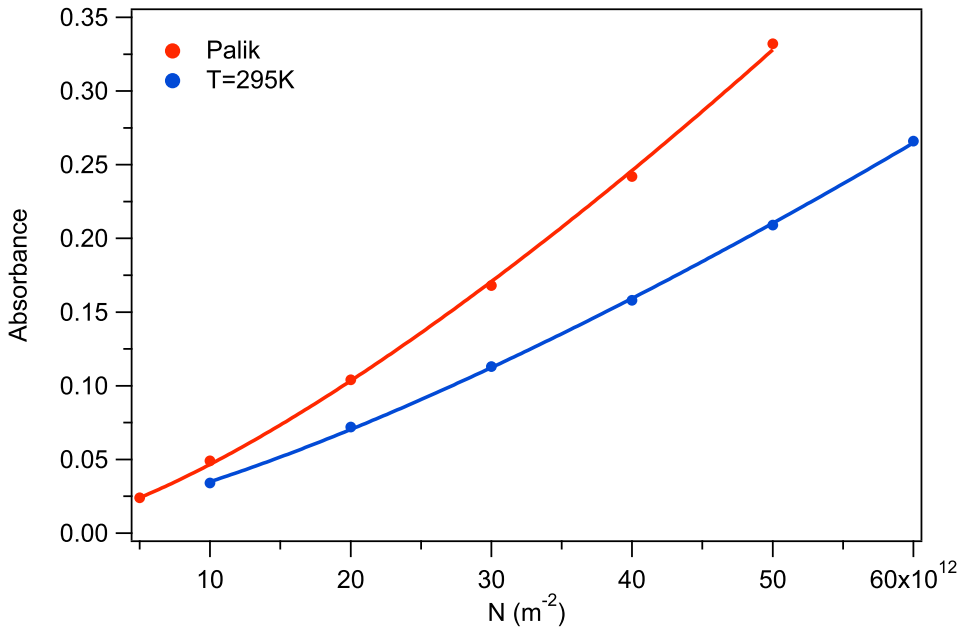

Figure 5.29: Peak absorbance values vs N (points) and an exponential fit (line), using both ϵ^{Pal} and $\epsilon^{num}(T = 295K)$ respectively, for the dielectric function of Au. The peak absorbance values occur at the same wavelength for each model, 531.8nm (Palik) and 538.0nm ($T = 295$K), for all data above.

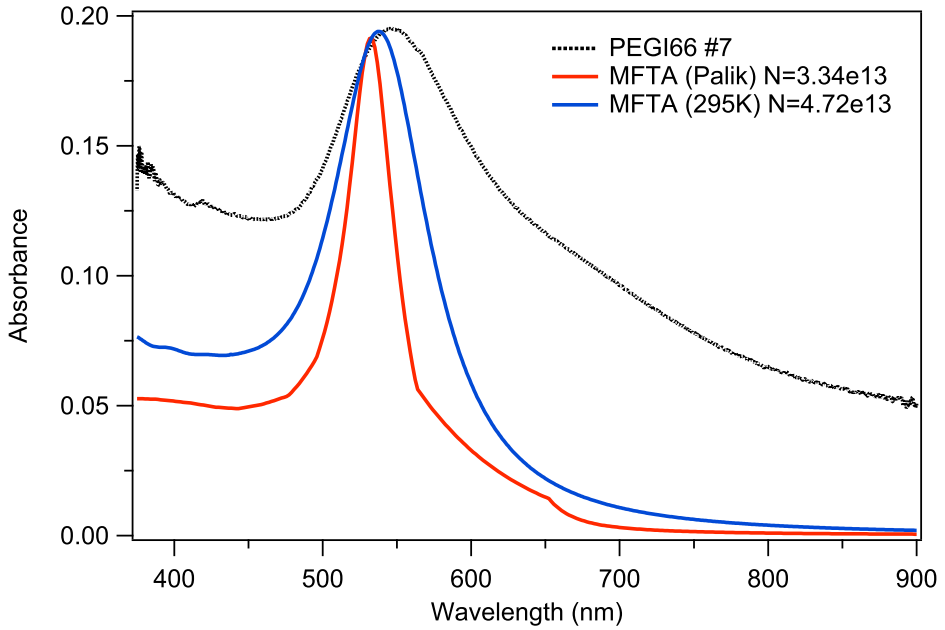

Figure 5.30: Absorbance spectra for PEGI66 and MFTA model with $N = \times 10^{13}$ m^{-2} (Palik) and $N = 4.72 \times 10^{13}$ m^{-2} ($T = 295$K). Peaks at 546.6nm (PEGI66), 531.8nm (MTFA-Palik), 538.0nm (MTFA-295K).

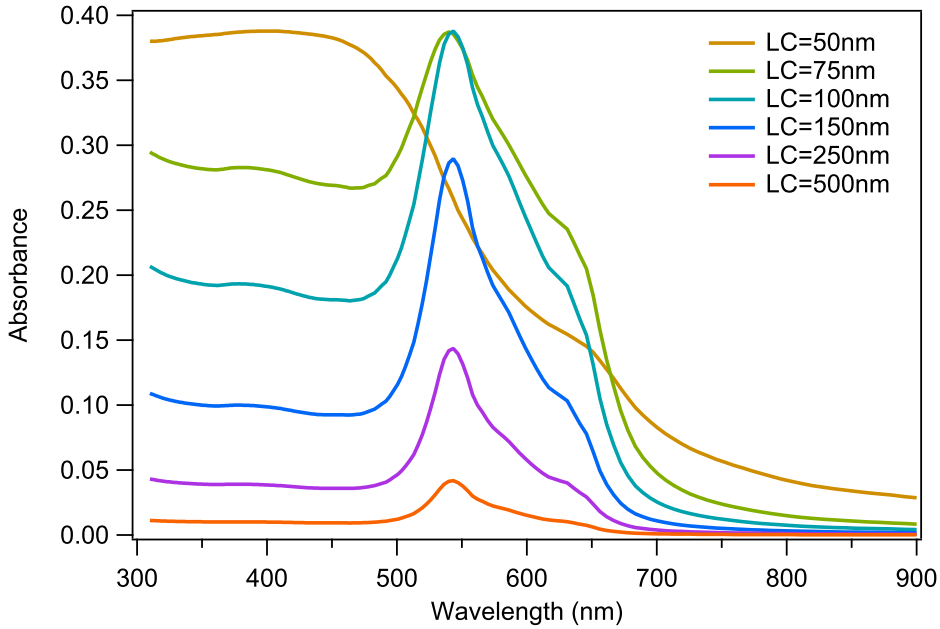

(a) Using ϵ^{Pal}

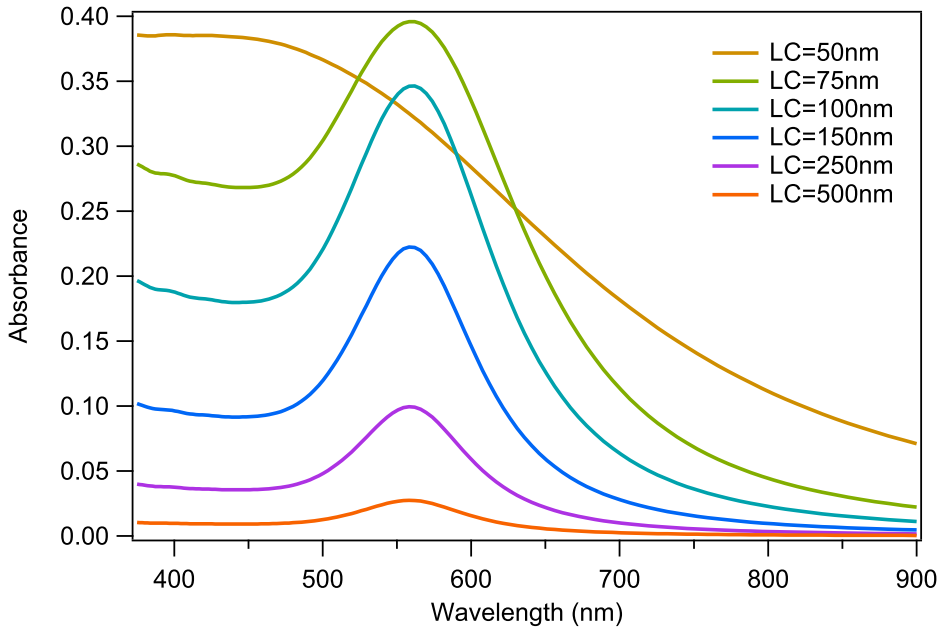

(b) Using $\epsilon^{num}(T = 295K)$

Figure 5.31: GranFilm models with varying lattice constant (LC) for Au nanoparticles of dimension $r_0 = 35.2$nm, $z_0 = 9.4$nm, supported on a BK7 substrate in air. The incident light is p-polarized at an angle of incidence $\theta = 0°$.

Figure 5.32 shows the absorbance at the corresponding peak wavelength as a function of LC. $\epsilon^{Pal}(\lambda)$ provides consistently higher values of absorbance than $\epsilon^{num}(\lambda, T = 295K)$ for the same values of LC. Again, this is due to the small discrepancies between the two dielectric functions.

Figure 5.33 shows the experimental absorbance spectra together with the GranFilm models for both dielectric functions. The values of LC have been fit to match the peak experimental absorbance, resulting in LC = 205.5nm for ϵ^{Pal} and 165.3nm for $\epsilon^{num}(T = 295K)$.

5.3.3 Conclusions

Metal-island films are considerably simpler to fabricate than GLAD and LIL template methods, however the optical properties aren't as controllable as demonstrated with the GLAD method, limiting absorption peaks and therefore range of pump lasers, to the visible. Depositing more material results in a larger absorbance due both to more particles and larger particles. Annealing shifts the absorption peaks toward the blue as the particles become more spherical and narrowing the broad absorption as the particles become more homogeneous.

The two models, MFTA and GranFilm, compare well with experiment. Each output similar absorbance curves, reproducing the main features of the experimental data with the position of the absorption peaks differing only by a few nanometers.

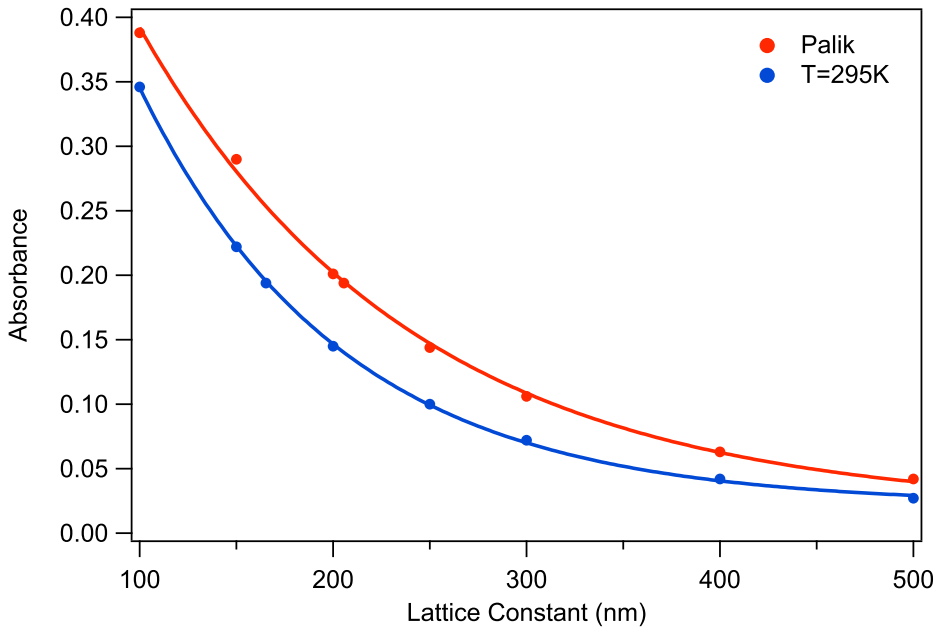

Figure 5.32: Peak absorbance values vs LC (points) and an exponential fit (line) using both ϵ^{Pal} and $\epsilon^{num}(T = 295K)$ respectively for the dielectric function of Au. The peak absorbance values occur at the same wavelength for each model for LC $>$ 100nm, 543.5nm (Palik) and 558.2nm ($T = 295$K), for all data above.

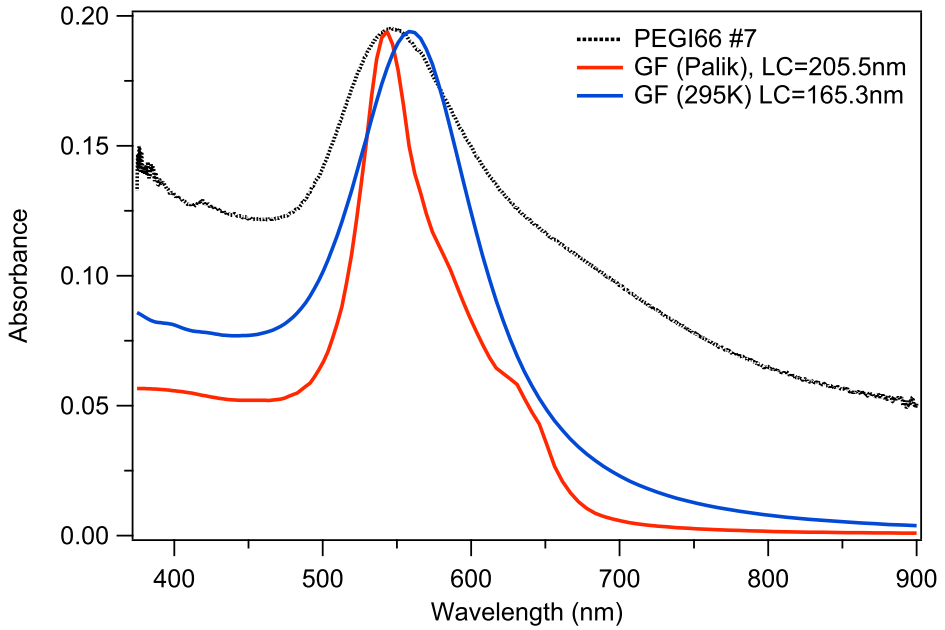

Figure 5.33: Abs spectra for PEGI66 with GF model with LC=205.5nm (Palik) and LC=163.5nm (295K). Peaks at 546.6nm (PEGI66), 543.4nm (GF-Palik), 558.2nm (GF-295K).

Chapter 6

Pump-Probe Experiments on Metal Island Films

6.1 Experimental Method

The goal of the pump-probe experiments is to measure the differential reflectivity, $\Delta R/R$, of the metal island film sample using a pump-probe technique. The pump beam, with a lasing wavelength close to the main absorption peak of the sample, provides the heating mechanism for the nanoparticles while the probe beam, with a lasing wavelength in the visible but sufficiently far enough from the main absorption peak in a spectral sense, is used to measure changes in the reflectivity of the sample. The pump beam is the 514.5nm line supplied by a Coherent Innova 70 series argon-ion laser. The Ar^+ laser is a continuous wave (CW) laser with a TEM_{10} polarized output and has a maximum light output of 100mW. The probe beam is supplied by a Melles Griot unpolarized HeNe operating at 632.8nm of maximum power 3mW.

Figure 6.1 shows the optical setup. A portion of the pump beam is split off and sent to a silicon photodetector which is used to measure the output intensity and fluctuations. The pump beam is then passed through an acousto-optic modulator (AOM), a polarization rotator which ensures p-polarization with respect to the sample, through a series of focusing lenses and is normally incident on Au-side of sample with a spot size approximately 100μm in diameter as measured with a calibrated imaging camera. After transmission through the sample, the remaining pump beam is blocked and absorbed to prevent any reflections back to the sample or detectors.

The probe beam is p-polarized using a standard sheet polarizer and a portion of the beam is split off as a reference. The probe beam is incident on the sample at 45° from the Au side and positioned to overlay the pump beam spot. Upon reflection from the sample, the probe beam is passed through a narrowband 632.8nm pass filter, thus blocking any stray reflections and scattering from the 514.5nm pump beam, and incident on a silicon photodetector. The photodetector has a maximum rise time of 10ns and thus is well suited to measurements over the intended modulation frequency range of these experiments. During all data collection, laboratory lighting is turned off and stray glare from visual displays minimized. The reflectivity of the Au nanoparticle sample is hence measured as the pump power and modulation rate is varied.

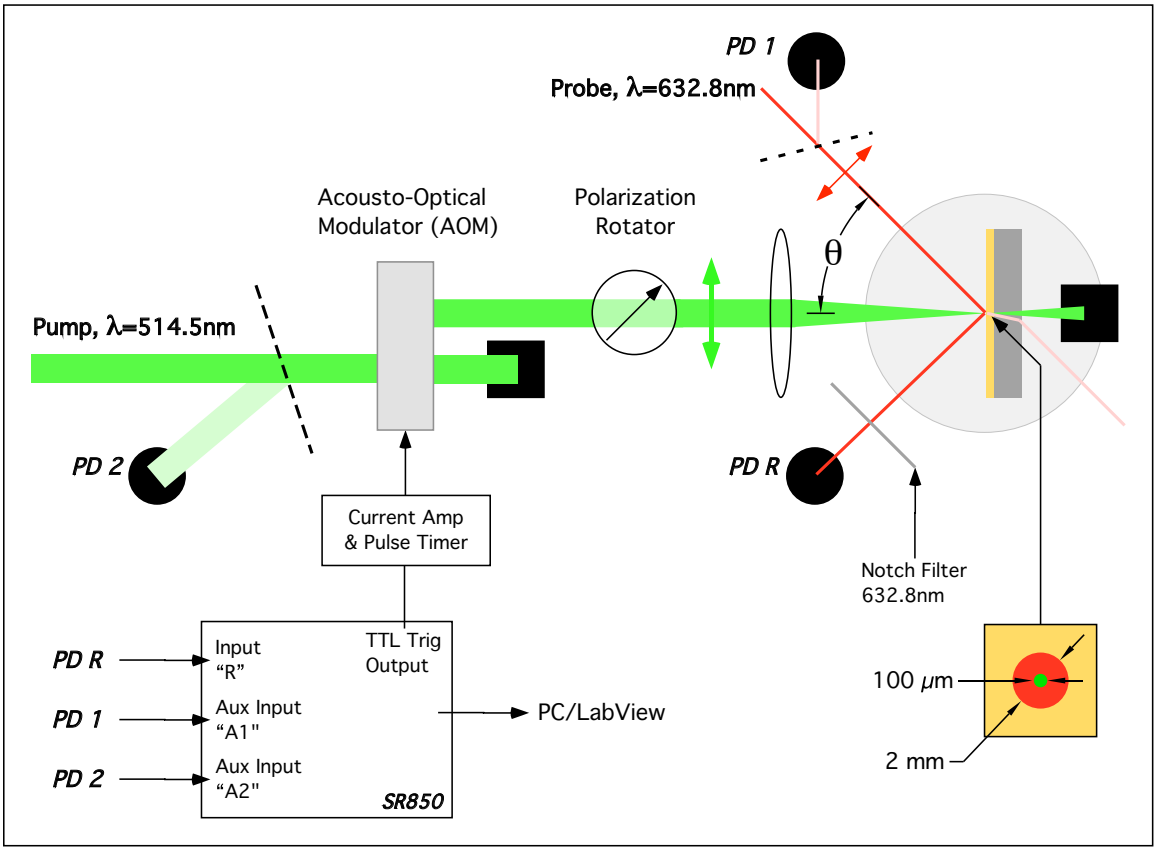

Figure 6.1: Pump-probe experiment optical set up.

The AOM can operate at modulation frequencies upto 10MHz, whereas a standard blade optical chopper can achieve modulation frequencies of maximum 1kHz. A SR850 lock-in amplifier is used to drive the AOM from a frequency stabilized TTL output via a high-speed current amplifier. This is advantageous as the modulation signal originates from the lock-in internal reference itself, thus minimizing any sources of electronic noise, drift and phase jitter from an external reference. Signals from the pump- and probe-beam reference photodetectors are input into the lock-in auxiliary input terminals for measurement. The signal from the probe photodetector is sent to the input terminal of the lock-in amplifier for synchronous detection measurement. A PC running NI Labview is interfaced to the lock-in via GBIP. A LabView program directly controls all aspects of the lock-in operation and AOM, and records all data to permanent storage for subsequent analysis.

As photodetectors don't output a signal proportional to incident power, calibration of photodetectors with a laser power meter is carried out for both pump and probe detectors. The laser power meter is positioned at sample, so the incident beam power reported this Chapter is the power incident on the sample after passing through all optics. Both pump and probe signals are normalized with respect to their references to minimize laser intensity fluctuations in reflectivity measurements. The probe differential reflectivity signal is recorded during an experimental run, then processed to find the mean value and standard deviation.

Prior to any data being taken, the pump laser output power is maximized by making small adjustments to the cavity mirrors. Any dust is blown off optical surfaces and the sample using a stream of dry filtered air. Alignment of the pump and probe beams on the sample is accomplished by setting the pump power to approximately half of full intensity at a modulation frequency of 1kHz. The probe beam, with a spot diameter of about 2mm, is roughly visually positioned to overlap pump beam spot on the sample. Refinements are made iteratively in the probe beam and detector positions to maximize the differential reflectivity signal, with care being taken to ensure a near-normal reflected probe beam incidence upon the photodiode active area.

Any possible signal originating from the substrate itself must be measured and taken into account. These measurements are taken using an identically cleaned BK7 substrate and later analyzed. The thermo-optic coefficients of optical glasses have been well studied. In particular, Ghosh [88] reports the thermooptic coefficient dn/dT for BK7 of 2.592×10^{-6}/K at $\lambda = 632.8$nm. However, the BK7 substrate heating alone is expected to be a negligible as BK7 is very weakly absorbing at the pump wavelength. Effects of indirect heating, i.e., the conduction of heat from a hot nanoparticle to the substrate thus heating the substrate and possibly providing a measurable signal, as considered later.

First, a baseline $\Delta R/R$ measurement is taken by shutting the pump beam aperture. All subsequent data is normalized with respect to this value as with no pump beam present $\Delta R/R$ is assumed to be zero. This takes into account any environmental thermal or mechanical perturbations on the sample. $\Delta R/R$ is then measured as pump power is increased for a specific modulation frequency. One data set is taken for each pump power setting, and is kept constant throughout run. When large fluctuations in the pump power are detected, the data set is repeated. After completing one pump-power run, the pump beam is then blocked, allowing the sample to cool for a few minutes. The modulation frequency changed and the experiment repeated. Baseline measurements are obtained prior to any pump power variation at each modulation frequency. The baseline measurement is subtracted from all

$\Delta R/R$ measurements to obtain results from only the influence of the pump beam on the Au nanoparticles. As pump power and modulation frequency are varied, lock-in settings such as gain, reserve and time constant are adjusted to obtain most stable phase. For modulation frequencies below 200Hz, the synchronous setting on the lock-in is used to further enhance accuracy at these low modulation frequencies.

6.2 Results & Discussion

Figures 6.2 and 6.3 show the $\Delta R/R$ signal for a clean BK7 glass substrate, i.e., with no Au. The substrate shows small but measurable signals over the frequency range 1Hz-100kHz. At low modulation frequencies ($\leq$ 200Hz), the signal is within the margin of error. Measurements at 1Hz are error-prone due to the lock-in time constants needed to make successful measurements at these frequencies. Measurements at all other frequencies, except 50kHz and 100kHz, have measurable responses with the margin of error spanning zero. The measurements for 50kHz and 100kHz are interesting, showing values of $\Delta R/R$ $\sim 1 \times 10^{-7}$ with small error bars together with a change in sign of the signal, but it is not quite understood where this signal arises from.

For the Au nanoparticle sample, using the incident pump power for the abscissa is acceptable, but it is more intuitive to transform the pump power into $\tilde{Q}_{NP}$ as given in equation (4.3.4), and reprinted below with the amendment that $R^0 \rightarrow R_p^0$ indicating p-polarization of the incident beams.

$$\tilde{Q}_{NP} = \frac{P_{abs,NP}}{\tilde{V}} \tag{6.2.1}$$

$$= \frac{P_0(1 - R_p^0 - 10^{-Abs})}{AN\tilde{V}} \tag{6.2.2}$$

R_p^0 is the reflectivity of the sample at normal incidence for p-polarization and is found to be 0.043. A is the spot size of the pump beam measured to be 7.9×10^{-9} m^2 and N is the number density of nanoparticles on the substrate surface measured experimentally to be 1.16×10^{14} m^{-2}. $Abs = 0.169$ at the pump wavelength of 514.5nm from Figure 5.24. $\tilde{V}$ is the average nanoparticle volume, equal to 4.88×10^{-23} m^3.

Figures 6.4 - 6.7 show the experimental data for $\Delta R/R$ as a function of $\tilde{Q}_{NP}$ as the modulation frequency is varied. In general, all $\Delta R/R$ curves, other than for modulation frequencies $\geq$ 20kHz, have a similar appearance. There is an initial linear response until around $\tilde{Q}_{NP} \sim 1.2 \times 10^{15}$ W/m^3 after which the $\Delta R/R$ slope seems to reverse. This slope reversal is believed to be due to heat retention and a $\Delta R/R$ signal from the substrate itself. For the 20kHz signal, the $\Delta R/R$ curve begins to flatten, and with higher modulation frequencies of 50kHz and 100kHz, the $\Delta R/R$ signal becomes negative. This is believed to originate from a hot-substrate signal.

FEMLab models, with the average nanoparticle size and spacing as determined in Chapter 5, are created with the same magnitude of heat source term $\tilde{Q}_{NP}$. Figure 6.8 shows the temperature of the nanoparticle after 1μs of heating, at which time the temperature has reached the steady-state value. The temperature exhibits a linear relationship with the heat source term, suggesting that the temperature of a single nanoparticle in the metal-island

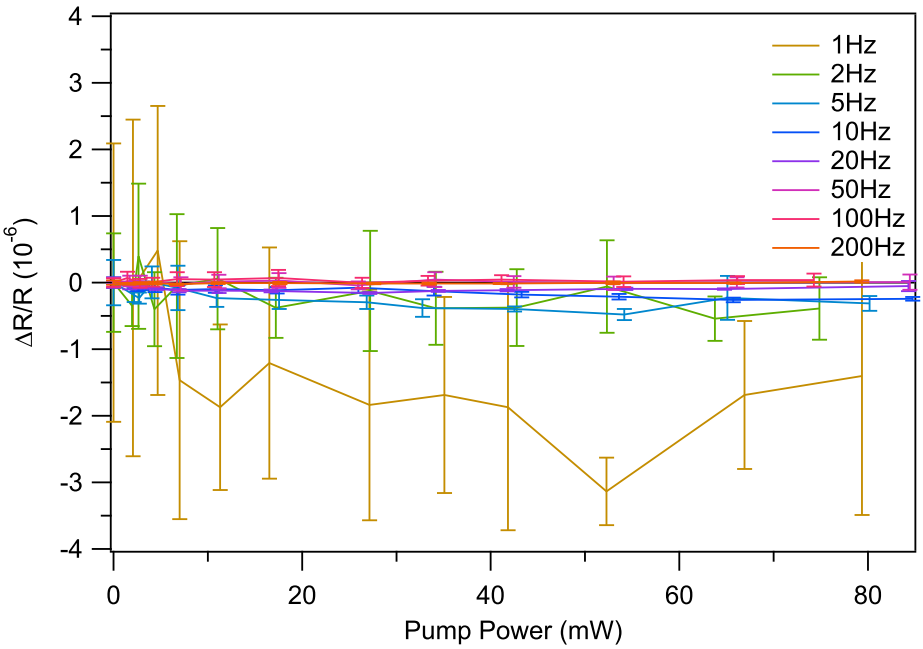

Figure 6.2: $\Delta R/R$ for modulation frequencies 1Hz to 200Hz on a clean BK7 substrate.

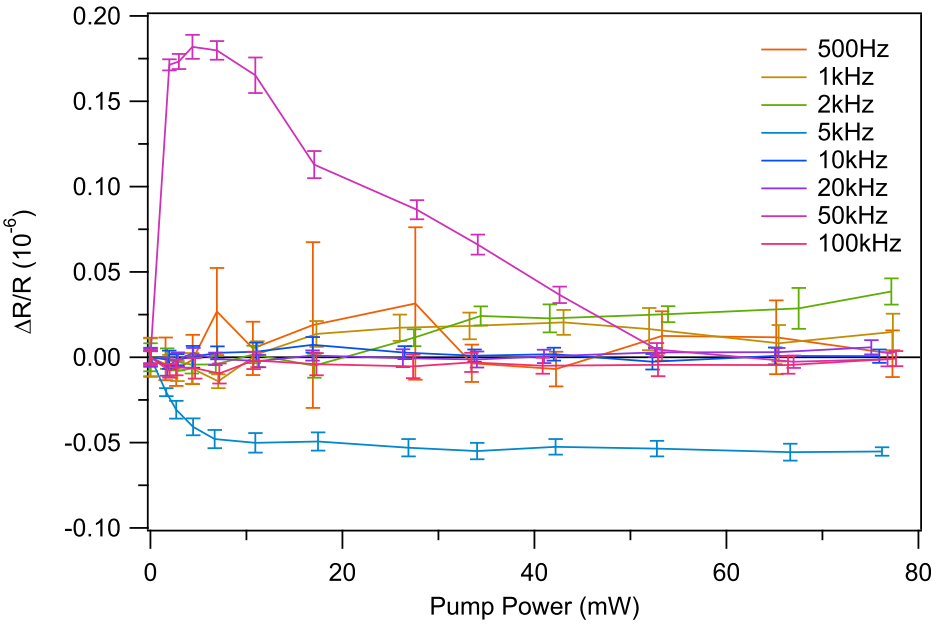

Figure 6.3: $\Delta R/R$ for modulation frequencies 500Hz to 100kHz on a clean BK7 substrate.

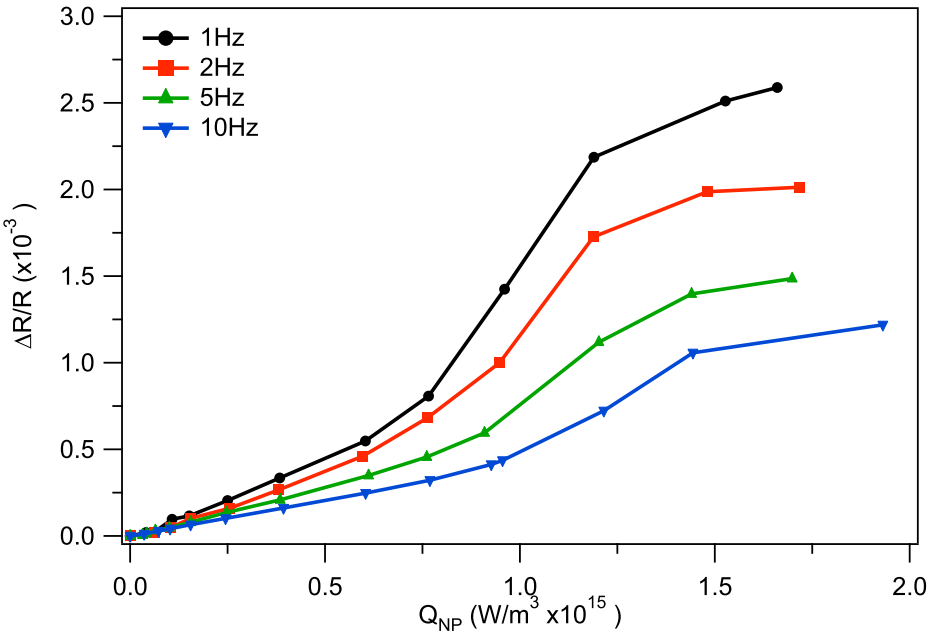

Figure 6.4: $\Delta R/R$ for modulation frequencies 1Hz to 10Hz on sample PEGI66: 3nm Au on BK7.

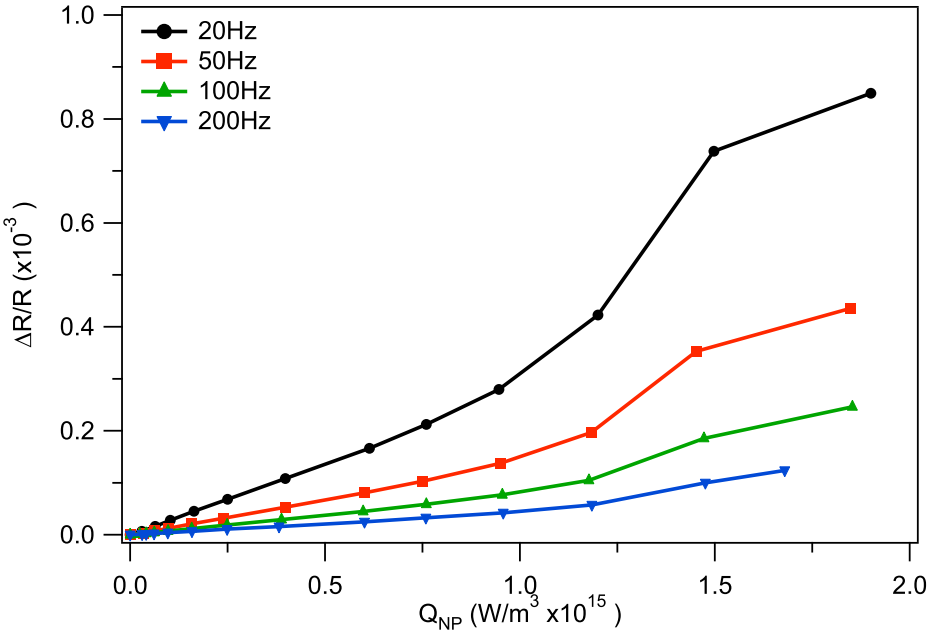

Figure 6.5: $\Delta R/R$ for modulation frequencies 20Hz to 200Hz on sample PEGI66: Au 3nm on BK7.

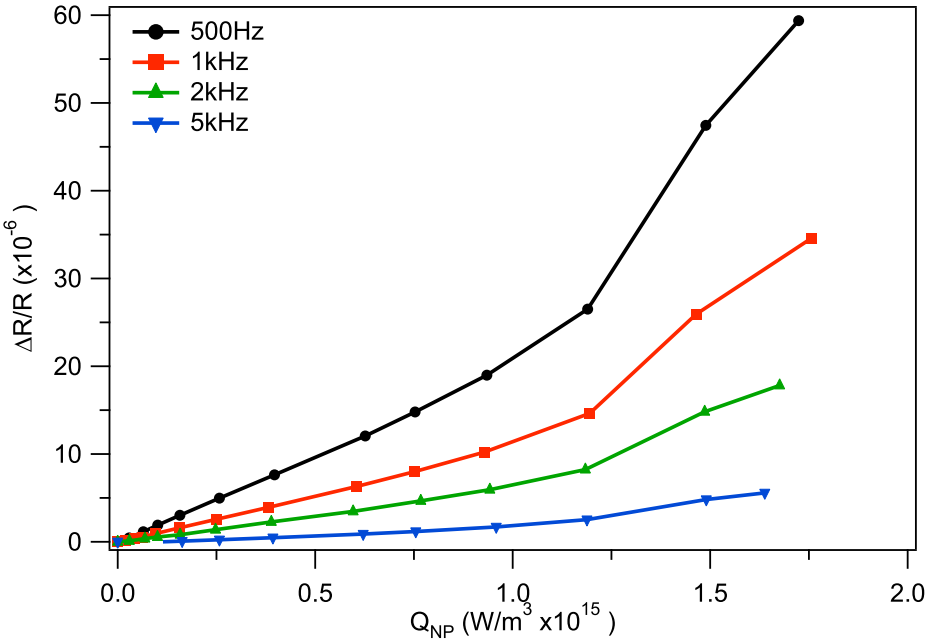

Figure 6.6: $\Delta R/R$ for modulation frequencies 500Hz to 5kHz on sample PEGI66: Au 3nm on BK7.

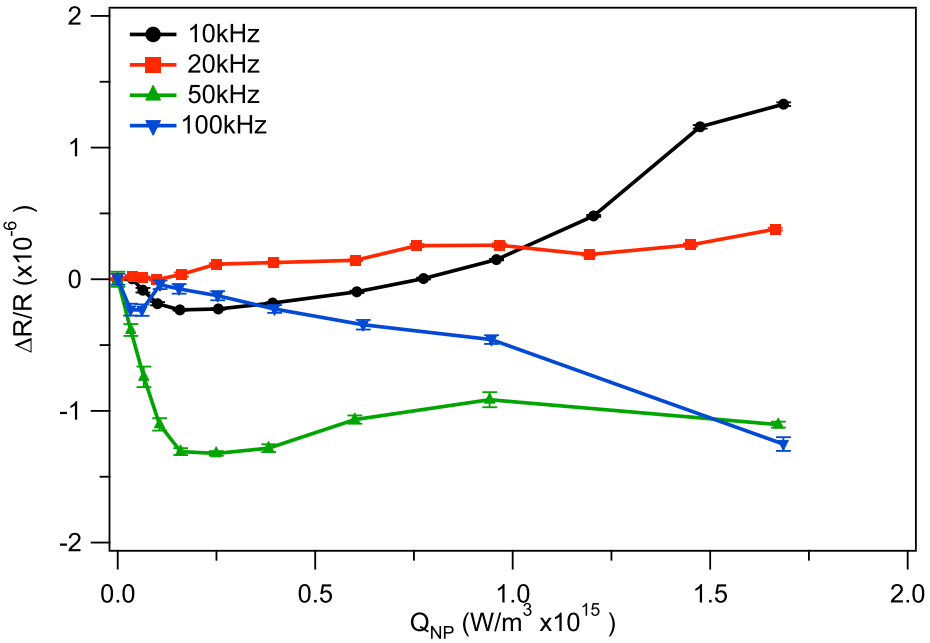

Figure 6.7: $\Delta R/R$ for modulation frequencies 1Hz to 10Hz on sample PEGI66: 3nm Au on BK7.

film is linearly proportional to $\tilde{Q}_{NP}$ and thus the incident pump beam power. FEMLab simulations show that the nanoparticle temperature only increases by a maximum of 2.7K with $\tilde{Q}_{NP} = 2.0 \times 10^{15}$ W/m^3.

Temperature dependent dielectric functions ϵ^{num} are generated using the method presented in Chapter 3 over the temperature range 295K-395K. These values of ϵ^{num} are used as inputs in GranFilm to produce models of $\Delta R/R$ for the nanoparticle sample, with particular emphasis on the temperature range 295K-297K, as shown in Figure 6.9. It should be noted that there is some uncertainty in the methodology employed by GranFilm to calculate the quantity ΔR, i.e., ΔR might be defined as $(R_0 - R_i)$ or $(R_i - R_0)$, the difference being a reversal in the sign. The experimental measurements of $\Delta R/R$ are simply the absolute magnitudes of the differential reflectance, i.e., $|\Delta R|/R$. Figure 6.9 is used to obtain values of $\Delta R/R$ specifically at the probe wavelength of 632.8nm, as shown in Figure 6.10. Again, one can see a linear trend in the now-absolute values of the differential reflectivity $|\Delta R|/R$ with respect to nanoparticle temperature.

The modeled $\Delta R/R$ vs. $\tilde{Q}_{NP}$ curve is shown, together with the experimental $\Delta R/R$ vs. $\tilde{Q}_{NP}$ for 1Hz, in Figure 6.11. These curves show relatively good agreement. However, FEMLab indicates the temperature reached in Figure 6.8 is constant after 1μs, corresponding to a modulation frequency of 500kHz. This is not the the case here as the experimental results show gradually decreasing values of $\Delta R/R$ as the modulation frequencies are increased. Clearly, there is some disagreement between the FEMLab-ϵ^{num}-GranFilm models used to produce Figure 6.10 and the experimental measurements. If $\Delta R/R$ is proportional to ΔT as is inferred, this suggests the steady-state temperature of the nanoparticle is less at higher modulation frequencies and that the heating of the nanoparticle is much slower than the FEMLab models predicts.

From Chapter 4, FEMLab shows that a nanoparticle reaches 90% of the steady-state temperature within the first 100ns of the heating phase. This is obviously not the case here. If the FEMLab models are accurate it implies a constant $\Delta R/R$ for modulation frequencies below approximately 5MHz. A gradual fall-off of the $\Delta R/R$ signal is expected to occur at modulation frequencies greater than 5MHz as heating times are reduced below 100ns. It is obvious that heat is conducted away from the nanoparticle to the substrate at a much greater rate than FEMLab predicts or the FEMLab model has ignored an important heat loss pathway. This would explain why lower modulation frequencies result in much larger $\Delta R/R$ signals than at higher frequencies.

The FEMLab models have assumed a perfect oblate spheroid in good thermal contact with it's surroundings. In reality, such a nanoparticle would likely be truncated by the substrate increasing the contact area. This would lead to more heat transfer from the nanoparticle to the substrate. Figure 6.12(a) shows the temperature evolution of perfect and truncated spheroids of equal volume heating with a heat source term of $\tilde{Q}_{NP} = 1 \times 10^{17}$ W/m^3.

The truncated spheroid heats marginally slower and does not reach the same steady-state temperature as the perfect spheroid. Similarly, Figure 6.12(b) shows the temperatures as a function of time for the same spheroids with the heat source term removed. Naturally the two spheroids reach the ambient temperature within 100ns of each other. Figure 6.13 shows the rate of change of temperature with respect to time for both perfect and truncated spheroids in the heating and cooling phases. The perfect spheroid heats and cools quicker than the truncated spheroid in the very first 20ns of each phase, with convergence after

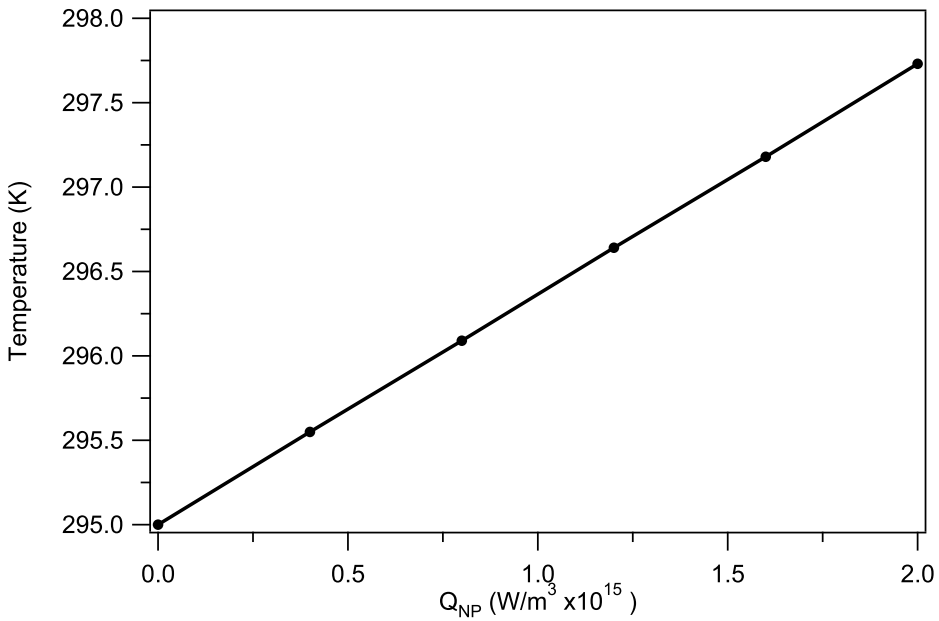

Figure 6.8: Steady-state temperatures, after heating for t=1μs, of the nanoparticle vs. the heat source term $\tilde{Q}_{NP}$ as modeled in FEMLab

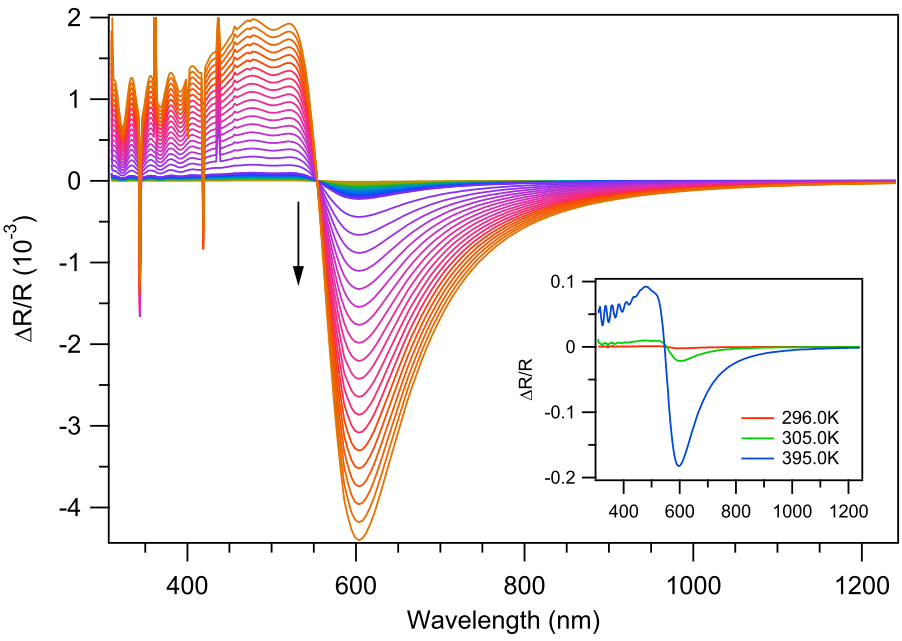

Figure 6.9: Granfilm generated $\Delta R/R$ curves using the temperature dependent dielectric functions ϵ^{num}. The temperature range is from 295.005K-297.0K (main window) and 296K-395K (inset). The arrow indicates the direction of increasing temperature.

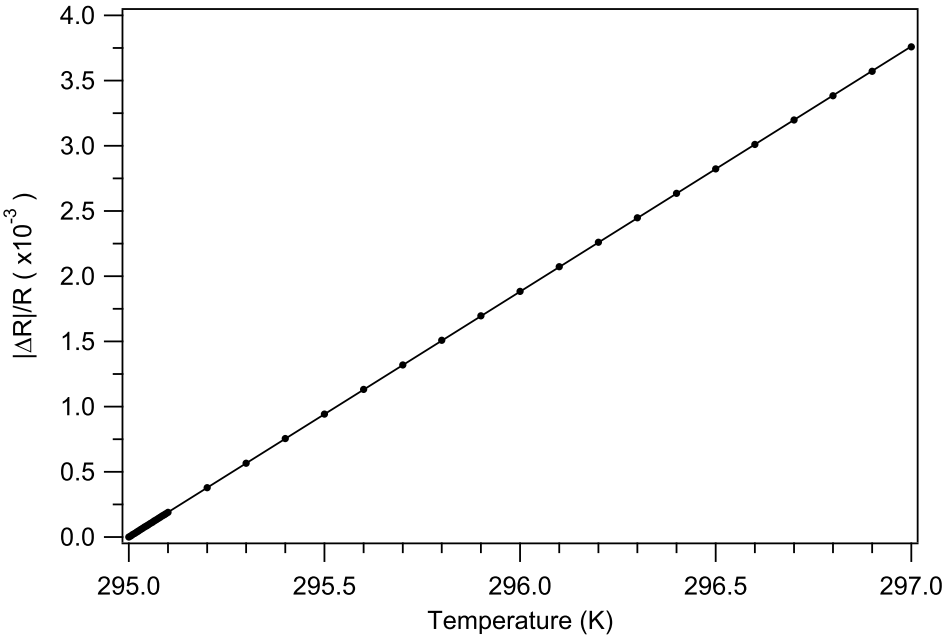

Figure 6.10: $\Delta R/R$ at 632.8nm vs. temperature obtained from Granfilm (points) and a linear fit (line).

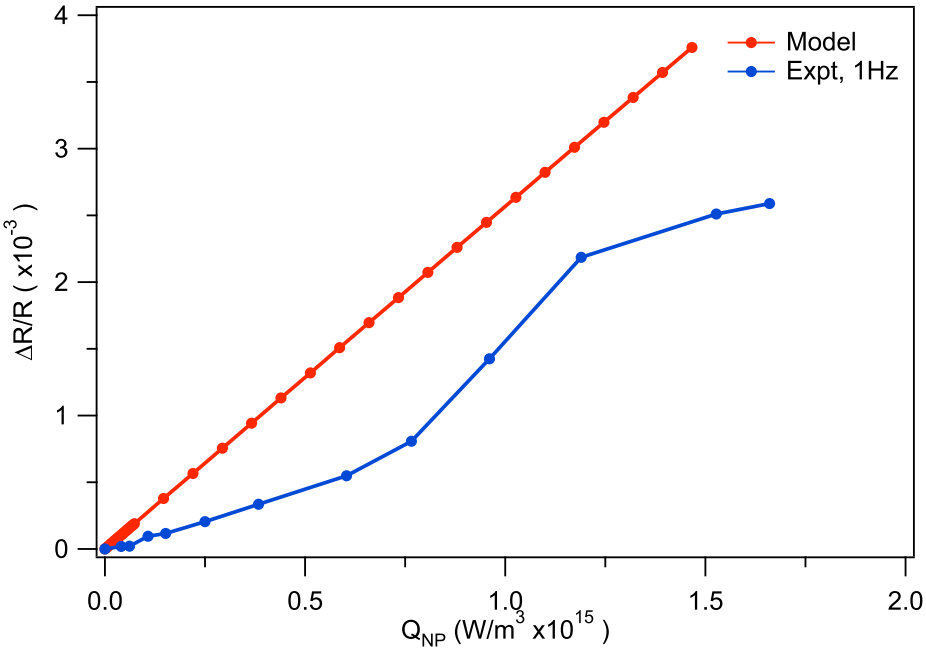

Figure 6.11: The modeled $\Delta R/R$ from the FEMLab, ϵ^{num} and Granfilm models compared with the experimental data obtained at a modulation rate of 1Hz.

$\sim$ 25ns and a steady state reached within 50ns. However, the difference in temperature evolution between a perfect and truncated spheroid is slight at best. This cannot be used to explain either the slow heating of the nanoparticles, or an increased heat-loss mechanism as the data suggests.

The area of the probe beam is much larger than the pump beam, in effect suggesting that a much larger number of nanoparticles are probed than heated with the pump. Indirect thermal coupling of nanoparticles inside the pump beam area to those outside would further contribute to nanoparticle heat loss rates, again affecting the heating rate. This may be remedied by two possible methods. Focussing the probe beam to a comparable area as the pump beam, or increasing the area of the pump beam to match the probe. However, these methods present new challenges. If the probe beam is focussed, this may lead to inadvertent heating of the nanoparticles by the probe beam itself unless it is very weak. This then presents issues with the accurate detection of small changes in an initially weak signal. If the pump beam is allowed to be larger, $\tilde{Q}_{NP}$ will be much smaller, leading to smaller temperature differences in the nanoparticle. A much more powerful laser may be used in this case to offset the reduced intensity at the substrate surface.

There are, of couse, errors in the determination of $\tilde{Q}_{NP}$. The largest source of error is the determination of N. If, somehow, a region of the sample was inadvertently chosen with a different nanoparticle N than determined by microscopy, this would result in much different values for $\tilde{Q}_{NP}$. However, this does not explain the gradual decrease of $\Delta R/R$ with increasing modulation frequency. This fall-off is almost certainly a heat conduction related effect, with heat being transferred away from the nanoparticle much quicker than the FEMLab models suggest.

There maybe a collective effect due to the large number of nanoparticles. It is known that radiative thermal conduction between nanoparticles can be quite large [75] and is proportional to r^6 and the nanoparticle spacing d^{-6}. With such a sample of small, isolated but close-packed nanoparticles, it may be necessary to include such nanoscale radiative effects in future simulations. In such a situation, the heat is transferred throughout this porous nanoscale structure having a certain effective mass. Reducing the effective mass of the sample by restricting the active area of the device with controllable sample preparation at a nanofabrication facility, together with near-field scanning microscopy (PSTM, NSOM) of the sample, will provide insight into this phenomena of nanoscale heat transport between close-packed nanoparticles. With greater understanding of the heat transfer processes, the performance of future plasmonic optical devices based on the thermooptical response of nanoparticles will be improved.

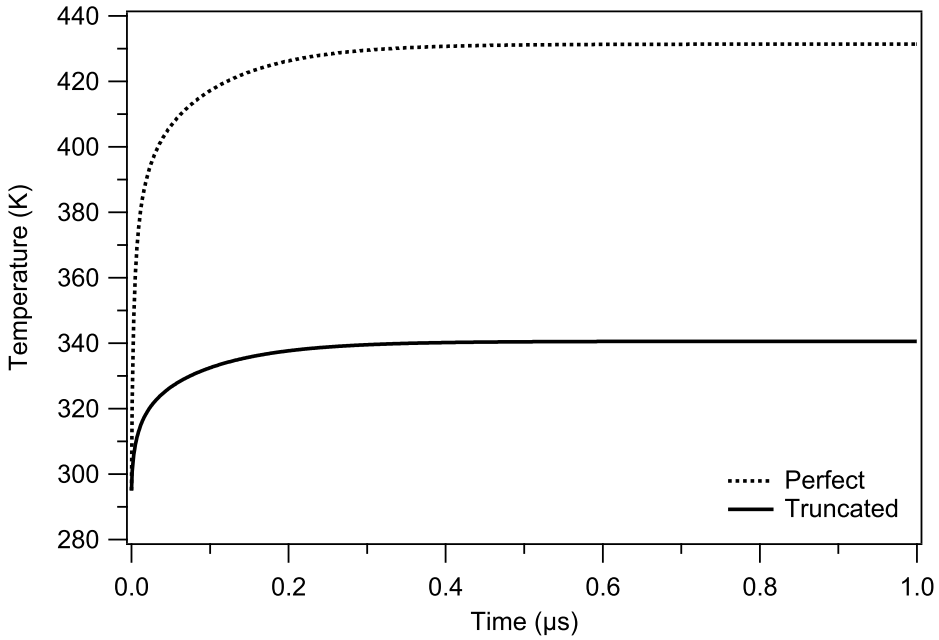

(a) Heating, $Q = 1 \times 10^{17}$ W/m^3

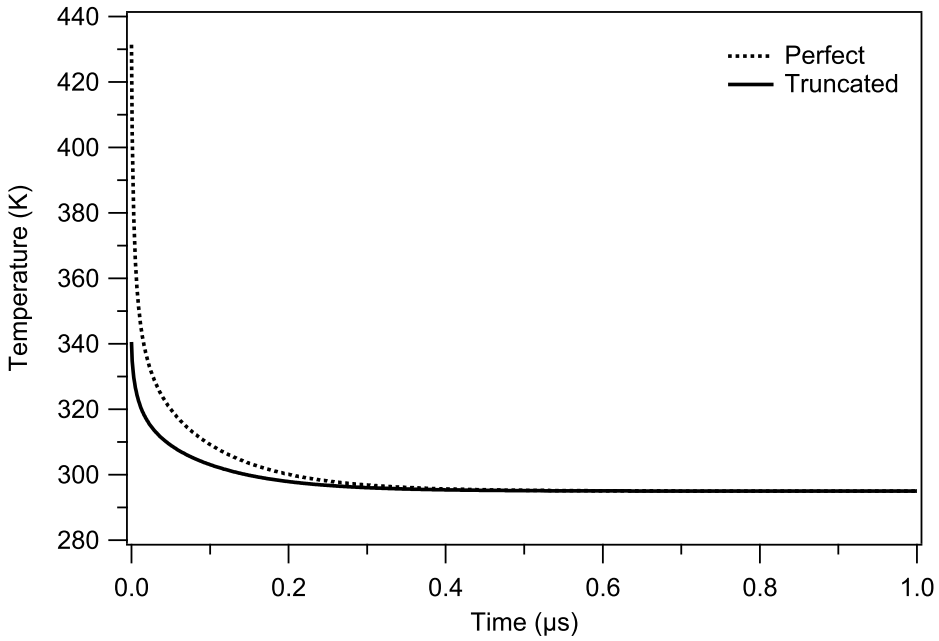

(b) Cooling, $Q = 0$ W/m^3

Figure 6.12: Temperature as a function of time for perfect and truncated oblate spheroids of equal volume during the heating and cooling phases.

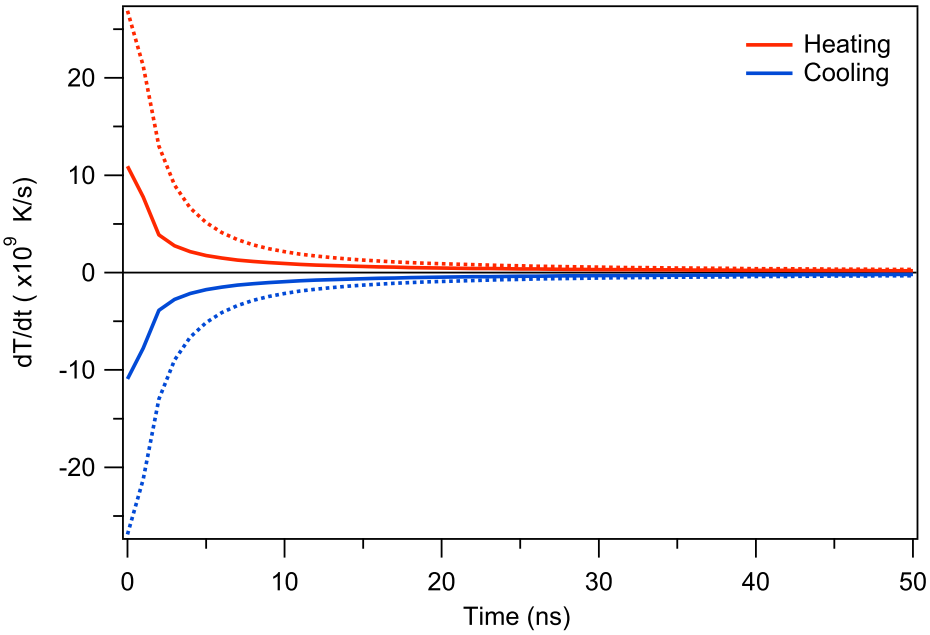

Figure 6.13: dT/dt for perfect and truncated oblate spheroids of equal volume during the heating and cooling phases. Solid lines represent the truncated spheroid and dashed lines represent the perfect spheroid.

Chapter 7

Conclusions

In summary, a metal island sample consisting of Au oblate spheroidal nanoparticles is used to investigate the feasibility of a plasmonic optical switch based on the laser heating of Au nanoparticles. The optical effects of increased temperature are studied, leading to a numerical method that generates realistic temperature dependent dielectric functions ϵ^{num} for Au. These results are input into the MFTA model and Granfilm software, providing the optical response and differential reflectivity spectra at arbitrary temperatures for Au metal island film samples. The thermal dynamics of laser heated Au nanoparticles on a insulating glass surface are studied using FEMLab in order to gain insight into the heating and cooling rates.

Several techniques were investigated in order to fabricate suitable samples of Au nanoparticles on glass substrates. Early promise in controlling the shape, therefore the optical response, of Au nanoparticles was shown using the GLAD method. However these samples were not suitable for pump-probe experiments due to the resulting large particle size and surface density. A metal-island film fabrication technique was found to be the most suitable in providing samples for the pump-probe differential reflectivity measurements.

The results are promising, showing that a signal applied to the pump beam can be transferred to the probe beam by heating, and thus changing, the optical properties of the Au nanoparticles. Detectable signals to a modulation frequency of 10kHz are obtained, an improvement over a similar device using a thin-film.

However, much more work needs to be done to further understand the physics involved of this intriguing problem. Improvements to the optical setup, including more sensitive detectors and more powerful tunable lasers are required. Improvements in the sample fabrication methods and careful selection of materials used would be advantageous in order to limit the active area of the device and the contact area of the nanoparticle-substrate interface. With advanced lithographic fabrication methods, nanoscale posts may be created to support these particles, further reducing the effect of the substrate in the heat losses from the nanoparticle. By growing the NPs to create specific shapes, perhaps using the GLAD method presented in Chapter 5, the absorption spectra can be shifted into a region where much more powerful lasers are available and where the thermooptic coefficients of the substrate are minimal. Theoretical, numerical and experimental efforts into the role of nanoscale thermal dynamics, particularly by radiative heat transport between nanoparticles, will result in greater understanding of the physics involved and greater performance of future plasmonic optical devices.

Bibliography

Bibliography

[1] A. L. Lereu, A. Passian, J. P. Goudonnet, T. Thundat, and T. L. Ferrell, Appl. Phys. Lett. **86**, 154101 (2005).

[2] D. Pines and D. Bohm, Phys. Rev. **85**, 338 (1952).

[3] R. W. Wood, Phys. Rev. **48**, 928 (1935).

[4] E. Rudberg, Phys. Rev. **50**, 138 (1936).

[5] R. H. Ritchie, Phys. Rev. **106**, 874 (1957).

[6] R. A. Ferrell and J. J. Quinn, Phys. Rev. **108**, 570 (1957).

[7] R. A. Ferrell, Phys. Rev. **111**, 1214 (1958).

[8] C. J. Powell and J. B. Swan, Phys. Rev. **115**, 869 (1959).

[9] C. Kunz and H. Raether, Solid State Comm. **1**, 214 (1963).

[10] A. Otto, Zeitschrift Fur Physik **216** (1968).

[11] E. Kretschmann and H. Raether, Zeitschrift Fur Naturforschung A **A 23** (1968).

[12] G. Mie, Ann. Physik **25**, 377 (1908).

[13] J. C. M. Garnett, Proc. Roy. Soc. London **73**, 443 (1904).

[14] W. T. Doyle, Phys. Rev. **111**, 1067 (1958).

[15] M. Bloemer, T. Ferrell, M. Buncick, and R. Warmack, Phys. Rev. B **37**, 8015 (1988).

[16] M. C. Buncick, R. J. Warmack, and T. L. Ferrell, J. Opt. Soc. Am. B. **4**, 927 (1987).

[17] A. Mary, A. Dereux, and T. L. Ferrell, Phys. Rev. B **72**, 155426 (2005).

[18] A. D. Boardman, *Electromagnetic Surface Modes*, Wiley, Chichester, 1982.

[19] W. R. Smythe, *Static and Dynamic Electricity*, McGraw-Hill, New York, 1968.

[20] J. A. Stratton, *Electromagnetic Theory*, McGraw-Hill, New York, 1941.

[21] F. Festy, A. Demming, and D. Richards, Ultramicroscopy **100**, 437 (2004).

[22] A. L. Demming, F. Festy, and D. Richards, J. Chem. Phys. **122**, 184716 (2005).

[23] R. Reddick, R. Warmack, and T. Ferrell, Phys. Rev. B **39**, 767 (1989).

[24] S. Nie and S. Emory, Science **275**, 1102 (1997).

[25] J. Goudonnet, J. Bijeon, R. Warmack, and T. Ferrell, Phys. Rev. B **43**, 4605 (1991).

[26] C. L. Haynes, A. D. McFarland, and R. P. V. Duyne, Anal. Chem. **77**, 338A (2005).

[27] J. Liu and Y. Lu, J. Am. Chem. Soc. **125**, 6642 (2003).

[28] J. Homola, S. S. Yee, and D. Myszka, *Optical Biosensors: Present and Future, edited by F. S. Ligler*, Elsevier Science, New York, 2002.

[29] H. Simon, D. Mitchell, and J. Watson, Phys. Rev. Lett. **33**, 1531 (1974).

[30] W. L. Barnes, A. Dereux, and T. W. Ebbesen, Nature **424**, 824 (2003).

[31] W. L. Barnes, W. A. Murray, J. Dintinger, E. Devaux, and T. W. Ebbesen, Phys. Rev. Lett. **92**, 107401 (2004).

[32] J.-C. Weeber et al., Phys. Rev. B **64**, 045411 (2001).

[33] L. Yin et al., Nano Lett. **5**, 1399 (2005).

[34] J. A. Dionne, L. A. Sweatlock, H. A. Atwater, and A. Polman, Phys. Rev. B **72**, 075405 (2005).

[35] S. A. Maier et al., Advanced Materials **15**, 562 (2003).

[36] N. Engheta, A. Salandrino, and A. Alu, Phys. Rev. Lett. **95**, 095504 (2005).

[37] D. Y. Tzou, *Macro- to microscale heat transfer : the lagging behavior*, Taylor & Francis, Washington, DC, 1997.

[38] M. Bonn et al., Phys. Rev. B **61**, 1101 (2000).

[39] J. K. Chen and J. E. Beraun, Numerical Heat Transfer A **40**, 1 (2001).

[40] M. Hu and G. V. Hartland, J. Phys. Chem. B **106**, 7029 (2002).

[41] M. Pelton, M. Liu, S. Park, N. F. Scherer, and P. Guyot-Sionnest, Phys. Rev. B **73**, 155419 (2006).

[42] H. Raether, *Surface plasmons on smooth and rough surfaces and on gratings*, volume 111, Springer-Verlag, Berlin, 1988.

[43] J. W. Little, T. L. Ferrell, T. A. Callcott, and E. T. Arakawa, Phys. Rev. B **26**, 5953 (1982).

[44] S. W. Kennerly, J. W. Little, R. J. Warmack, and T. L. Ferrell, Phys. Rev. B **29**, 2926 (1984).

[45] J. D. Jackson, *Classical Electrodynamics*, Wiley, New York, 3rd ed edition, 1999.

[46] M. Perner et al., Phys. Rev. Lett. **85**, 792 (2000).

[47] E. D. Palik and G. Ghosh, *Handbook of Optical Constants of Solids*, Academic Press, San Diego, 1998.

[48] M. Cardona, *Modulation Spectroscopy*, volume 11, Academic Press, New York, 1969.

[49] J. W. Scouler, Phys. Rev. Lett. **18**, 455 (1967).

[50] R. Rosei and D. W. Lynch, Phys. Rev. B **5**, 3883 (1972).

[51] B. R. Cooper and H. Ehrenreich, Phys. Rev. **138**, 494 (1965).

[52] N. E. Christensen and B. O. Seraphin, Phys. Rev. B **4**, 3321 (1971).

[53] M. Guerrisi and R. Rosei, Phys. Rev. B **12**, 557 (1975).

[54] P. Winsemius, M. Guerrisi, and R. Rosei, Phys. Rev. B **12**, 4570 (1975).

[55] S. Link, C. Burda, M. B. Mohamed, B. Nikoobakht, and M. A. El-Sayed, Phys. Rev. B **61**, 6086 (2000).

[56] C. Voisin, N. Del Fatti, D. Christofilos, and F. Vallee, J. Phys. Chem. B **105**, 2264 (2001).

[57] M. Rashidi-Huyeh and B. Palpant, Phys. Rev. B **74**, 075405 (2006).

[58] H. Petrova et al., Phys. Chem. Chem. Phys. **8**, 814 (2006).

[59] G. P. Pells and M. Shiga, J. Phys. C **2**, 1835 (1969).

[60] S. L. Logunov, T. S. Ahmadi, M. A. El-Sayed, J. T. Khoury, and R. L. Whetten, J. Phys. Chem. B **101**, 3713 (1997).

[61] H. Inouye, K. Tanaka, I. Tanahashi, and K. Hirao, Phys. Rev. B **57**, 11334 (1998).

[62] L. B. Scaffardi and J. O. Tocho, Nanotechnology **17**, 1309 (2006).

[63] C. Kittel, *Introduction to Solid State Physics*, Wiley, New York, 5th ed edition, 1976.

[64] M.-L. Thèye, Phys. Rev. B **2**, 3060 (1970).

[65] B. Dold and R. Mecke, Optik **22**, 435 (1965).

[66] D. E. Aspnes, E. Kinsbron, and D. D. Bacon, Phys. Rev. B **21**, 3290 (1980).

[67] J. R. Beattie and G. K. T. Conn, Philos. Mag. **46**, 222 (1955).

[68] M. Rashidi-Huyeh and B. Palpant, J. Appl. Phys. **96**, 4475 (2004).

[69] M. N. Ozisik, *Heat conduction*, Wiley, New York, 1980.

[70] Femlab.

[71] F. Cooper, Int. J. Heat Mass Transfer **00**, 991 (1977).

[72] G. Chen, D. Borca-Tasciuc, and R. G. Yang, Encyclopedia of Nanoscience and Nanotechnology **10**, 1 (2004).

[73] Umfpack.

[74] A. I. Volokitin and B. N. J. Persson, Phys. Rev. B **63** (2001).

[75] G. Domingues, S. Volz, K. Joulain, and J.-J. Greffet, Phys. Rev. Lett. **94** (2005).

[76] G. Mbise, G. B. Smith, and C. G. Granqvist, Thin Solid Films **174**, L123 (1989).

[77] K. Robbie, M. J. Brett, and A. Lakhtakia, J. Vac. Sci. Tech. A. **13**, 2991 (1995).

[78] K. Robbie and M. J. Brett, J. Vac. Sci. Tech. A **15**, 1460 (1997).

[79] B. Dick and M. J. Brett, J. Vac. Sci. Tech. B **21**, 23 (2003).

[80] P. C. P. Hrudey, K. L. Westra, and M. J. Brett, Adv. Mat. **18**, 224 (2006).

[81] D. R. Luhman and R. B. Hallock, Phys. Rev. E **70**, 051606 (2004).

[82] R. Lazzari and I. Simonsen, Thin Solid Films **419**, 124 (2002).

[83] *ImageJ* is a free image processing and analysis package written in Java. It can be downloaded from http://rsb.info.nih.gov/ij/.

[84] F. Yu et al., Biomaterials **26**, 2307 (2005).

[85] J. H. Moon et al., Synthetic Metals **148**, 99 (2005).

[86] U. Kreibig and M. Vollmer, *Optical Properties of Metal Clusters*, volume 25 of *Springer Series in Materials Science*, Springer, Berlin, 1995.

[87] D. Bedeaux and J. Vlieger, *Optical Properties of Surfaces*, Imperial College Press, London, 2002.

[88] G. Ghosh, *Handbook of Thermo-Optic Coefficients of Optical Materials with Applications*, Academic Press, San Diego, 1998.

Vita

Philip Gareth Evans was born in Manchester, England on 16th March 1979. He attended the British School in Riyadh, Saudi Arabia until age 14. He sat GCSE exams at Arnold School, Blackpool, 'A'-Level exams at Bolton School, Bolton and read Physics at the University of Bath, graduating with M.Phys. (Hons) in 2001. During his Masters' degree studies, he worked in the Liquid Crystal Devices research group at Sharp Laboratories of Europe Ltd., Oxford. He entered the Dept. of Physics & Astronomy at the University of Tennessee, Knoxville in 2002 to pursue the Doctorate of Philosophy in Physics under the supervision of Dr. Thomas L. Ferrell. The requirements for this degree were completed in April 2007. He is now known as Dr. Phil.